Montanuniversität Leoben

Fabrication and thermo-mechanical behavior of nanoporous copper

Diploma Thesis

by

Marius Kreuzeder

This work has been carried out at the Department of Materials Physics, University of Leoben in cooperation with the Department of Nuclear Engineering, University of California Berkeley.

Leoben, November 2013

Affidavit

I declare in lieu of oath, that I wrote this thesis and performed the associated research myself, using only literature cited in this volume.

Leoben, November 2013 Marius Kreuzeder

Acknowledgements

I take this opportunity to express my profound gratitude and deep regards to my guide Dr. Daniel Kiener for the possibility to write a diploma thesis at the Department for Material Physics in Leoben, and for his exemplary guidance, monitoring and constant encouragement throughout the course of this thesis. He always gave me excellent support and advice to all hours, and taught me how to work as a professional material scientist. I have gained much experience during the collaboration with Dr. Daniel Kiener.

I am highly thankful to Prof. Peter Hosemann for providing his Micromaterials nanoindenter at the Department for Nuclear Engineering at UC Berkeley, USA and his excellent scientific support. The stay in Berkeley was a fascinating experience in my life and gave me possibility to meet a lot of great people. At this point I want to say thanks to Dr. Manuel-David Abad and Dr. Marisa Rebelo de Figueiredo for the techniqual support and know-how at the nanoindenter.

I am obliged to Dr. Verena Maier for the valuable information provided by her in the fields of nanoindentation. I am grateful for her cooperation during the period of my thesis.

My sincere thanks also goes to DI Mario Stefenelli, who strongly supported me by conducting the X-ray diffraction measurements.

I would like to express my very great appreciation to those people who shared the great years of study, especially Mladen-Mateo Primorac.

Lastly, I thank almighty, my girlfriend, my parents, sisters and friends for their constant encouragement without which this thesis would not be possible.

Abbreviations and Symbols

ARB .....Accumulative Roll Bonding

At.% .....Atomic Percent

BCC .....Body Centered Cubic

BSE.....Back-Scattered-Electrons

cBN .....Cubic Boron Nitride

CG .....Coarse Grained

CL.....Constant Load

CRL.....Constant Rate of Loading

CSR.....Constant Strain Rate

CPS.....Counts Per Second

DC .....Depth Controlled

ECAP .....Equal Channel Angular Pressing

EDX .....Energy Dispersive X-ray Spectroscopy

FCC.....Face Centered Cubic

FE-SEM.....Field Emission Scanning Electron Microscope

FIB.....Focused Ion Beam

HPT .....High Pressure Torsion

LM.....Light Microscope

NC.....Nano Crystalline

NPC.....Nano Porous Copper

RT.....Room Temperature

SE.....Secondary Electrons

SEM.....Scanning Electron Microscope

SPD .....Severe Plastic Deformation

UFG.....Ultrafine grained

XRD .....X-Ray Diffraction

Abstract

Nanoporous materials are enormously interesting for future applications due to many excellent properties including: high surface-to-volume ratio, high strength-to-weight ratio, electrical and thermal conductivity, or radiation tolerance. These excellent properties can be used for combining structural purpose and a certain functional use in the same material at the same time. To use these foams more efficiently in the future, it is necessary to acquire information about the foam manufacturing, their thermo-mechanical properties, and the plastic deformation mechanisms.

Therefore, the objective of this diploma thesis was to manufacture nanoporous copper, to determine the thermo-mechanical properties, and to elucidate the deformation behavior at elevated temperatures. The experimental approach for manufacturing the foam structures used high-pressure torsion, subsequent heat treatments, and selective dissolution. Scanning electron microscopy was used for identifying the shape and size of the foam structures and their thermal stability. In-situ nanoindentation was conducted to determine mechanical properties and deformation mechanisms at elevated temperatures.

High-temperature nanoindentation was successfully conducted on nanoporous copper, showing a room temperature hardness of 220 MPa. During high temperature experiments, unexpected oxidation of the copper occurred even at low temperatures and the hardness rapidly increased to ~ 1 GPa. A model was developed, taking into account the mechanical properties of the copper oxides, which allows to explain the measured mechanical properties in dependence of the proceeding oxidation. The strain rate sensitivity of the copper foam strongly correlates with the strain rate sensitivity of ultrafine grained bulk copper. Although oxidation occurred near the surface, the rate-controlling process was still the deformation of the softer copper. An increase in the strain rate sensitivity with increasing temperature was observed, comparably to that of ultrafine grained copper, which can be linked to thermally activated processes at grain boundaries. Important insights into the effects of

oxidation on the deformation behavior were obtained by assessing the activation volume. Oxidation of the copper foam, thereby hindering dislocations to exit to the surface, resulted in a pronounced reduction of the apparent activation volume from $\sim 800 \cdot b^3$ to $\sim 50 \cdot b^3$, typical for ultrafine grained materials. These basic mechanistic insights shall contribute to a better understanding of the deformation processes of nanoporous materials at a microscopic level.

Table of contents

1 Introduction

Nanoporous materials have received considerable interest due to their many excellent properties including: electrical and thermal conductivity, or high surface-to-volume ratio. These kind of foams are widely used as catalysts, sensors, actuators and energy absorbing materials, and for many other applications. One potentially interesting application is to use foams as structural and functional material at the same time. Combining structural purpose and a certain function in the same material would be the desired solution for many applications. Decreasing the length-scale of ligaments down to nanometers leads to an enormous increase of the yield strength of the ligaments, approaching the theoretical strength of the material. Therefore, weight can be reduced due to the fact that nanoporous materials show mechanical properties close to their corresponding properties of the particular bulk material. Furthermore, special material properties, such as a high surface-to-volume ratio, can be utilized for special purposes. With such promising material properties, this kind of material has high potential for future applications.

One impressing fact about nanoporous materials is that the ligament size and morphology can be controlled by the manufacturing process, dedicated heat treatments, or chemical treatments. Adjusting these parameters in the desired way will allow tailoring of these foams for specific purposes. Therefore, the application of foams will continuously grow in the next years.

Even if the intended application is a functional purpose, it is required to acquire information about the mechanical properties of the material in order to understand the behavior of foams in many applications. Nanoindentation is a well-suited method to obtain many mechanical properties for micro- and nanoporous structures with high lateral- and depth resolution. Important data about the material can be obtained to determine the dominant deformation processes and mechanical behavior, even at elevated temperatures. Better knowledge about mechanical properties of nanoporous materials at elevated temperatures will improve our understanding of foams.

2 Theoretical Background

2.1 Severe plastic deformation

Severe plastic deformation (SPD) allows producing ultrafine-grained (UFG) and nanocrystalline (NC) metals and alloys with a high amount of high angle grain boundaries in a very effective way compared to other available techniques. SPD counts to the "Top Down" methods. The coarse grained starting material is highly deformed by large amounts of imposed strain during the "top down" production process to a fine-grained material. The three most common SPD methods are Accumulative Roll Bonding (ARB), Equal Channel Angular Pressing (ECAP) and High Pressure Torsion (HPT) as shown Figure 2.1. During the ARB process (Figure 2.1 (a)) a sheet is cut into two pieces and the surfaces are cleaned in order eliminate oxides and dirt. These two sheets are stacked together again, rolled to 50% thickness reduction and this process repeats several times to gain the desired grain refinement. The principle of ECAP is shown in Figure 2.1 (b). For this process a round or square shaped sample is pressed several times through a two channel consisting die. The angle ϕ of these two channels, as shown in Figure 2.1 (b), controls the amount of imposed shear. For the experiments conducted in this thesis, the HPT process was used for manufacturing the samples, which is yet another SPD technique that will be detailed in the following chapter. A more detailed description of the before mentioned SPD methods can be found in [1].

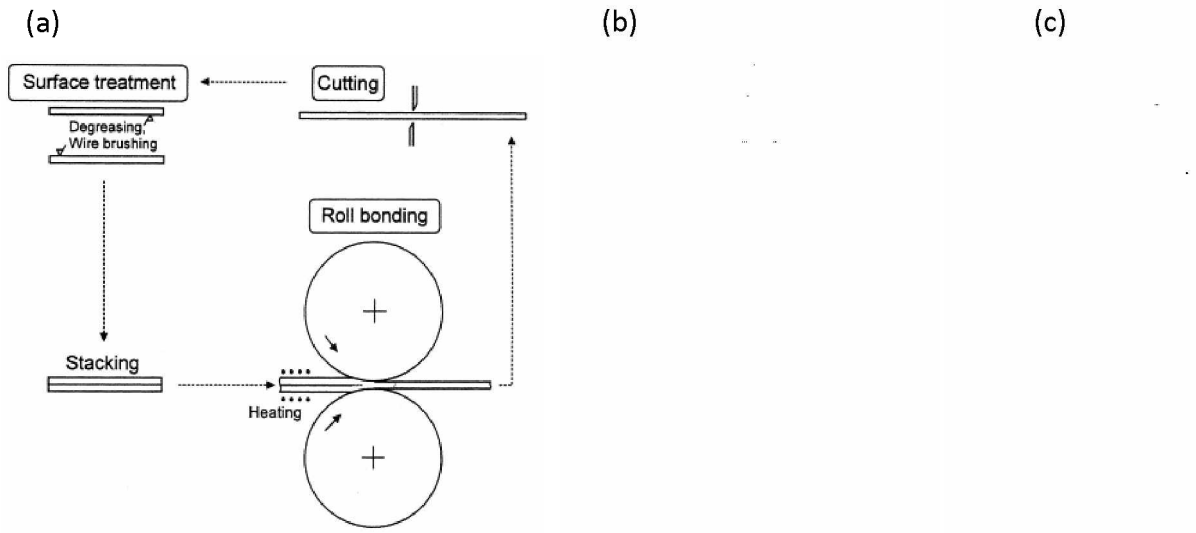

Figure 2.1: Schematic sketches of the most common SPD-methods: (a) ARB-Process (by Tsuji et al.[2]) (b) ECAP-Process (by Valiev et al.[3]) and (c) HPT-Process (by Valiev et al.[3]).

2.1.1 High pressure torsion

The most attractive grain refinement method among SPD techniques is HPT due to the very large imposed strains. The principle of this process is a simple torsion experiment as shown in Figure 2.1 (c). During this process a disk shaped specimen is set under hydrostatic pressure of several GPa between two anvils. The upper anvil is fixed, while the lower anvil is rotating and highly deforming the specimen in shear due to the friction between the specimen and the anvils. The high pressure during the process is the reason for avoiding crack initiation during the HPT-process and achieves largest strain values compared to all other SPD-methods possible. The shear strain γ imposed during the process at a distance R and a thickness t of the sample can be calculated with the following equation:

$$\gamma = \frac{2 \cdot \pi \cdot R \cdot N}{t}, \tag{1}$$

where N is the number of applied turns of the lower anvil.

At the Erich Schmid Institute two HPT-machines are installed. The first HPT machine has a maximum load of 400 kN, the second machine 4000 kN, respectively. With the large HPT-tool large samples with a diameter ranging from 30-50 mm and a thickness of 10 mm can be deformed. For comparison, the small HPT-tool is able to produce samples with a diameter of 6-14 mm and a thickness of maximum 1 mm. The small HPT tool additionally provides the possibility of cooling or heating the system during the deformation process from liquid nitrogen (-196°C) temperature up to 800°C.

During this diploma thesis a two-step HPT process was used as described by Bachmaier in [4] to create a nanocomposite from a mixture of two powders. After the first HPT step the final grain size d_1 of the individual phases in a composite can be described by the equation [4]:

$$d_1 = \frac{d_0}{\gamma_1}, \tag{2}$$

where d_o is the grain size of the initial component and γ_1 is the shear strain applied in this deformation process.

The experimental approach of this two-step HPT process is shown in the Figure 2.2. The deformed samples produced by the large HPT tool are then used for cutting smaller samples. These are used for the small HPT tool, but the shear direction now is rotated by 90°. After the second step, the grain size can be drastically reduced, which is described by following equation [4]:

$$d_2 = \frac{d_1}{\gamma_2} = \frac{d_0}{\gamma_1 \cdot \gamma_2}, \tag{3}$$

where d_2 is the individual composite structure size after both HPT steps and γ_1 and γ_2 are the applied shear strains of step 1 and step 2.

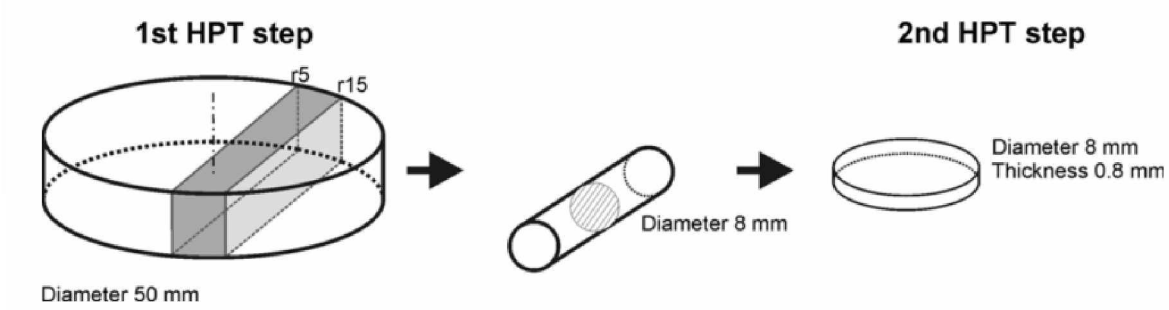

Figure 2.2: Schematic picture of the specimen processing: the grey zone of the compacted disk of the first HPT step was used for making a rod and cutting out smaller pieces for the second HPT step [4].

The main advantages related to this novel process are the capability to produce nanocomposites very fast and to achieve a homogeneous material microstructure. In addition, this is a more flexible way of handling the starting materials; the powders can be mixed to get materials with the desired composition [4]. Note that this kind of approach for nanocomposites is not possible by a melting metallurgy manufacturing route due to thermal activated processes leading to grain growth or immiscibility of certain elements as in the present work.

2.1.2 High pressure torsion of 2-phase metal-metal composites

The following chapter should give you an overview about metal-metal composites, with the focus on the Fe-Cu system. In general, there are three possibilities of what can be obtained during the HPT process of metal-metal composites [4]:

- A nanostructered composite due to grain refinement
- The formation of a supersaturated solid solution
- An amorphization reaction

The first step of an SPD process in a metal-metal-composite is grain refinement of both metals. If a critical thickness, which is dependent on the phase stability and phase mixtures of the constituents, is reached during the deformation process, unique futures such as supersaturated solid solution or amorphization reactions can occur. Especially for immiscible systems such as Fe-Cu (Figure 2.3), an enhancement of supersaturated solid solution can be observed [5–7]. The main mechanisms of this supersaturating process are diffusion, defect-enhanced diffusion, and mechanical intermixing driven by the plastic deformation [8]. Subsequent annealing can reverse the effect of supersaturated solid solution. Amorphization reactions are usually not observed in the case of Fe-Cu [9,10] and thus not discussed here. A detailed discussion of amorphization processes is given in [8].

Besides very high strength, this new class of metal-metal composites with immiscible elements exhibits great potential for superior magnetic, thermal, and electrical properties. However, for this work the main interest was the complete immiscibility of the two elements during the HPT process for the later foam processing.

The positive heat of mixing energy [11] and a different lattice structure of α-Fe (body-centered cubic (BCC)) and Cu (face-centered cubic (FCC)) ends up in an immiscibility even up to high temperatures of around 600°C as shown in the Fe-Cu phase diagram in Figure 2.3. In the Fe-Cu system the following phases can be found depending on the Cu and Fe ratio:

- Single phase FCC or BCC supersaturated solid solution for very low Cu or Fe contents or
- Two phase supersaturate solid solutions for intermediate compositions

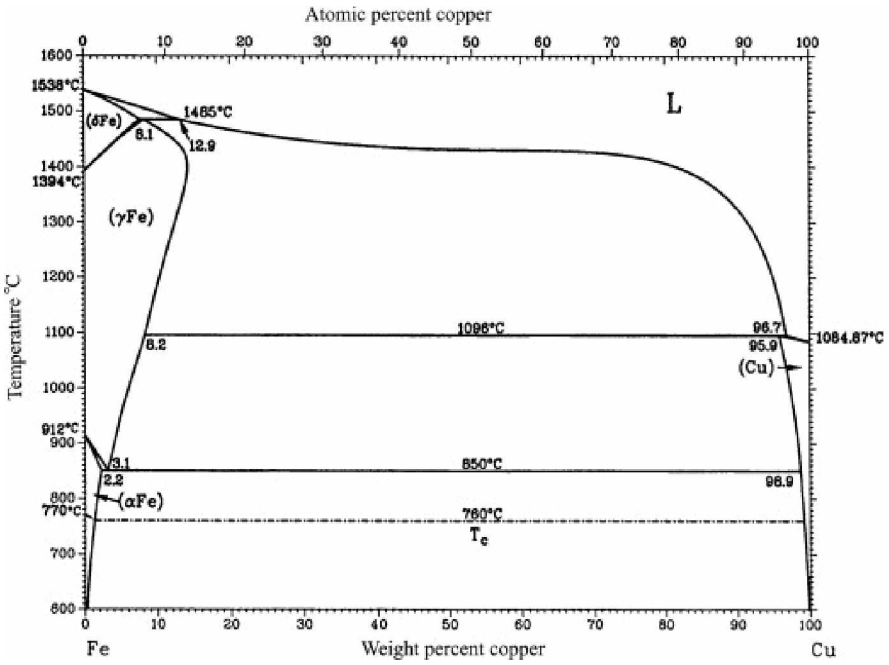

Figure 2.3: Fe-Cu phase diagram: shows the insolubility of Cu and Fe at low temperatures [12].

2.2 Foams

Nanoporous metals have attracted considerable interest in the past for various applications due to their excellent electrical and thermal conductivity properties, and a high surface-to-volume ratio. Foams are widely used as catalysts, sensors, actuators, lightweight structural materials, acoustic dampeners, energy absorbing materials, separation membranes and radiation tolerant materials [13–17]. In the near future, the importance of nanoporous structured materials will rapidly grow especially due to high demand of functional materials in the before mentioned applications. There are many methods to produce foams effectively, but recently the process of selective dissolution has been the focus of much attention for open cell nanoporous structures. Nanoporous metals, such as gold, palladium, silver, platinum, and copper have been successfully prepared by selective dissolution of a less noble alloying element in an aqueous solution [18].

2.2.1 Selective dissolution

In this work, the goal was to produce a nanoporous Cu (NPC). The requirements for a successful selective dissolution is to select a suitable copper alloy or composite as precursor and a desired open cell nanoporosity (porosity <60%). The precursor should have a large electrochemical potential between copper and the other alloying component. The standard reversible potentials of Cu/Cu^{2+} and Fe/Fe^{3+} are 0.342 V and -0.037 V (vs. standard hydrogen electrode) [19]. The electrochemical gap between the elements should normally be larger for ideal dealloying conditions, but the CuFe-system shows the best preconditions due to the immisci-

bility during the HPT-process. The process of selective dissolution is influenced by many parameters, such as the composition of the alloy, the concentration and the composition of the electrolyte, treatment time, and the temperature [20,21]. By controlling pore size, ligament size, and surface properties, a designing of foams for novel optical, sensing, and other special applications is possible [22,23].

The Pourbaix diagrams for Cu and Fe are shown in Figure 2.4. Every environment has a certain pH-range and an intrinsic oxidization power. This yields to specified areas in the Pourbaix diagram. HCl (Hydrocloric) acid is a reducing acid and the region of HCl is marked orange in the Pourbaix diagram of Fe and Cu (Figure 2.4). These diagrams are for a first estimation of what to expect during the selective dissolution process. Generally, this process is very sensitive to small changes of parameters and therefore it requires a great deal of experimentation to identify the perfect conditions for the dealloying experiments. For example, Figure 2.4 (a) shows that Fe should be immune in an environment of HCl, but a slow corrosion by dissolution exists at room temperature (RT). This indicates that the Pourbaix diagrams are just for a first approximation. The immunity of Cu can be seen in Figure 2.4 (b) and Figure 2.5 from room temperature up to 55°C.

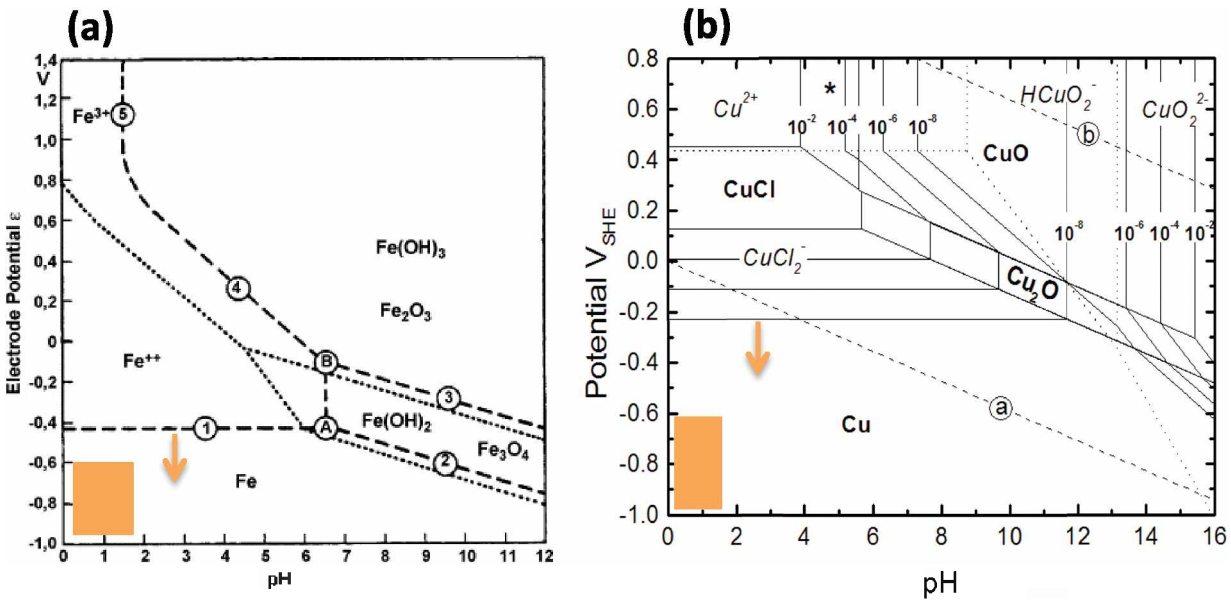

Figure 2.4: (a) Pourbaix diagram for Fe in aqueous solution (not available for Cl-aqueous solution). The arrow shows the change of the Fe^{2+}/Fe transition line to lower potentials at higher temperatures [24]. (b) The Pourbaix diagram for Cu in Cl-aqueous solution.

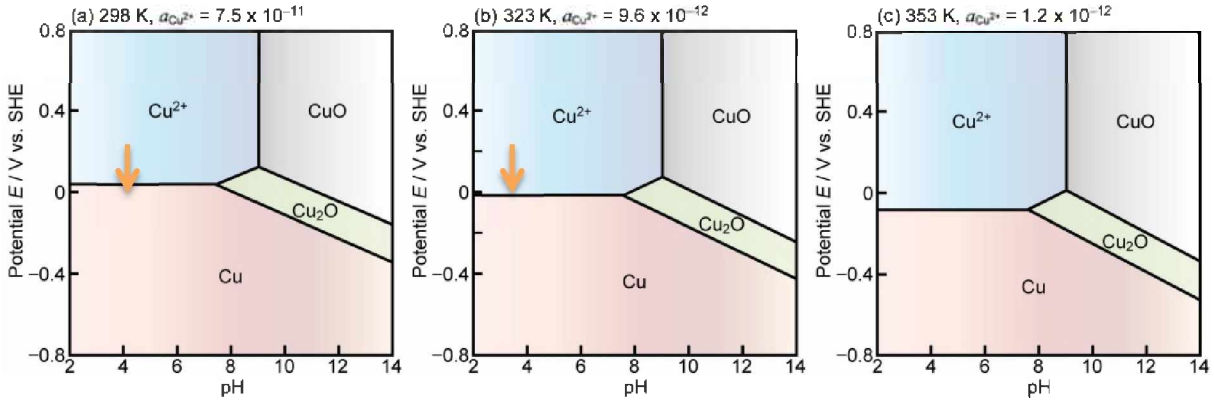

Figure 2.5: Change of the Pourbaix diagram for Cu at 298 K (a), 323 K (b) and 353 K (c) [25]. The arrows indicate the reduction of the potential.

2.2.2 Mechanical properties of foams

The efficient use of foams in many applications requires a detailed understanding of their mechanical behavior. Even when the main use is not related to a mechanical issue, such as thermal isolation, the strength and fracture toughness are still important to know. For basic understanding of the deformation of foams, it is essential to comprehend the deformation behavior during compression. In this diploma thesis, an elastic-plastic behavior is observed for the NPC. Therefore the following theoretical paragraphs deal with elastic-plastic metal foams, with a focus on the yield strength and the elastic modulus. Figure 2.6 shows a schematic compressive stress-strain curve and the different regimes for an elastic-plastic foam. The graph contains a linear elastic region for low stresses, followed by a long collapse plateau, and finally a regime of densification in which the stress subsequently rises steeply. Bending, simple extension or compression of the cell walls controls the linear-elastic regime. The Young's modulus is the initial slope of the stress-strain curve. The formation of plastic hinges occurs during the collapse plateau after the yield stress of the metal. When the cells are completely collapsed and opposing cell walls touch, densification occurs and the solid itself leads to the final rapidly increase of the flow stress. Higher relative densities raise the plateau stress, reduce the strain for the start of densification and increase the Young's modulus [26].

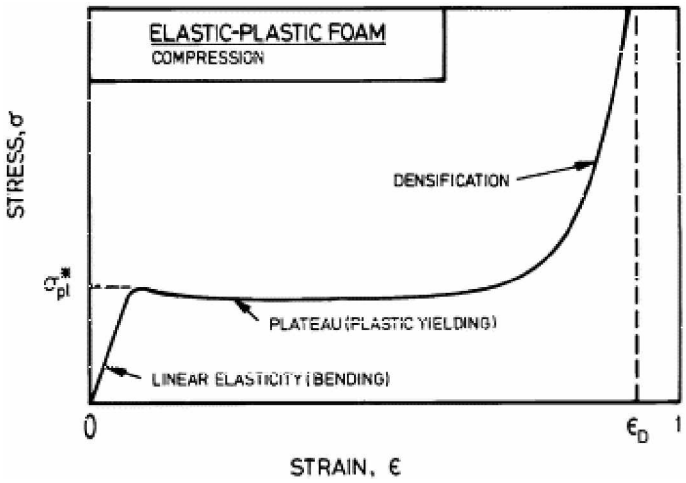

Figure 2.6: Elastic-plastic behavior of an open cell foam during compressing [26].

Gibson and Ashby have developed scaling equations for foams by using the relative density and the bulk material mechanical properties for a good estimation of the mechanical properties of foams. The yield strength σ_{pl}^* of open-cell foams related to the relative density (ρ^*/ρ_s) is given by equation [26]:

$$\sigma_{pl}^* = C_1 \cdot \sigma_{ys} \cdot (\rho^*/\rho_s)^n, \tag{4}$$

where σ_{ys}, ρ_s, and $\rho^*$are the yield strength of the solid, the density of the solid, and the density of the foam, respectively. C_1 is the proportionality constant describing the cell geometry, and *n* depends on the deformation mechanism of the cell. Experimental data shows that a wide range of open-cell foams can be described by $C_1 = 0.3$ and *n* = 1.5 [26].

The Young's modulus of an open-cell foam can be described by following equation [26]:

$$E^* = C_2 \cdot E_s \cdot (\rho^*/\rho_s)^n, \tag{5}$$

where E_s, ρ_s, and ρ^* are the Young's modulus, the density of the solid material, and the density of the foam, respectively. C_2 is the proportionality constant which describes the cell geometry, and *n* describes the elastic cell deformation via ligament bending. Open-cell foams are usually well fitted by using $C_2 = 1$ and *n* = 2 as given in [26].

These scaling equations are developed for macroporous foams and for lower densities than the foam used in this work. The effects of scaling from "macro to nano" has barely been a subject of discussion [27–29] and therefore very little is known and understood about the mechanical properties of nanoporous metals. Therefore, it is not clear if these models can be applied to porous materials on a length scale of only several hundred nanometers.

2.2.3 Plastic indentation

Foams drastically change their volume during compressing compared to dense solids, which are incompressible when plastically deformed. This can be explained by considering that during the deformation under the indenter the foam can change the volume and is not constrained by the surrounding material due to porosity. Thus the foam is compressed mostly uniaxial and the effective Poisson's ratio is near zero as shown in Figure 2.7. [30] A material with non-lateral expansion (effective Poisson's ratio near zero) during compression is then characterized by $H \sim \sigma_f$ instead of $H \sim 3 \cdot \sigma_f$ for a dense solid material, whereby σ_f is the flow stress of the investigated material. This near-zero Poisson ratio assumption is also used for obtaining the Young's modulus from of the reduced modulus [31], which is assessed from the load-displacement unloading curves.

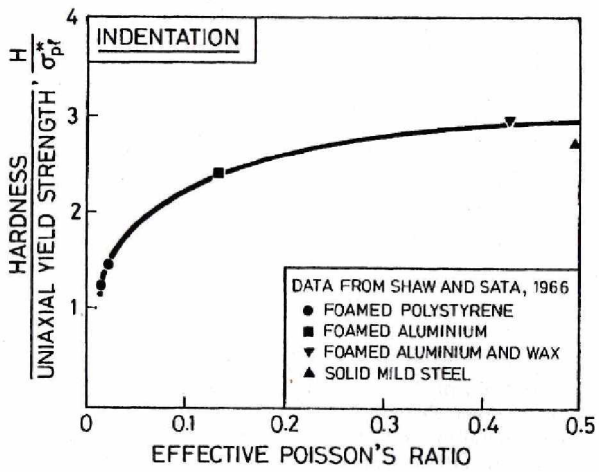

Figure 2.7: The ratio of indentation hardness to the uniaxial yield strength as a function of the effective Poisson's ratio during plastic yielding for different materials [26].

2.2.4 Effect of temperature and strain rate

The strength and stiffness of foams depend on temperature T and the strain rate $\dot{\varepsilon}$. The Young's modulus of a foam is proportional to the Young's modulus of the cell walls as given by equation (4). Increasing the strain rate does not affect the modulus but increases the strength of the material. A convenient estimation for metal and ceramic foams is given in the following equation [26]:

$$E_S = E_S^0 \cdot \left(1 - \alpha_m \cdot \frac{T}{T_m}\right), \tag{6}$$

where E_S^0 is the modulus at a temperature of 0°K and α_m is a material constant (typically $\alpha_m = 0.5 \pm 0.2$). This indicates a more or less linear variation of the Young's modulus with temperature.

The plastic collapse strength σ_{pl}^{*} of metal and ceramic foams can also be approximated by equation [26]:

$$\sigma_{pl}^{*} = \sigma_{pl}^{*\,0} \cdot \left(1 - \frac{AT}{T_m} \ln \frac{\dot{\varepsilon}_0}{\dot{\varepsilon}}\right), \tag{7}$$

here $\sigma_{pl}^{*\,0}$ is the yield strength at 0 K , *A* is a constant in the order 0.04 and $\dot{\varepsilon}_0$ is a kinetic constant of about 10^6 s^{-1}. This equation shows a linear decrease in yield strength with increasing temperature. An increasing strain rate just slightly influences the yield strength. The dependence of σ_{pl}^{*} on density (see equation (4)) is not influenced by changes in temperature or strain rate.

2.3 Nanoindentation

Nanoindentation has become an increasingly attractive technique for the assessment of mechanical properties in submicron-sized volumes of material due to the high depth and load resolution. This technique is especially useful in determining the change of the mechanical properties at elevated temperatures as well as time-dependent properties, such as: creep, relaxation, and strain rate sensitivity *m.* In this chapter, essential basics for the data evaluation, which has been performed during this diploma thesis, and the specific nanoindenter, are explained.

2.3.1 "Micromaterials" nanoindenter

All the indentation measurements presented in this work were performed with a nanoindenter (Micro Materials NanoTest Platform 3, Micromaterials, UK) with a high temperature option at the Department for Nuclear Engineering at the University of California in Berkeley, CA, USA, which is illustrated in Figure 2.8. The primary section of device consists of a movable pendulum, which is controlled by a magnetic field produced by a coil as shown in Figure 2.8 (b). The pendulum applies a certain load on the indenter tip controlled by the applied voltage. The whole instrument is directly mounted on a special floating table to reduce vibrations. The nanoindenter is placed in a chamber, which can be purged with gas in order to change the experimental environment for special purposes. High temperature measurements of up to 750°C can be performed thanks to a special heating and water cooling system, which is described later in chapter 3.6.1. An optical microscope with four magnifications allows an accurate placing of the indents on the specimen.

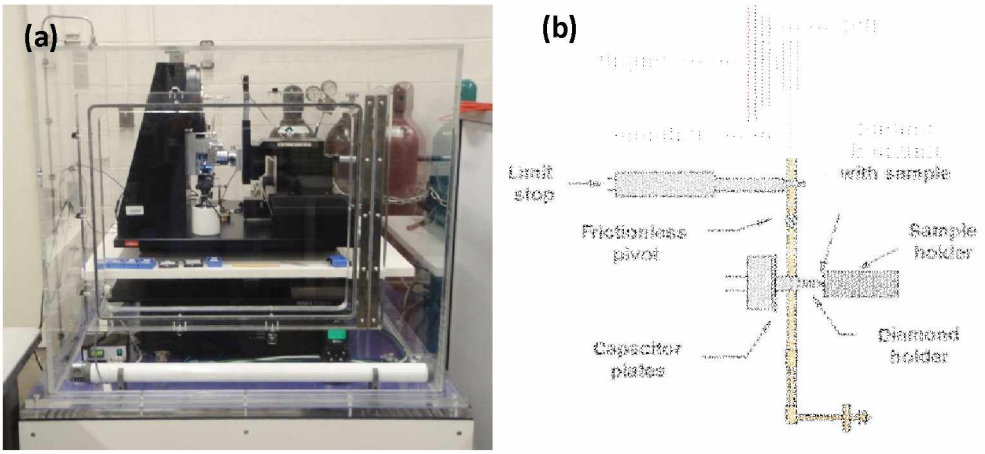

Figure 2.8: (a) Image of the used nanoindenter and (b) Schematic of the equipment configuration [32].

2.3.2 Evaluation of the hardness and Young's modulus

The evaluation of hardness and reduced modulus during this work is performed from the load-displacement curves by the Oliver-Pharr-method [33]. The calibration of the tip geometry is essential for this kind of evaluation. For the tip calibration, amorphous materials such as fused silica are appropriate due to their isotropic elastic-plastic behavior. Figure 2.9 (a) shows a typical load-displacement curve with essential parameters. During this indentation process a tip is pressed into the material with a certain loading- $\dot{P}$ or indentation strain rate $\dot{\varepsilon}$ up to a peak load P_{max}. The surface deforms elastically and around the indent a plastic zone is formed. The elastic displacements are recovered and the final depth of the residual hardness impression h_f remains, when the indenter is fully withdrawn. Figure 2.9 (b) shows a cross section with the used analysis parameters of this indentation process.

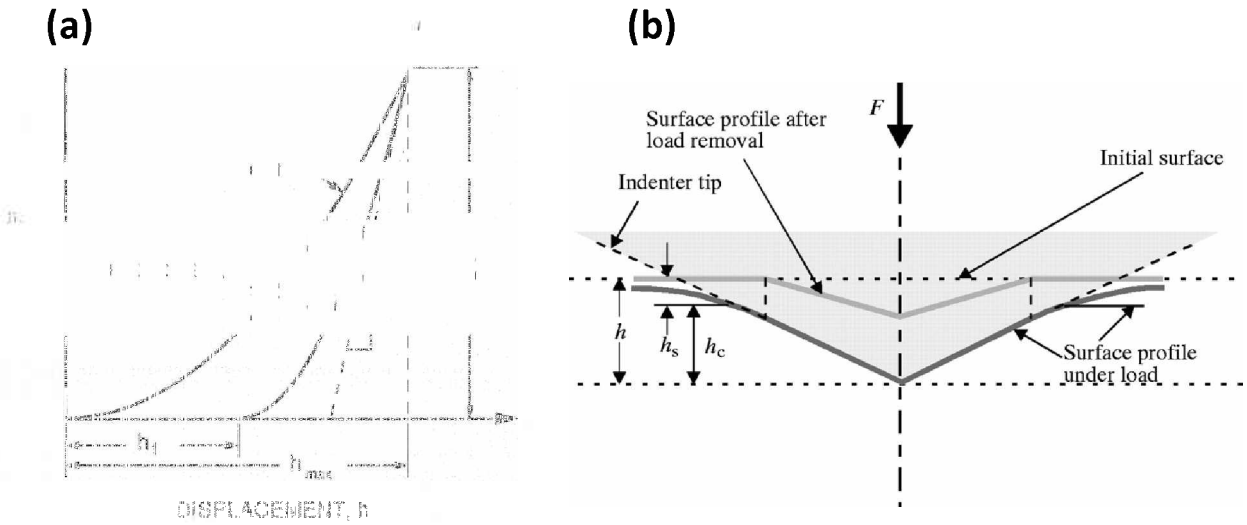

Figure 2.9: (a) Schematic of a load-displacement curve. (b) The indentation process and contact area during and after the indentation process [33].

The following equations describe the calculus of hardness and the Young's modulus [34]. For the evaluation of the hardness and Young's modulus it is essential to determine the contact depth h_c. This is the difference between the maximum indentation depth h_{max} and the elastic recovery h_s (Figure 2.8):

$$h_c = h_{max} - h_s \tag{8}$$

Hereby the maximum depth h_{max} can be obtained directly from the load-displacement curve, and the elastic recovery h_s can be determined from Sneddon's elastic contact theory [35]. The elastic deformation is dependent on the tip geometry and can be described by the following equation:

$$h_s = \varepsilon \cdot \frac{P_{max}}{S}, \tag{9}$$

where ε is a geometrical factor (for a Berkovich indenter ε = 0.75) and S the contact stiffness. Combing equation (8) and (9) results in:

$$h_c = h_{max} - \varepsilon \cdot \frac{P_{max}}{S}, \tag{10}$$

The unloading curve can be fitted with the following equation

$$P = B \cdot \left(h - h_f\right)^m, \tag{11}$$

using the fit parameters B, m and h_f. The contact stiffness is calculated out of the derivative of the fitted function at the depth at the peak load P_{max}.

$$S = B \cdot m \cdot \left(h - h_f\right)^{m-1}\Big|_{h_{max}} \tag{12}$$

The contact area A_c of the tip can be described with following function after the calibration on a reference material:

$$A(h_c) = a_0 h_c^2 + a_1 h_c + a_2 h_c^{1/2} + a_3 h_c^{1/4} + \cdots, \tag{13}$$

where a_o is a geometrical constant dependent on the geometry of the tip and the other constants a_i are describing the geometrical deviation of an ideal tip.

Finally the hardness and the reduced modulus E_r are obtained from the following equations:

$$H = \frac{P_{max}}{A_c}, \tag{14}$$

$$E_r = \frac{\sqrt{\pi}}{2\beta} \cdot \frac{S}{\sqrt{A}}, \tag{15}$$

where β is a depth independent geometrical factor (for a Berkovich indenter β = 1.034).

The reduced Young's modulus combines the elastic properties of the tip and the sample, and is associated with the Young's modulus by

$$\frac{1}{E_r} = \frac{1-\nu^2}{E} + \frac{1-\nu_i^2}{E_i}. \tag{16}$$

Hereby E and ν are Young's modulus and Poisson's ratio of the sample, and E_i and ν_i of the indenter tip, respectively.

A more detailed explanation for the whole calculus is given in [33].

Often it is important to determine the flow stress from the indentation hardness for a quantitative macroscopic comparison to uniaxial tests. For the estimation of the flow stress from the hardness, the following equation can be used:

$$H = c^*_{\varepsilon_{rep=8\%}} \cdot \sigma_f \tag{17}$$

Hereby, H is the hardness, $c^*_{\varepsilon_{rep=8\%}}$ is the material-depending constraint factor, which links the flow stress with the hardness for a representative strain ε_{rep} of 8 % in the case of a Berkovich indenter, and σ_f is the flow stress. A fixed constraint-factor of 3 is often used in the literature. But in recent publications, Atkins, Tabor and Hay et al. [36,37] have shown that the constraint factor is dependent on the ratio of E/σ_f and the ratio of the residual depth of indentation to the total depth, h_f/h_{max}, of the investigated material. For fully-plastically deforming materials like Al or Ni, where the ratio E/σ_f is very large or h_f/h_{max} close to 1, a constraint factor of 2.8 was determined. On the contrary, fused silica has a $c^*_{\varepsilon_{rep=8\%}}$ value of 1.5. In general, the following distinction of different constraint factors can be made as suggested by Johnson et al. [38]:

- Fully elastic deformation: $c^* < 1.07$
- Elastic and plastic deformation: $1.08 < c^* < 2.8$
- Fully plastic deformation: $c^* > 2.8$

2.3.3 Strain rate sensitivity and activation volume

The rate dependent deformation mechanisms and the underlying movement of dislocations can be obtained by strain rate jump-tests, relaxation tests, or creep experiments. These tests are usually based on compression or tensile experiments. Beside these methods, novel

nanoindentation techniques have been developed in order to obtain local deformation mechanisms in a material. There are several characteristic properties of a material that can be used for an understanding and description of the ongoing time and strain rate dependent mechanisms inside the material. The strain rate sensitivity *m* and the activation volume *A* are two of those characteristic properties. During an indentation experiment, the correlation between the stress σ and the strain rate $\dot{\varepsilon}$ can be described by Norton's power law [39]:

$$\sigma = k \cdot \dot{\varepsilon}^m . \tag{18}$$

In this equation, *k* is a proportionality constant. Correspondingly, the strain rate sensitivity is [40,41]:

$$m = \frac{\partial \ln \sigma}{\partial \ln \dot{\varepsilon}} \sim \frac{\partial \ln H}{\partial \ln \dot{\varepsilon}} \sim \frac{1}{n} \tag{19}$$

Here *n* is the often-used strain-hardening exponent. The strain rate sensitivity for coarse-grained FCC metals is about 0.001 [42] and the strain rate-dependence of the deformation behavior is very low. Contrarily, the strain rate sensitivity for UFG or NC FCC metals is larger than 0.01 [42], respectively one order of magnitude higher due to a higher fraction of grain boundaries. The rate-dependence of the material deformation is influenced by dislocation activities, grain boundary diffusion and lattice diffusion [43]. For CG FCC metals, forest lattice dislocations dominate the plastic deformation, which results in low strain rate sensitivities. Generally, the contribution of lattice diffusion is negligible at RT, but gets more important at elevated temperatures.

By using creep or relaxation measurements, the activation volume *A* can be associated with [44]:

$$A = \sqrt{3}kT \frac{\partial \ln \dot{\varepsilon}}{\partial \sigma} \cong c^* \sqrt{3}kT \frac{\partial \ln \dot{\varepsilon}}{\partial H} \tag{20}$$

The activation volume gives information about dislocation obstacles during plastic deformation [42] and can be calculated with:

$$A = b \cdot d \cdot l. \tag{21}$$

Hereby, *b* is the Burgers-vector, *d* the displacement of the dislocation segment and *l* the length of the dislocation segment. High activation volumes (1000 b^3) can be related to forest dislocations [42], while very small activation volumes for NC or UFG materials can be linked to thermally activated dislocation movements at grain boundaries such as grain boundary sliding

mechanisms (A = 1 b^3, m = 0.5 [45]) and Coble creep (m = 1.0 [46]). With a decrease of the grain size to the submicron regime, the forest cutting mechanism is suppressed because of the large amount of grain boundaries and/or sub-grain boundaries, which serve as strong influencing obstacles to dislocation motions. With both parameters, m and A, important conclusions about local time and strain rate dependent deformation mechanisms can be made. In recent studies on FCC, UFG, and NC metals a decrease of the activation volume with increasing temperature in a temperature range of 100 K up to 400 K has been observed for Cu and Ni [47,48]. Such temperature dependence of A is quite different from that of CG (coarse grained) materials. This unique phenomenon can be explained by dislocation sources in grain boundaries, which control the motion of dislocations in UFG and NC metals [42].

During this diploma thesis nanoindentation stress relaxation tests are used to obtain m and A. Beside the stress relaxation tests, there are also two other techniques to measure m. The first method, proposed by Mayo and Nix, uses a constant rate of loading (CRL). Another technique is the constant strain rate (CSR) method, which was proposed by Lucas and Oliver and uses an exponential load–time function to produce a steady strain rate. However, both of these methods require many indentations to obtain the necessary strain rate - hardness pairs for the calculation of m. By using strain rate jump tests, one can overcome this weakness [34], using a series of exponential loading rates to generate several strain rate and hardness pairs. But the most popular technique is still the constant load (CL) method of Mayo et al. [49,50], which uses a holding segment at a fixed peak load to achieve continually changing strain rate and hardness pairs. This allows the calculation of strain rate sensitivity from a single indent, and therefore less indents and a smaller area on the sample surface are required. In a couple of studies [51–53] a good correlation of values obtained using the CL method and bulk literature values has been reported.

The data evaluation for the stress relaxation measurements presented in this work is performed with the following theoretical approach [51]. The hardness and strain rate are obtained from:

$$H = \frac{P}{A_c}, \tag{22}$$

$$\dot{\varepsilon} = \frac{\dot{h}}{h_a}. \tag{23}$$

Here, h_a is the absolute indentation depth, $\dot{h}$ is the displacement rate, P is the applied load, and A_c is the projected area of the indent. The size of the projected area depends on geometry of the indenter tip. Thus, a calibration of this tip is necessary. The instantaneous area is

determined from instantaneous total depth and is used for a continuous hardness calculation during the test. Figure 2.10 shows the indentation depth and load curves for the dwell period of an indent. This depth-time curve of the dwell period can be separated into two distinct regions, called Stage *a* and Stage *b*. Stage *a* shows a rapid increase in the indentation depth and Stage *b* a rather linear increase of the indentation depth, while the load is kept constant. These two regimes are sometimes referred to as a transient (Stage *a*) followed by a steady-state regime (Stage *b*). Measured *m* values are mainly taken from of this regime, which is assumed to be more stable, and results of Stage *a* are often discarded. In a recent publication of Peykov et al. [51], a good correlation between *m* values obtained from Stage *a* and literature *m* values for bulk samples, was observed for different materials including Cu. Peykov et al. found several advantages of using Stage *a*:

- No load dependence
- No significant influence of thermal drift

In this present work, *m* values are obtained from Stage *a* and Stage *b*.

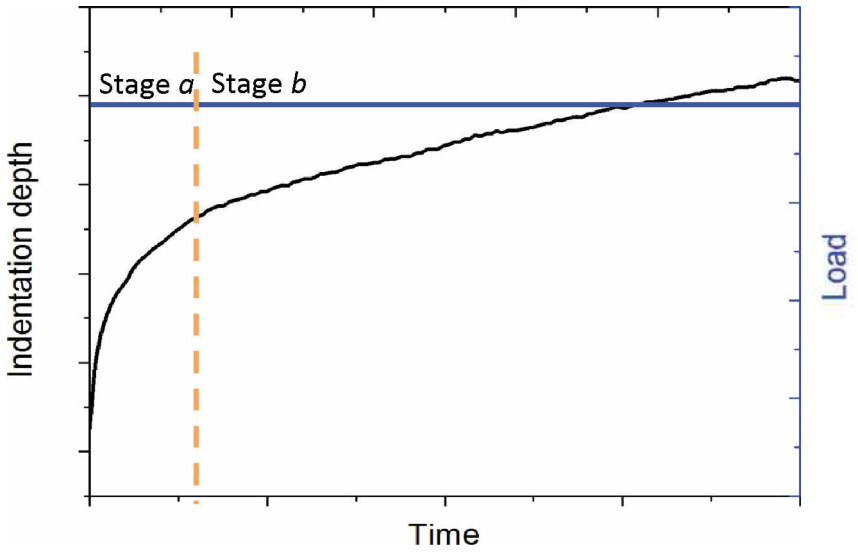

Figure 2.10: Indentation depth and load over time curve with the distinct regimes of the dwell period.

2.4 Oxidation behavior of Cu

The oxidation behavior of Cu is not well investigated, especially for NPC. Oxidation of NPC can strongly influence material properties due to the high surface-to-volume ratio even at low temperatures. During this work, oxidation of the NPC was observed and further study of Cu-oxidation deemed necessary. Figure 2.11 shows an oxidation model for bulk copper. Hereby, a layered structure of different copper oxides can be observed for different temperature re-

gimes, whereby Cu_3O_2 is a mixed oxide consisting of CuO and Cu_2O. The different stages are shown in Figure 2.11 and are classified into different temperature regimes: (1) below 70°C, (2) 70–110°C, (3) 110–200°C, (4) 200–270°C, and (5) 270–330°C. In stage (1) the oxidation starts with the formation of the Cu_xO structure developed between ambient temperature and 70°C. Stage (2) oxidation apparently produces Cu_2O over the precursor oxide Cu_xO. In stage (3) Cu_3O_2 is formed, but no Cu_2O exists below this layer with the exception of the precursor oxide; a defect structure of Cu_2O. Oxidation in stage (4) produces CuO, in the presence of Cu_2O and Cu_3O_2. Oxidation at 200°C and above produces at least three oxides Cu_2O, Cu_3O_2 and CuO with the outer layer being a mixture of CuO and Cu-(I) oxide. Oxidation in stage (5) produces CuO over Cu and the lower copper oxides [54]. Further oxidation at 400°C mainly forms Cu_2O [55].

Figure 2.11: Model for the oxidation behavior of Cu at elevated temperatures [56].

Table 1 shows an overview of the different copper oxides and their properties. In a further work [57], the oxidation of NPC was examined. The following equation allows an approximation of the oxide thickness on the ligaments in air [57]:

$$d_{oxide}(t) = A \cdot exp\left(\frac{-Q}{R \cdot T}\right) \cdot \sqrt{t} + d_0, \tag{24}$$

where $d_{oxide}(t)$ is the thickness of the formed copper oxide as a function of time, $R = 8.314 \cdot 10^{-3}$ kJK^{-1} mol^{-1} is the gas constant, T is the temperature, t is time in minutes, d_0 is the initial copper oxide thickness (approximately 4 nm for a natural oxide layer). The activation energy Q for the formation of copper oxide was found empirically and is shown in Table 2. The initial coefficient A is $5.518 \cdot 10^5$ Å $\cdot min^{-0.5}$ for 100°C and 200°C, and $4.85 \cdot 10^5$ Å $\cdot min^{-0.5}$ for 300°C and 400°C [58,59].

Table 1: Properties of different copper oxides [56-59].

Oxide	Hardness [MPa]	Young's modulus [GPa]	Density [g/cm^3]	Crystal structure
CuO	2050–2490 [59]	81.6 [60]	6.45 [61]	Monoclinic [61]
Cu_2O	2010–2030 [59]	30.1 [62]	6.15 [61]	Cubic [61]

Table 2: Activation energies for the formation of copper oxide [55,58,59].

Temperature [°C]	Activation energy Q in air [kJ/mol]	Activation energy Q in Ar + 1% O_2 [kJ/mol]
100	33	-
200	33	-
300	42	58
400	42	58

The crystal structures of CuO and Cu_2O are monoclinic and cubic. Cu_2O has a complex crystal structure. The oxygen ions are ordered on a BCC cubic lattice and the copper ions occupy the positions of a FCC cubic lattice. The structure consists of two completely intertwined and identical frameworks, which are not cross-linked by any primary Cu-O bonds. Regarding the deformation of copper oxides, only the deformation behavior of Cu_2O has been investigated in prior studies [63–65]. It has to be mentioned that the dislocation dynamics is very sophisticated due to the complex crystal structure. The polycrystalline cuprous oxide is ductile at temperatures over 350°C, and brittle at lower temperatures. Therefore, extensive plastic deformation is not observed at low temperatures and dislocation movement is restricted. There have not been prior studies on CuO and Cu_3O_2 regarding deformation mechanisms.

3 Experimental Procedure

This chapter will give an overview of the experimental procedure for the whole material manufacturing route, microstructural characterization, and mechanical testing of the foam. The process includes compacting the powder to disk shaped specimens, heat treatment, preparing and dealloying the disks, and finally testing the resulting foam at different temperatures and strain rates.

3.1 High pressure torsion

The first step of the manufacturing chain was to create a disk shaped bulk sample from a powder mixture, which can be later used for another deformation step. The basic raw materials for the HPT process were copper powder (99.9% purity, - 170 + 400 mesh, 37-88 µm) and iron powder (99.9% purity, - 100 + 200 mesh, 74-149 µm). The two different powders were premixed in a ratio of 50 at. % Cu and 50 at. % Fe ($Cu_{50}Fe_{50}$). The powder mixtures were prepressed and deformed to a disk shaped specimen in a large HPT tool at room temperature. Severe strain was imposed through 20 revolutions under constant pressure of 2.4 GPa. This compacted disk was 50 mm in diameter and 9.6 mm thick and was used for cutting out a rod with 8 mm diameter at a radius between 5 and 15 mm. The rod was used for making small slices with a diameter of 8 mm and thickness of 0.8 - 0.9 mm for a second HPT deformation step in order to get a homogenous and fine microstructure. These small slices were deformed through 200 revolutions with a rotation speed of 0.6 turns per minute under a constant pressure of 7.8 GPa in a small HPT tool at RT. An air-cooling system was used to keep the temperature constant during the deformation process. The single steps of the specimen production are shown in Figure 2.2 [4].

The microstructure of the HPT-processed specimen disks was characterized by a light microscope (LM; Olympus BX51, Olympus Corporation, Japan) and scanning electron microscope (SEM; LEO type 1525, Carl Zeiss GmbH, Germany) after the second HPT step. A backscattered electron (BSE) detector was used for gray scale based phase separation by making use of the different scattering factors. The aim of the two-step HPT-process was to obtain a

fine and homogeneous microstructure. Therefore, during this diploma thesis all microstructural investigations were made in an axial and/or tangential direction at a radius of 3 mm due to the high-grade of deformation at this radius. The investigations were always performed with the before mentioned LM and SEM and at least in one of both directions to characterize microstructure variations due to the shear texture evolving during the HPT process. The directions of the microstructural examinations are given in Figure 3.1. For the examination the disks were warm-embedded in an electrically conductive polymer, and subsequently ground and polished down to 1 µm. Afterwards, a further polishing of the polished disks with a 0.05 µm colloidal silicon oxide suspension was performed.

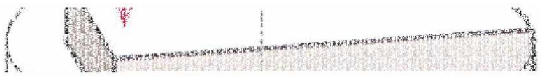

Figure 3.1: Directions of the microstructural observations [66].

3.2 Heat treatment

In order to prepare the samples for selective dissolution and to reduce the amount of forced mechanical mixing between Cu and Fe, a heat treatment was conducted at 500°C for one hour in a vacuum furnace (SERIES XRETORT, Xerion Advanced Heating Ofentechnik GmbH, Germany). The pressure never exceeded $3 \cdot 10^{-4}$ mbar during the heat treatment. The heating rate of the furnace was 10°C per minute and the cooling down to RT required eight hours. After the heat treatment an investigation of the microstructure was performed again in tangential direction using the LM and SEM.

3.3 Sample preparation

The next step was to prepare the disk specimens for nanoindentation experiments. Therefore, samples were fixed with a double-faced adhesive tape on small sample holders for subsequent preparation. The aim was to create a homogenous area of the sample, which is located in the middle of the disk height, since the deformation is mostly homogeneous and defined in this zone. The specimens were ground down from a starting thickness of 0.6 - 0.8

mm to 0.3 - 0.4 mm, as shown in Figure 3.2, and subsequently polished with 9 µm, 3 µm and 1 µm diamond suspension. After the polishing, a 0.05 µm colloidal silica oxide suspension was used for preparing the disks for nanoindentation. Subsequently, the round samples were quartered into four similar pieces with a water-cooled diamond wire saw as shown in Figure 3.2.

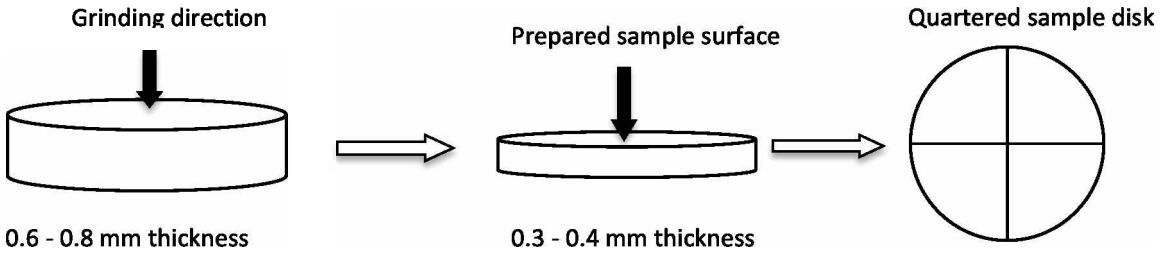

Figure 3.2: Schematic sketch of the sample preparation. The height of the sample is reduced exactly to the center of the HPT disk to perform the indentation experiments in the middle of the origin sample.

3.4 Foam processing

The bulk nanoporous copper (NPC) was prepared using a free corrosion process by selective dissolution of the iron. During nanoindentation experiments non-porous regions should not influence the plastic-zone and therefore a certain dealloying depth is necessary to perform nanoindentation properly without influence of the underlying non-porous material. The aim was to dealloy the quartered specimens at least 50 microns from both sides in order to reach the mentioned non-influencing depth level. The inner part of the samples should not be porous in order to later prevent sponging of the high temperature fixing cement for nanoindentation. For this dealloying process the polished slices of $Cu_{50}Fe_{50}$ were emerged in 5 wt.% hydrochloric acid (HCl) for 35 hours at a temperature of 55°C and opened to air. After 35 hours the samples were removed from the solution and cleaned in Acetone and Ethanol to remove the residual HCl-solution. Cross-sectional ion polishing was performed to check the reached dealloying depth and porosity quickly and without damaging the material as shown in Figure 3.3. The ion polishing was done with an argon ion milling System (E-3500 Ion Milling, Hitachi High Technologies Pte Ltd, Japan) for eight hours. The white area in Figure 3.3 shows the size of the Ar ion polished region and the arrow indicates the direction of incoming ions.

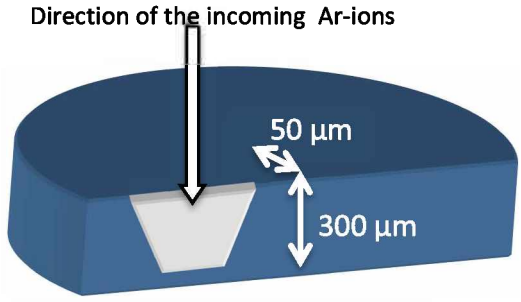

Figure 3.3: Sketch of the half of the whole sample, which was emerged to 5 wt.% HCl for 35 hours and ion polished 3 mm outside of the center.

3.5 Foam characterization

After the dealloying process the morphologies and structures of the NPC were investigated to confirm a successful dissolution process. The microstructural investigations were performed in an axial direction using an SEM equipped with an energy dispersive X-ray spectroscope (EDX) or a dual beam FIB-SEM (Qanta 3D FEG, FEI, USA). The remaining iron was determined by EDX. EDX spectra were collected for the NPC over a certain axial region to check the remaining Fe concentration.

A further method to get information about the porosity is to obtain the relative density from micrographs. SEM pictures were processed using the computer software Analysis (AnalySIS Pro 5.0, Olympus Soft Imaging Solutions GmbH, Germany) to prepare the images for a professional phase separation. The first step of this process contained the change of normal image into a grey scale image. Then a band-pass filter was used to remove variation in brightness. The next step was the binarization of the image into pores and struts for a phase distinction. The algorithm for differentiation between the two phases was proofed by manually drawing and differentiating copper from pores.

Later, local cross-sections were performed with a FIB (Focused Ion Beam) using Gallium ions, additionally to the ion polishing method of investigating the structure and morphology beneath the surface of the foam.

3.6 Nanoindentation

The mechanical and deformation properties were tested using a nanoindenter (Micro Materials NanoTest Platform 3, Micromaterials, UK) with a high temperature option at the Department for Nuclear Engineering in Berkeley, CA, USA (Figure 2.8a)). The machine was placed into an environmental chamber purged with high purity argon to reduce the oxygen level below 2% aiming to minimize oxidation of the sample. The measurements, data record-

ing and data evaluation were carried out with the software "NanoTest Platform Three", Origin and Microsoft Excel.

3.6.1 Preparations for nanoindentation

For RT measurements the samples were fixed with super glue on a common sample holder. For the high temperature measurements the specimens were mounted onto the heatable sample stage with a special high temperature cement Omegabond 600 (Omega Engineering Inc., Stamford, USA) as shown in Figure 3.4. The heating system of the indenter consists of resistance heaters on the sample stage and the indenter tip, as shown in Figure 3.5. Two thermocouples were mounted, on the sample surface of a reference specimen close to the measured sample and directly above the resistance heater of the heating stage to control the temperature accurately. A second heating element and thermocouple were used to control the temperature of the indenter in order to minimize thermal fluctuations during indentation. Additionally, a water-cooled heat shield was used to reduce the thermal drift as shown in Figure 3.5.

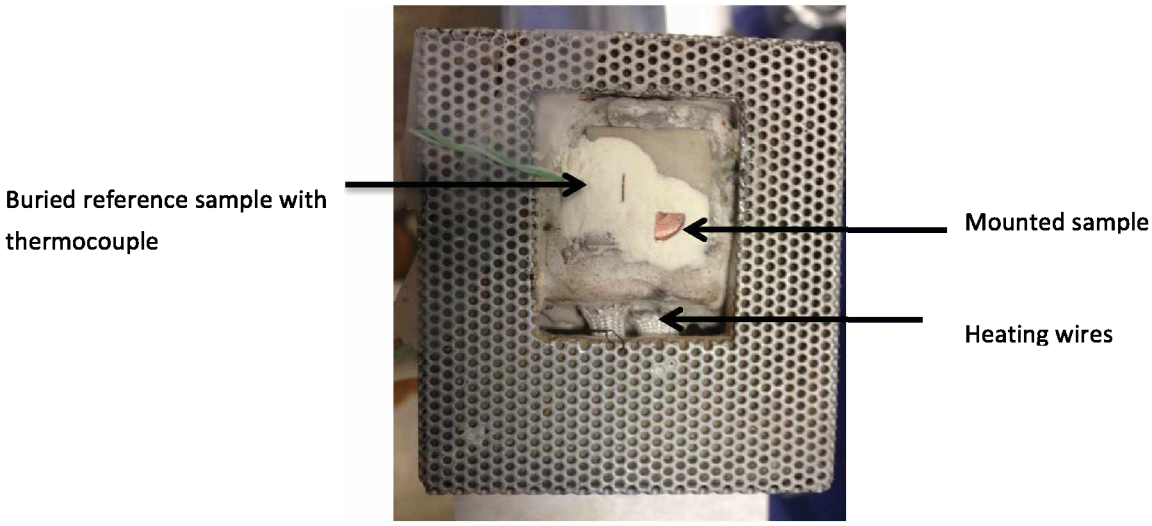

Figure 3.4: Heatable sample stage with a mounted sample and reference sample surrounded by high temperature resistant cement. The thermocouple is fixed on the reference sample.

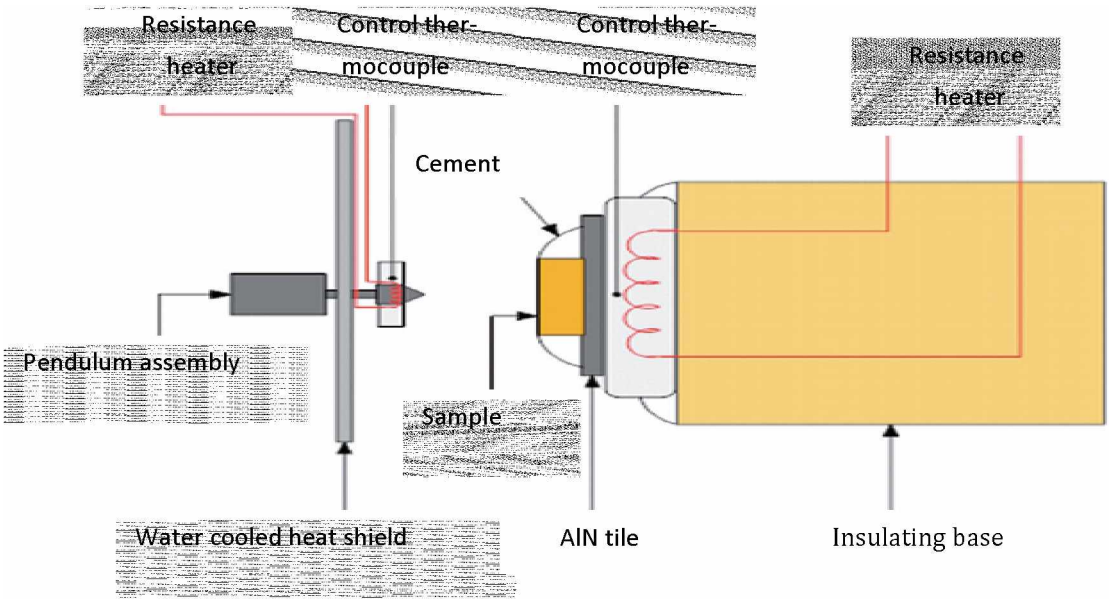

Figure 3.5: Schematic shows the separately working water cooled heating system of the tip and the sample stage [32].

3.6.2 Conducted indentation experiments

Indentations were performed at RT, 50°C, 100°C, 200°C and 300°C in argon atmosphere (oxygen content < 2 %). For the high temperature measurements of up to 300°C, a cubic Boron Nitride (cBN; mechanical properties: E = 800 GPa, ν = 0.12) Berkovich indenter was used in an argon atmosphere. After measurements at elevated temperatures were acquired, all the used samples were measured again with a diamond (mechanical properties: E = 1141 GPa, ν = 0.07) Berkovich indenter at RT to get information about changes of the microstructure. Indentations were performed on the planar, "polished surfaces" of the samples. The tip calibrations were performed on fused silica (E = 72 GPa, ν = 0.18) before and after each high temperature indentation experiment. Before each experiment the floating table was brought into an equilibrium position for minimizing vibrations. All measurements were conducted at a radius of 3 mm from the center of the sample and the distance between the indents was 50 µm as shown in Figure 3.6.

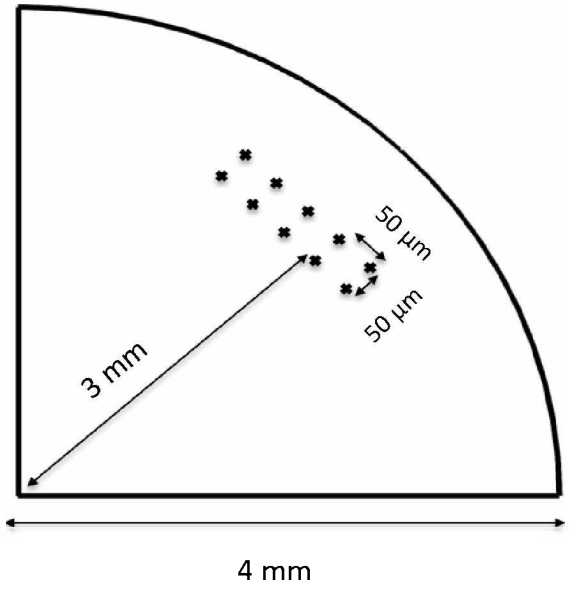

Figure 3.6: Schematic sketch of the positioning of the indents.

An overview of the parameters used for all conducted experiments is shown in Table 3, while Figure 3.7 shows the schematic correlation between the load and time for the all experiments. Depth sensing nanoindentation was performed to 2000 nm with a constant strain rate of 0.1 s^{-1} in order to achieve reference values for the hardness and Young's modulus of the NPC. The dwell segment for the depth-controlled measurements was 30s (Figure 3.7) and the unloading rate was 10 mN/s. Constant load relaxation tests were performed to determine the strain rate sensitivity *m* of the material. For the determination of *m* it is essential to test a similar volume. Thus, for the experiments loads of 8 mN were used for the RT measurements at the beginning, and 30 mN for the high temperature tests and RT tests after high temperature nanoindentation due to an increase of hardness during the heating. For all constant load measurements a dwelling time of 200 s (Figure 3.7), a loading time of 10 s and unloading time of 5 s were used. A minimum of 10 indents per temperature and condition were performed tangential as shown in Figure 3.6. The 60 s thermal drift correction was performed post-indentation at 10% of the maximum peak load. The last 60 % of the recorded drift data was used for the thermal drift correction. The thermal drift of all measurements was below 0.3 nm/s.

Table 3 Overview of the used parameters and conditions for the conducted measurements.

Parameters/Measurements	Load Controlled (LC) (a)	Load Controlled (LC) (b)	Depth Controlled (DC) (c)
Depth/Load	8 mN	30 mN	2000 nm
Dwell Time	200 s	200 s	30 s
Loading Time	10 s	10 s	-
Strain rate	-	-	0.1 s^{-1}
Unloading Time	5 s	5 s	-
Unloading Rate	-	-	10 mN/s
Calculated parameters	*m*	*m*	*E, H, m*

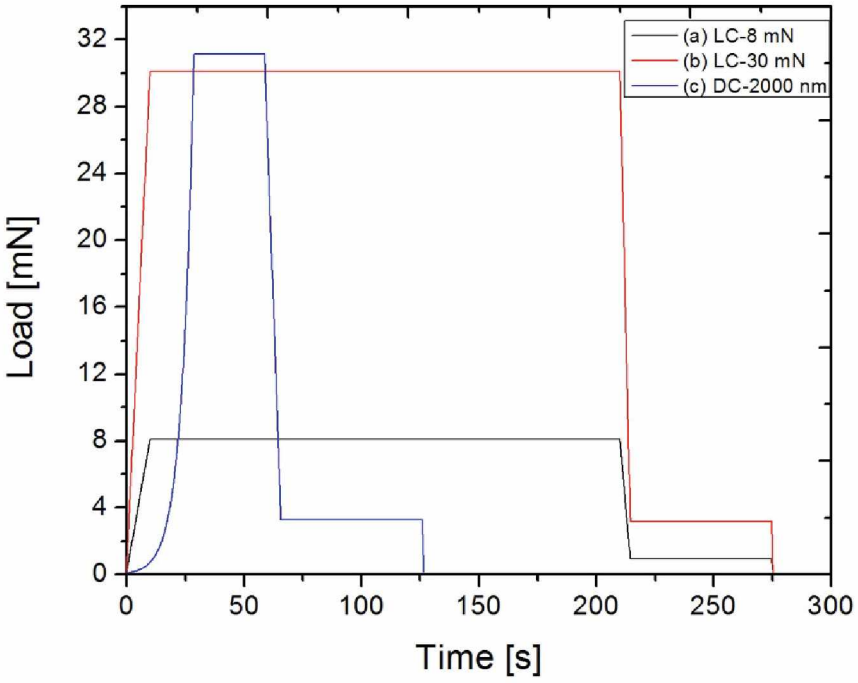

Figure 3.7: The load over time correlation for the three different nanoindentation set-ups in Table 3 (a), (b) and (c).

3.6.3 Evaluation of the strain rate sensitivity and activation volume

Measurements with dwell times of 30 s and 200 s were performed for obtaining information about the rate controlling deformation mechanism of the material. The changes in hardness and strain rate during the dwell period allow the calculation of the *m* and *A* values.

With both parameters, conclusions about local time- and strain rate-dependent deformation mechanisms can be made. The following paragraph explains the evaluation of *m* and *A*.

The relative depth-time curves of each indent were fitted with the following empirical function:

$$h_r(t) = A \cdot |h - x_c|^P, \tag{25}$$

where h_r is the relative indentation depth, h the actual indentation depth, and A, x_c and P are fitting parameters. For Stage *b* all the data (200 s) were fitted (Figure 3.8), while for Stage *a* just the first 20 s were used to obtain an accurate fit (Figure 3.9). The reason for this approach was that the density of recorded values in the first regime is less than in Stage *b*. Therefore, the best and most accurate results of the fits were achieved by two distinct fits. The *m* values for each regime were calculated and compared to each other. The least-square method was used to fit the depth-time curves. The absolute depth h_a must be used for the further calculation of the displacement rate.

$$h_a(t) = h_r(t) + h_0 \tag{26}$$

Hereby h_0 is the depth of the beginning of the dwell period.

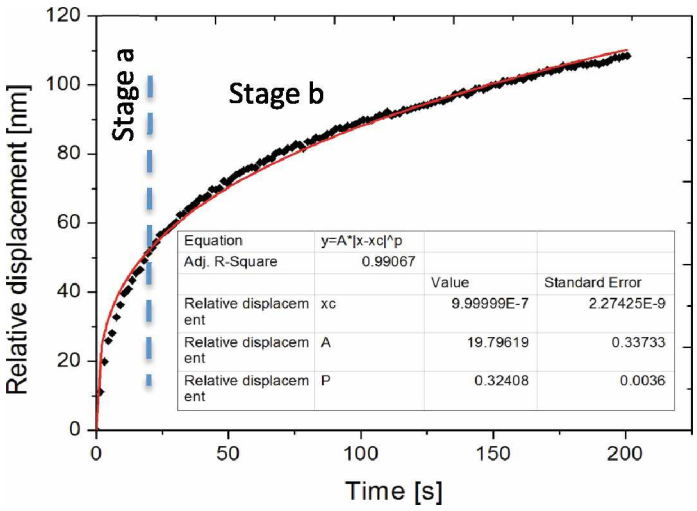

Figure 3.8: Relative depth of the dwell segment and the corresponding depth-time fit for 200s. The dashed blue line separates the two distinct regimes. The table insert shows the resulting fitting parameters.

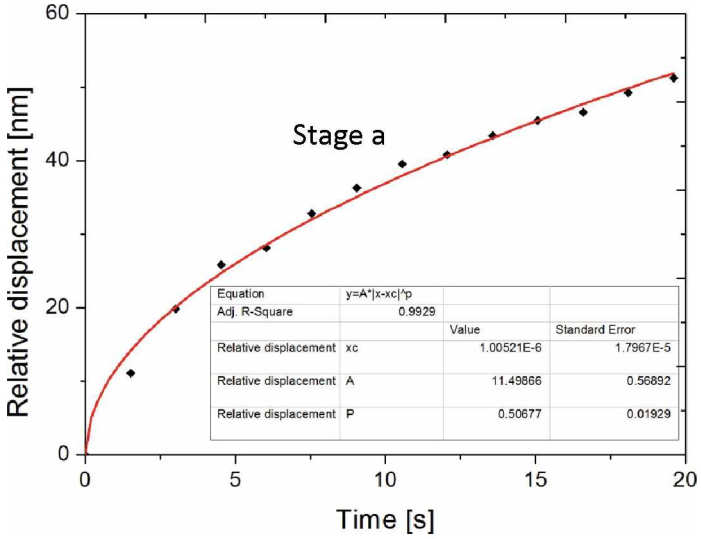

Figure 3.9: Relative depth of the dwell segment and the corresponding depth-time fit for 20 s (Stage *a*). The table shows the resulting fitting parameters.

The instantaneous displacement rates $\dot{h}_a$ were achieved from the derivative of this fitted curve and then the strainrates $\dot{\varepsilon} = \frac{\dot{h_a}}{h_a}$ were calculated from equation (22). The current hardness values were obtained with equation (21) from the average load during the hold segment and the projected area (obtained from the original data). As requested by equation (18), the hardness and strain rate were plotted in a double natural logarithmic plot to achieve the *m* value by two linear fits for each regime. Hereby, the *m* values for Stage *a* were assessed from the recorded data of the first 20 s, and the linear fit of Stage *b* included data between 30 s and 200 s. The data of the transient region between 20 s and 30 s was discarded. Finally, activation volume was obtained for each regime by using equation (19).

3.7 X-ray diffraction measurements

In the present work oxidation of the open-cell NPC foams occurred. In order to verify the oxide type and temperature of oxide formation, besides confirming increased oxygen content with EDX on the sample surface after the high temperature nanoindentation, the oxide was examined by XRD (X-ray diffraction). Previous studies in bulk copper showed that XRD can be used to follow the formation of the different copper oxides ex-situ [57]. In the present work the XRD measurements were performed with a X-ray diffractometer (Smartlab X-RAY DIFFRACTOMETER, Rigaku Corporation, Japan) on a polished sample surface in air. First an ex-situ experiment was performed on a non-oxidized sample and an oxidized sample after 300°C for six hours, respectively, to identify peak positions of distinct elements and chemical compounds, and intensities at 25°C. This experiment was also used to find the best conditions for performing more demanding in-situ heating experiments in air. The further proce-

dure was the XRD in-situ measurement of a non-oxidized sample, where the temperature was raised in 20°C steps with a short holding segment for obtaining the XRD spectra. The measured temperature profile is shown in Table 4, whereby the heating rate was 2°C per minute.

Table 4: Temperature steps for the in-situ XRD measurements to study oxidation of NPC.

Temperature [°C]	Holding time [Minutes]
25	10
40	10
60	10
80	10
100	50
150	10
200	10
250	10
300	10

4 Results

4.1 High pressure torsion processing

Fully dense two phase supersaturated solid solution Fe-Cu nanocomposites are obtained by a two-step HPT process, as observed by Bachmaier et al. [67]. Figure 4.1 shows the deformed microstructure after the deformation process for $Fe_{50}Cu_{50}$ in the SEM. The Fe and Cu phase can be easily distinguished due to the lower scattering factor of the Fe phase. Thus, the brighter appearance of the Cu-phase and the bands of Fe and Cu rich regions can be easily distinguished. The thickness of the bands shown below is several hundred nanometers.

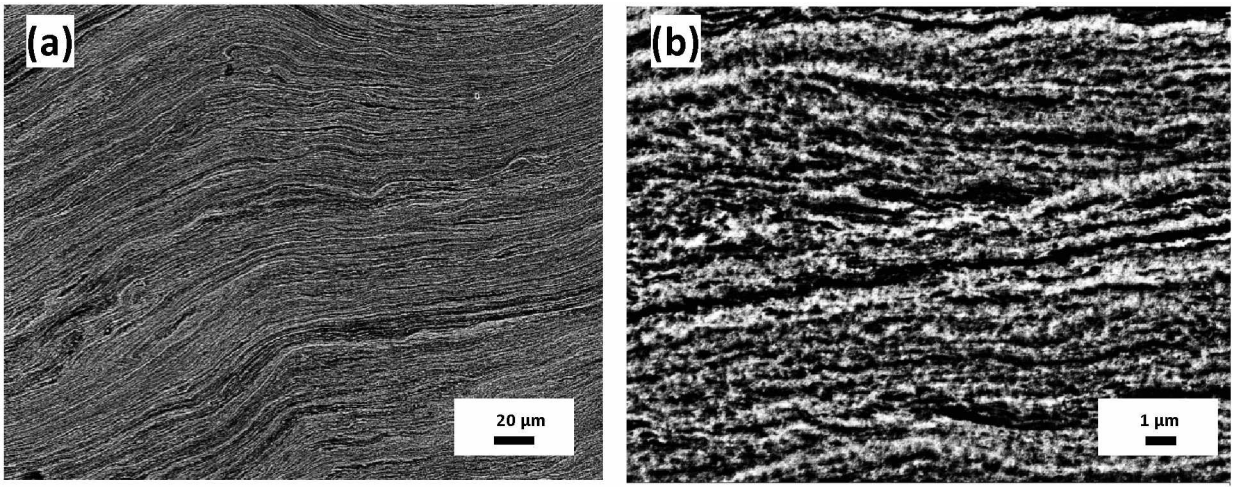

Figure 4.1: SEM images (back scattered electron mode) showing the microstructure of the $Fe_{50}Cu_{50}$ before heat treatment after the second deformation step at a radius of 3 mm in tangential direction. Fe rich regions appear darker, Cu regions brighter. (a) Microstructure with low magnification and (b) with higher magnification.

Figure 4.2 shows the microstructure in axial direction in the light microscope after the heat treatment. The difference of the microstructure over the radius can be seen, which is related to the differences in the imposed shear strains. The outer area of the sample gets most deformed and shows therefore a finer and more homogenous microstructure, as desired for further experiments.

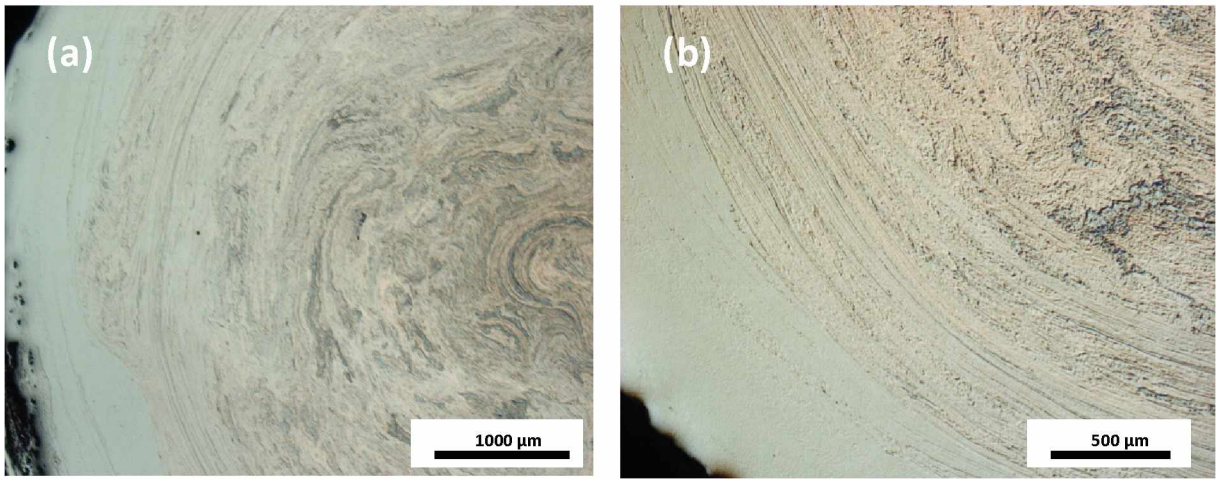

Figure 4.2: Light microscope images showing the deformation structure in axial direction after the heat treatment. (a) Low magnification overview of the microstructure of half the HPT disk. (b) Detailed micrograph of the outer area.

The imposed shear strain during the first and second HPT step can be calculated with equation (1). For this calculation the mean initial grain size d_0 is about 50 µm, the shear strain γ_1 of the first HPT step is ~ 130, and γ_2 for the second step is ~ 4200. The calculated band thickness with equation (3) should be about 0.02 nm. This calculation example shows that the equation can only be used up to a saturation deformation. After a certain number of turns the saturation grain size is reached, and the grain refining stops due to grain boundary migration and dynamic recrystallization processes [66]. Nonetheless, this demonstrates that our samples were deformed to a steady state where grain refinement saturation was reached.

Figure 4.3 shows the microstructure in tangential direction after the conducted heat treatment of 1 hour at 500°C. The band structure has changed during the heating process to a fine homogeneous structure. The decomposition of the supersaturated solid solution has occurred during the heat treatment, as also observed by Bachmaier et al. [67]. The grain size of the final structure is about 200 nm. Figure 4.4 shows the microstructure after the heat treatment in axial direction. The resulting band structure of the shear deformation process is partly remaining.

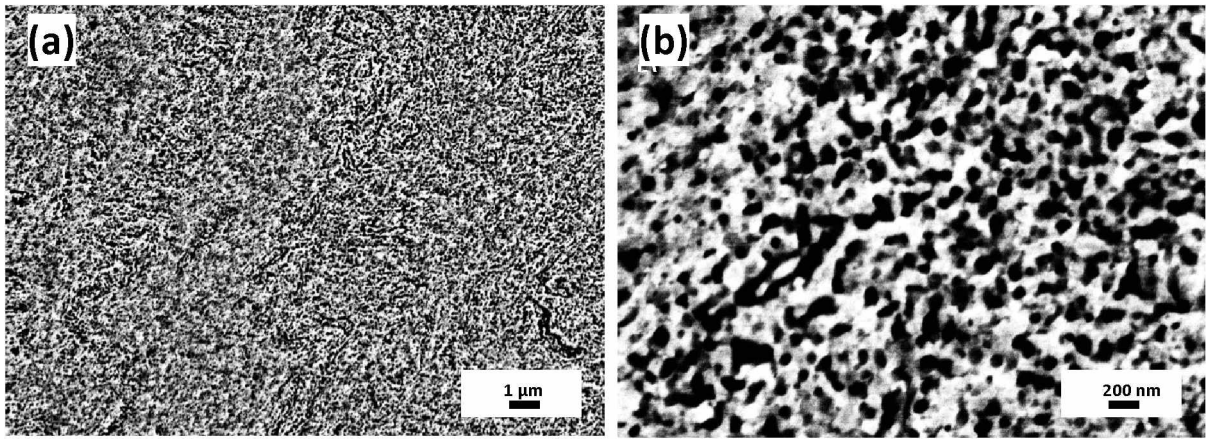

Figure 4.3: SEM images (back scattered electron mode) recorded tangential at a radius of 3 mm after heat treatment at 500°C for 1h. (a) Low magnification overview. (b) Detailed micrograph of the microstructure.

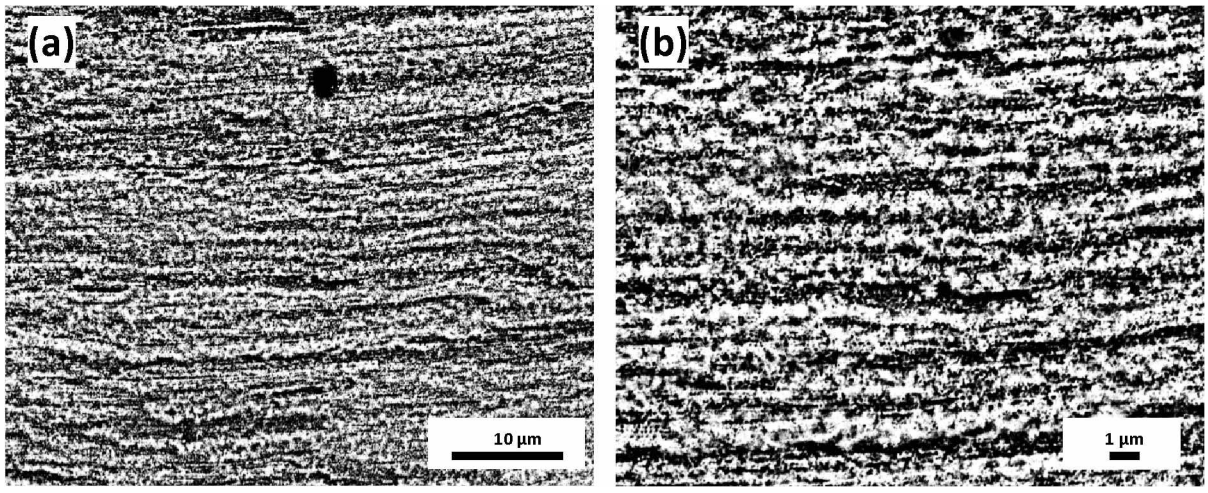

Figure 4.4: SEM images (back scattered electron mode) recorded axial at a radius of 3 mm after heat treatment at 500°C for 1h. (a) Overview of microstructure with a low magnification. (b) More detailed micrograph.

The aim of the heat treatment is to reach a decomposition of the supersaturated solid solution phases into a FCC Cu phase and a BCC Fe phase without grain growth. Bachmaier et al. observed that the decomposition of the supersaturated Fe phase starts at 300°C and ends at 480°C [67]. The decomposition of the supersaturated Cu phase also starts at 300°C, but ends at a temperature of 585°C [67]. Thus, some soluted Fe is still remaining in the Cu phase. Annealing at higher temperatures would lead to a full decomposition of the supersaturated Fe in Cu, but also to an undesired grain growth, which would potentially degrade the mechanical properties of the foam.

4.2 Foam manufacturing and characterization

The NPC is obtained by selective dissolution as detailed in chapter 2.2.1. During the immersion, hydrogen bubbles were generated as expected from the Pourbaix diagrams in Figure 2.4, hinting at a successful dissolution. The resulting structure after this process in axial direction is shown in Figure 4.5. The ligament size of the structure is about 200 nm, as was expected from the grain size of the composite. Both ligament width and pore size are not perfectly homogenous throughout the whole specimen related to manufacturing process.

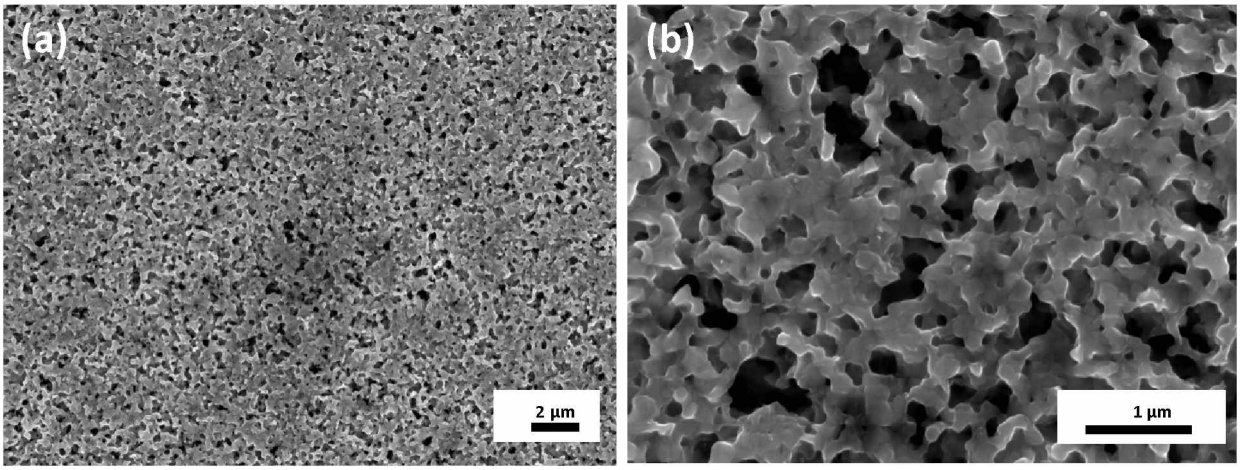

Figure 4.5: The images show the obtained structure in axial direction after the selective dissolution with a low magnification in (a) and high magnification NPC in (b).

Figure 4.6 (a) shows the ion-polished surface in tangential direction. The intensity distribution of the incoming argon ions can be identified by the resulting round structure. In the middle, most of the material is milled away due to the highest intensity of argon ions. This method serves as a quick-check for controlling the porosity without damaging the material. The velocity of the milling process should not be at a maximum level in order to get a consistently smooth milled area. The band-structure of the HPT-process can still be seen after the dealloying process, although a two-step HPT-process has been used. The detail highlighted in Figure 4.6 (a) is shown in higher magnification in Figure 4.6 (b), showing the dealloyed material. The image confirms the successful dealloying process and the reached dealloying depth of at least 50 µm for nanoindentation. Figure 4.7 shows a local FIB cross-section under an indent, which also confirms the reached dealloying depth and the layered structure of the HPT deformation. The bright and non-porous zone on the top of the imprint is a locally sputter deposited Platinum protective layer (Figure 4.7) to avoid material removal near the surface and curtaining of the cross-section. The deformed area below the imprint will be discussed later in chapter 4.3.3.

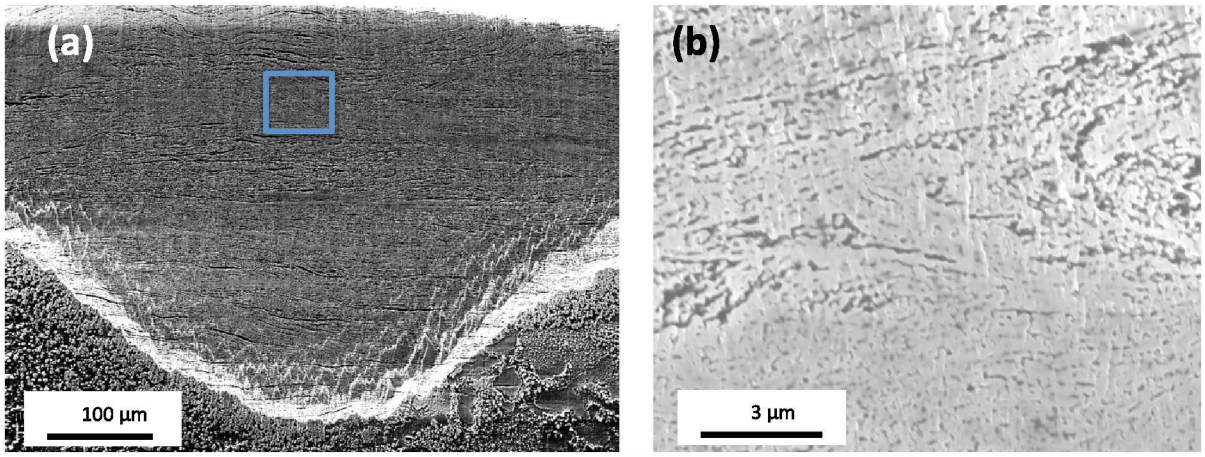

Figure 4.6: SEM images of the ion-polished area of a dealloyed. (a) Overview. (b) Detailed micrograph of the marked area of image (a).

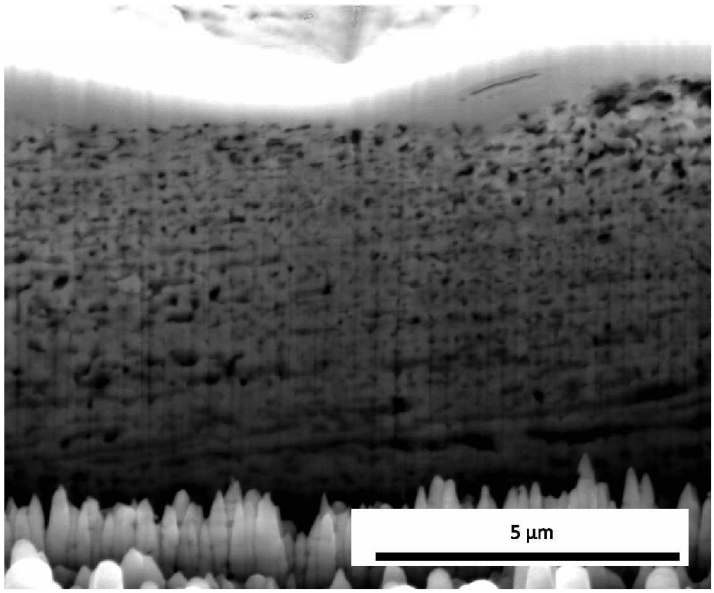

Figure 4.7: Dealloyed zone below an indent in order to check the dealloying depth and morphology. The bright area on the top surface of the indent is a protective Platinum layer.

4.2.1 Relative density measurements

The porosity of the foam is an essential criterion to know. Many assumptions and calculations can be justly used if the relative density of the porous material is known. In order to obtain this information, first the EDX and then the SEM imaging results are shown and explained. The yellow marked region in Figure 4.8 (a) shows the area which was used for the conducted EDX measurement. The measured area should cover a relatively wide range to get a good average result for the chemical composition of the foam. The EDX spectra of the examined area can be seen in Figure 4.8 (b). Two different elements can be distinguished, namely Cu and Fe. The foam approximately contains 97 wt.% Cu and 3 wt.% Fe. There are two assumptions of where the remaining Fe could be: Either still solidly supersaturated in the Cu phase, or during the dealloying process some of the Fe remained. In order double-check this, SEM images are analyzed to determine the porosity.

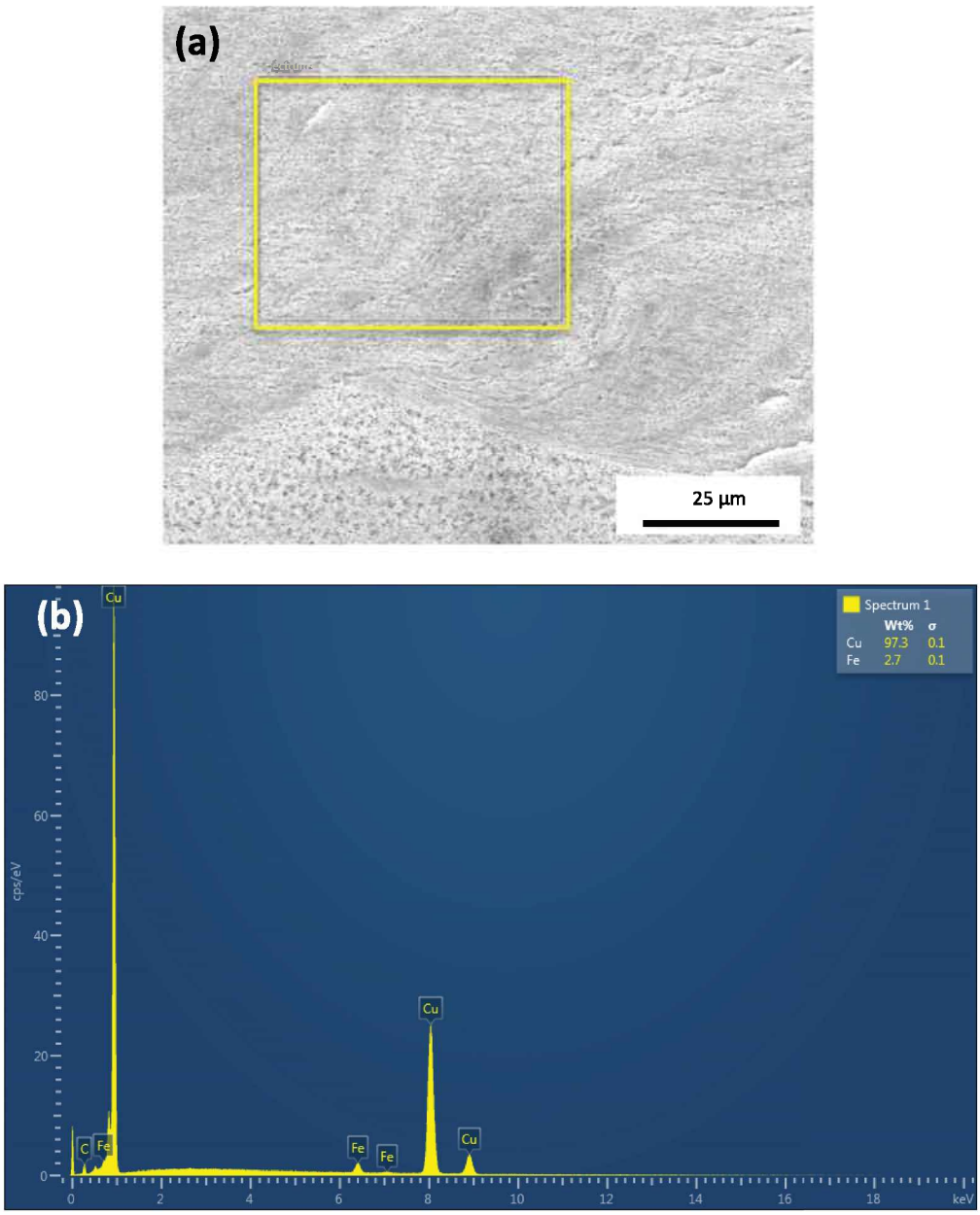

Figure 4.8: (a) SEM image of the polished and dealloyed surface in axial direction of the foam. The area inside the yellow rectangle shows the EDX examined area. (b) EDX-spectra of the polished surface and the chemical composition of the foam.

An example of a SEM processing sequence is shown in Figure 4.9 for an SEM plan view micrograph of the open cell NPC. The original micrograph is shown in Figure 4.9 (a). Figure 4.9 (b) shows the image processed to a grey scale image. Figure 4.9 (c) is the image processed with a bandpass filter and Figure 4.9 (d) shows the binarized image with pores and struts clearly distinguished. The relative area is identical to relative density for statistically isotropic structures of the whole specimen at a radius of 3 mm of the center. The information provided by the SEM micrographs using secondary electrons (SE) contains mainly information about features close to the focal plane since signal detection probability exponentially decays when electrons travel in the out-of-plane direction [29]. After processing sufficiently

focused images, the relative density averaged over a narrow region close to the surface can be obtained. If a sufficiently large amount of struts and pores are captured in the micrograph view, then the relative density of the micrograph is independent of the field of view. This was proven by processing images having three different magnifications, where the images of the two higher magnifications are shown in Figure 4.10. The average relative density for all magnifications was 53.5 % $\pm$ 1.5 %. This result also indicates the proposed assumption that around 3 wt.% of the Fe is still solidly supersaturated in the Cu phase.

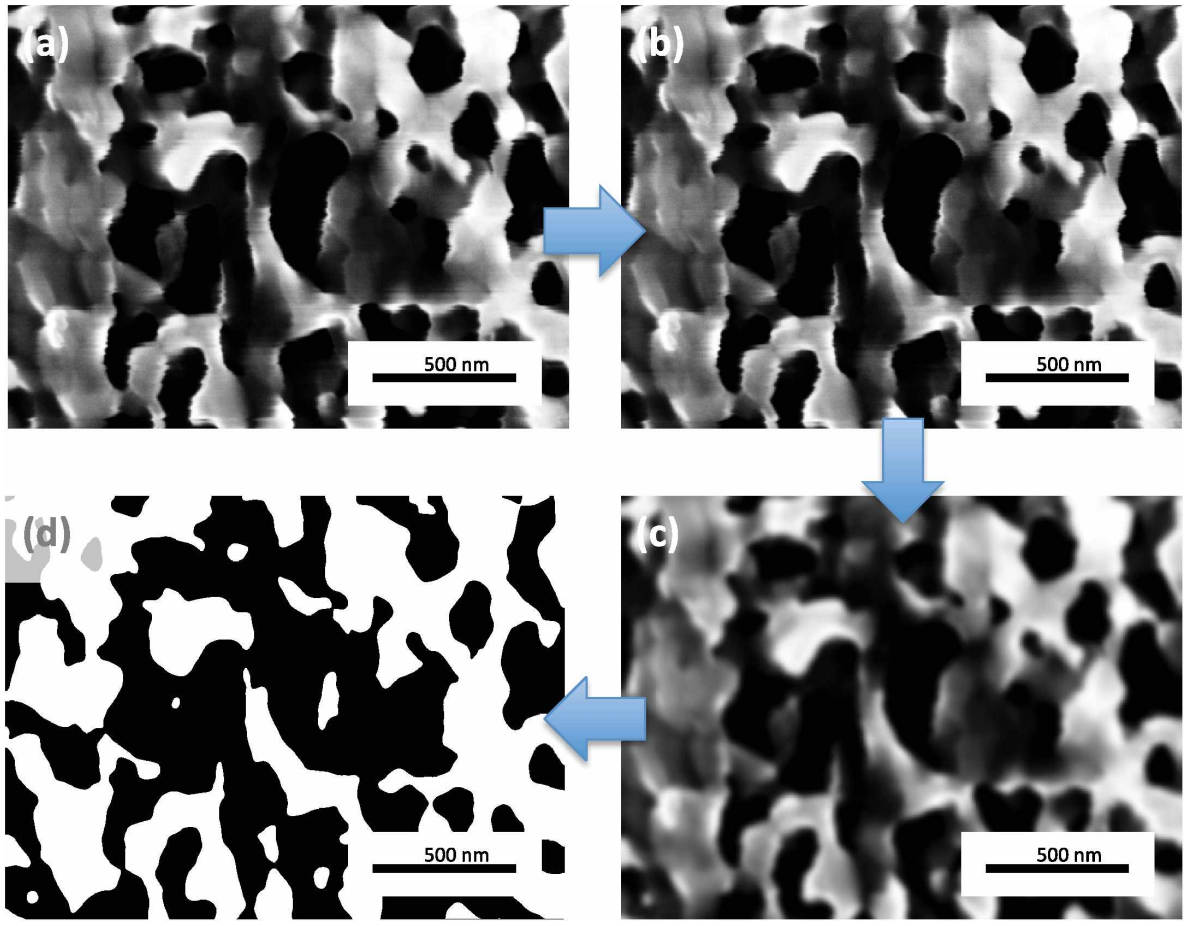

Figure 4.9: Image sequence showing how an SEM micrograph is converted to a binary image for relative density measurements: (a) Plan-view SEM micrograph of open cell NPC. (b) SEM image after converting into a grey scale image. (c) The image after using a bandpass filter. (d) The binary image after converting the filtered image.

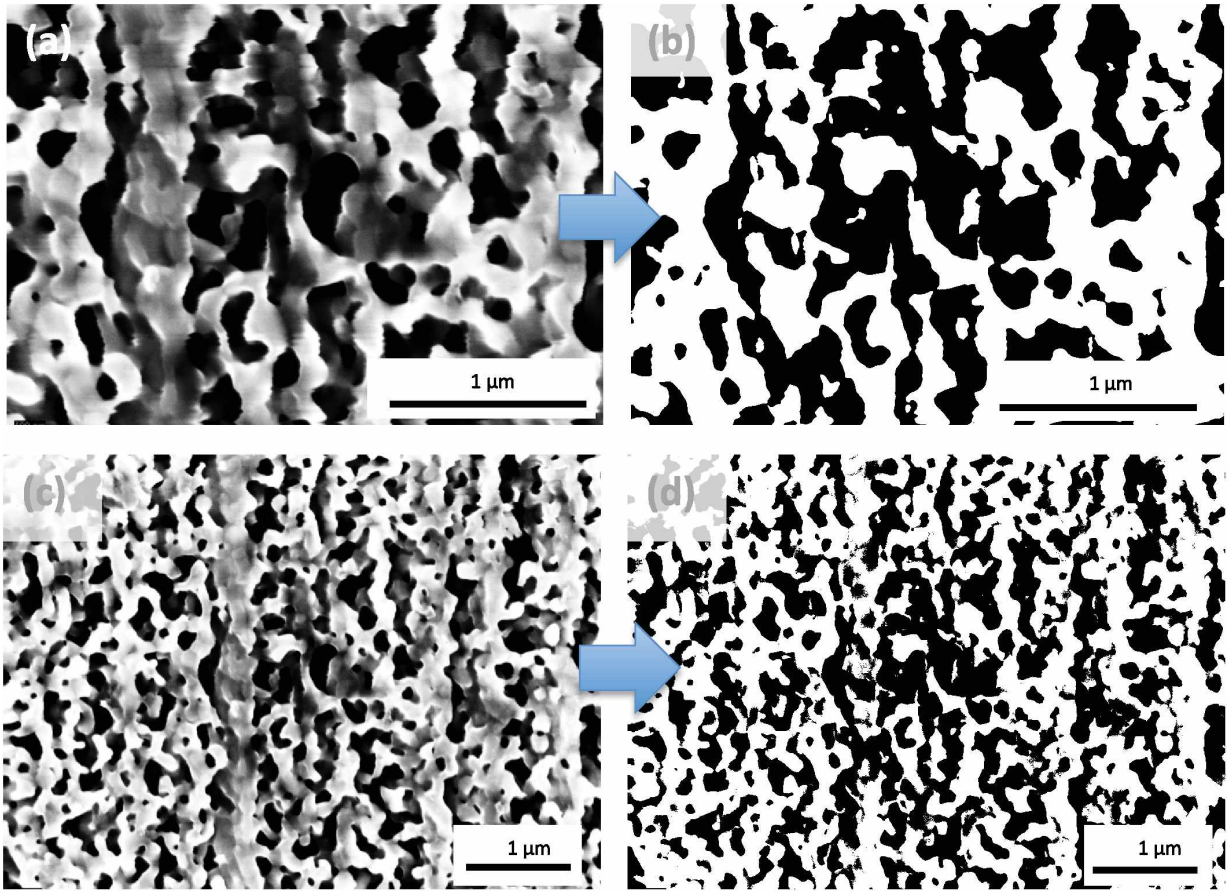

Figure 4.10: (a), (c) SEM images of the foam with two different magnifications. (b), (d) The corresponding binarized images.

4.3 Nanoindentation

In the present work, the mechanical properties of the NPC with a relative density of 53% are investigated by nanoindentation between room temperature and 300°C. The mechanical properties, such as hardness and elastic modulus, are measured and evaluated. Furthermore, the strain rate sensitivity and activation volume of the material are determined to reveal information about the material deformation mechanisms. The deformation of the NPC during nanoindentation is demonstrated by the load-displacement P-h indentation curves, displayed for different temperatures in Figure 4.11, where the left column shows DC experiments data, while CL data is provided in the right column, respectively. These experiments were performed on the polished surface of the sample to minimize the effect of surface roughness. The experiments do not probe the mechanical properties of individual ligaments, but an average mechanical response of a large number of ligaments and pores has been assessed. This is ensured by the high indentation depths, ranging from one up to three microns, resulting in large imprints probing a volume in the order of several cubic microns. Compared to this, the typical ligament width of 200 nm is significantly smaller. A certain var-

iation of the P-h curves can be observed, but this was expected considering the inherent inhomogeneity of a random porous material.

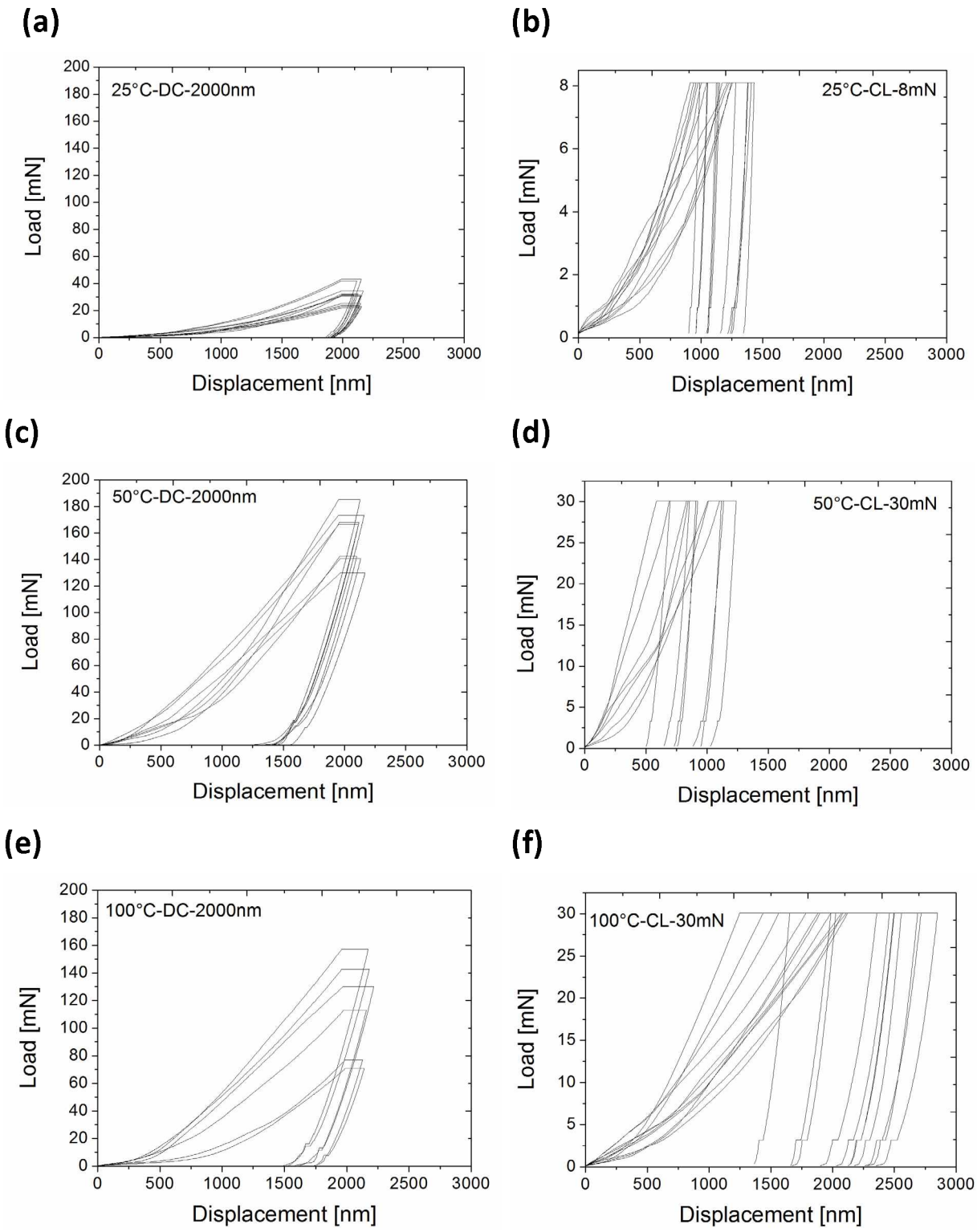

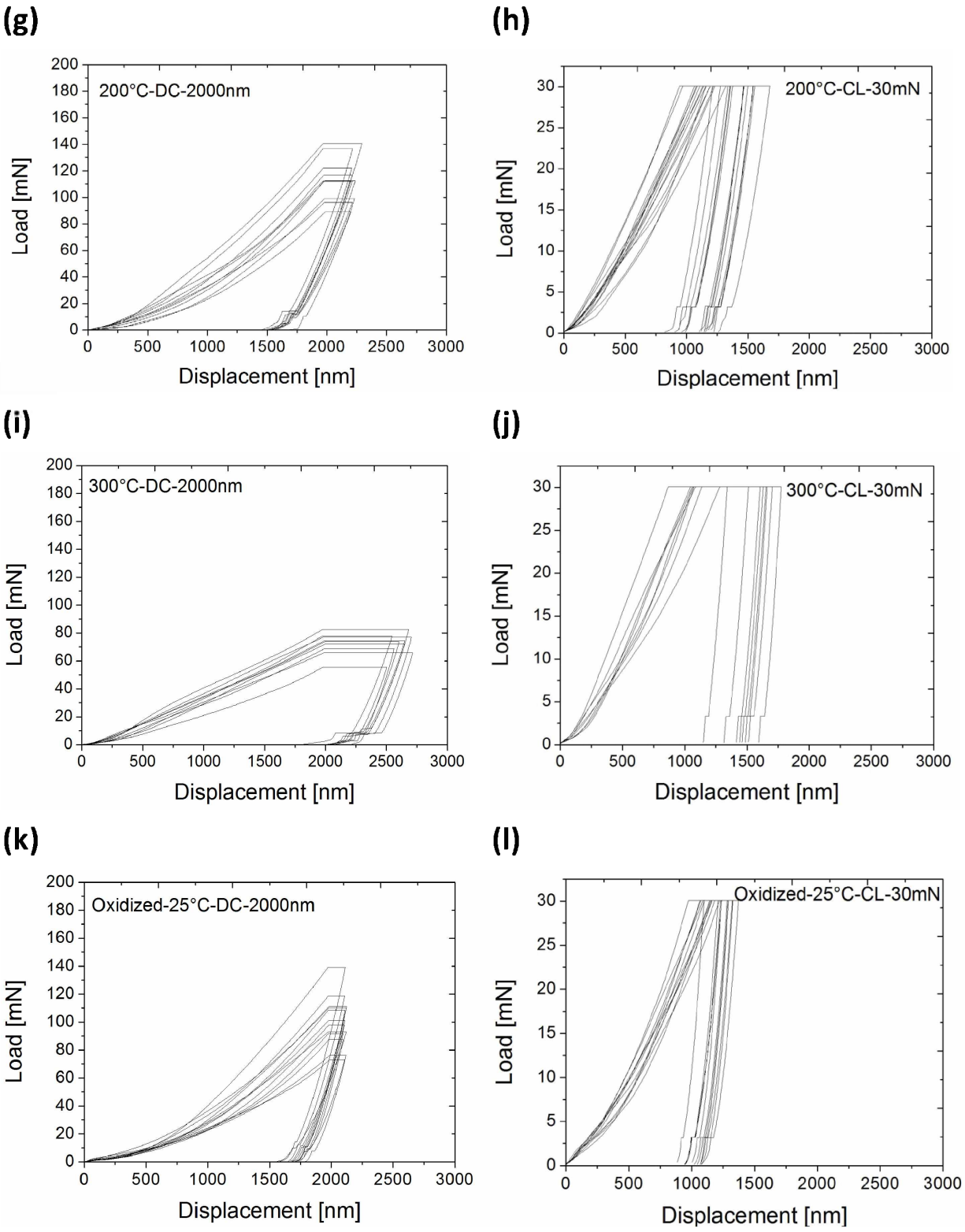

Figure 4.11: Load-Displacement curves for all temperatures and parameters. On the left side the depth-controlled (DC) measurements for (a) 25°C (c) 50°C (e) 100°C (f) 200°C (i) 300°C and (k) 25°C (After 100°C/15h and 200°C/15h) are shown, and on the right hand side the curves for (b) 25°C (d) 50°C (f) 100°C (h) 200°C (j) 300°C and (l) 25°C (After 100°C/15h and 200°C/15h) for constant load measurements (CL).

4.3.1 Young's modulus and hardness

This chapter provides information about the mechanical properties of the foam. To access the change of hardness and Young's modulus over temperature, DC measurements were performed with a constant strain rate. Figure 4.12 visualizes the correlation between Young's modulus, which was obtained from the reduced modulus by using equation (16), and temperature. The obtained values for 25°C in the non-oxidized state are symbolized by "Start". First, an increase of the Young's modulus from 17 $\pm$ 3.5 GPa to 26.8 $\pm$ 3 GPa was observed up to 100°C, which was followed by a decrease in modulus down to 22.2 $\pm$ 2.2 GPa at 200°C and 16.7 $\pm$ 2.1 GPa at 300°C, as expected from equation (6).

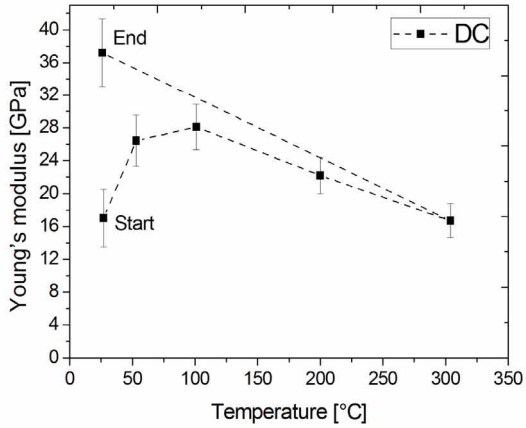

Figure 4.12: Young's modulus versus temperature for NPC up to 300°C. "End" symbolizes the RT modulus after high temperature experiments.

Figure 4.13 shows the change of hardness over temperature. A strong increase of the hardness from 220 $\pm$ 60 MPa up to $\sim$ 950 $\pm$ 300 MPa was observed at 50°C, which stayed constantly at 100°C and 200°C, contrary to the predicted decrease by equation (7) with increasing temperature. At 300°C a hardness drop from 940 $\pm$ 140 MPa down to 300 $\pm$ 60 MPa was observed.

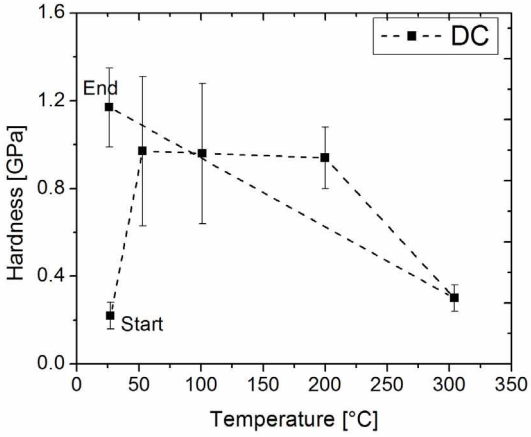

Figure 4.13: Hardness over temperature for NPC up to 300°C. "End" symbolizes the oxidized sample at RT.

The values of the RT hardness after the high temperature experiments at 25°C are shown in both graphs close to the symbol "End". The sample after high temperature indentation shows an enormous increase of around 500 % in hardness and 200 % in Young's modulus compared to the original 25°C experiments, which will be discussed later in chapter 5.2.1. The hardness and the Young's modulus values are tabled in Table 5.

Table 5: Overview of the mechanical properties of the NPC obtained from DC measurements.

Temperature [°C]	H [MPa]	E [GPa]
25	220 (±60)	17.0 (±3.5)
50	970 (±340)	26.8 (±3.0)
100	960 (±320)	28.1 (±2.8)
200	940 (±140)	22.2 (±2.2)
300	300 (±60)	16.7 (±2.1)
Oxidized 100°C/200°C -15h/15h	1170 (±180)	37.2 (±4.1)
Oxidized 300°C – 6h	1280 (±410)	32.8 (±5.1)
Oxidized 400°C – 5 h	1610 (±180)	26.2 (±1.8)

The obtained mechanical properties back at 25°C after the high temperature experiments are shown in Figure 4.14. The oxidized samples were measured after the high temperature nanoindentation experiments in order to get a better understanding of the change in material properties. Equation (24) and Table 2 were used to estimate the thickness of the oxide layer and the results of calculation are shown in the tick labels of the x-axis in Figure 4.14. The oxide types for the different temperature regimes were obtained from the model shown in Figure 2.11 and from XRD ex-situ and in-situ measurements. A pronounced difference in hardness and Young's modulus between non-oxidized and oxidized samples is observed (Figure 4.14).

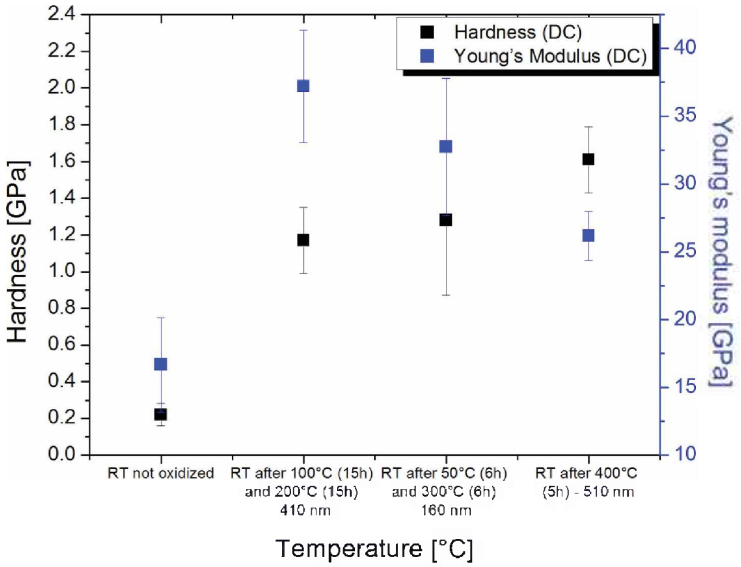

Figure 4.14: Mechanical properties for different oxidized samples. The dwell time at a certain temperature and the estimated thickness of the oxide are indicated in the x-labels.

4.3.2 Strain rate sensitivity and activation volume

The results of the nanoindentation stress relaxation tests are presented in this chapter. The aim of these experiments was to obtain material parameters characteristic for strain rate- and temperature dependent deformation mechanisms. An example of a double logarithmic plot for determination of the *m* value is shown in Figure 4.15. The slope of the two distinct regimes corresponding to Stage *a* and *b is* similar, namely between 0.03 and 0.04. The *m* value was calculated by using equation (19), which is given by the slope of the curve in Figure 4.15.

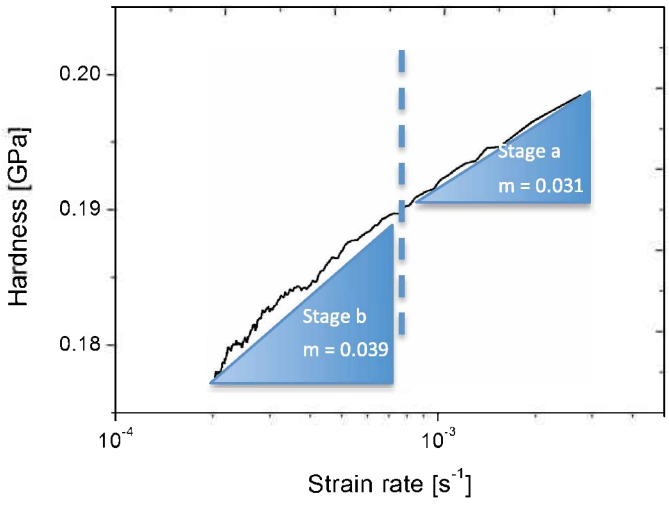

Figure 4.15: Double logarithmic plot of hardness versus strain rate. Similar *m* values for Stage *a* and *b* are observed.

Figure 4.16 shows the *m* value versus temperature for CL and DC measurements. In general, an increase of the strain rate sensitivity over temperature from 0.03-0.04 to 0.1-0.2 was observed for all different experimental conditions. For Stage *a* and Stage *b* of the CL experiments the same trend of the *m* value was observed. The *m* value for 100°C DC measurements slightly differs compared to that of the CL measurements. The effect of the oxidation and temperature on the *m* value will be discussed later in chapter 5.2.3.

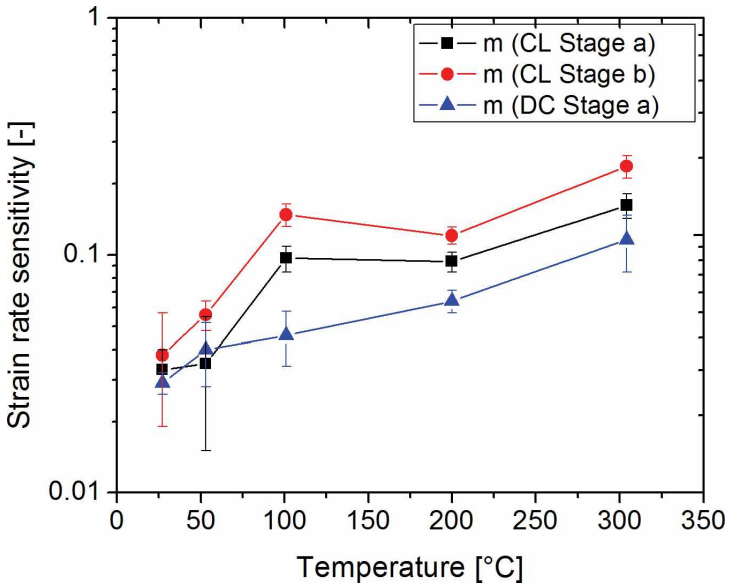

Figure 4.16: Strain rate sensitivity over temperature for CL and DC measurements.

The results of the investigation of the RT experiments after high temperature indentation are shown in Figure 4.17. No significant changes of the *m* value between the measurements before and after the oxidation were observed for the DC measurements, which show a very constant value of 0.03 for all different conditions. The Stage *a* *m* values of the LC measurements are around 0.04 and show higher scattering than the DC measurements. The Stage *b* results of LC measurements are between 0.04-0.06 and show significantly higher standard deviations. The reason for the high standard deviation is the roughness of the surface due to heavy oxidation. The *m* values for all temperatures are summarized at the end of this chapter in Table 6.

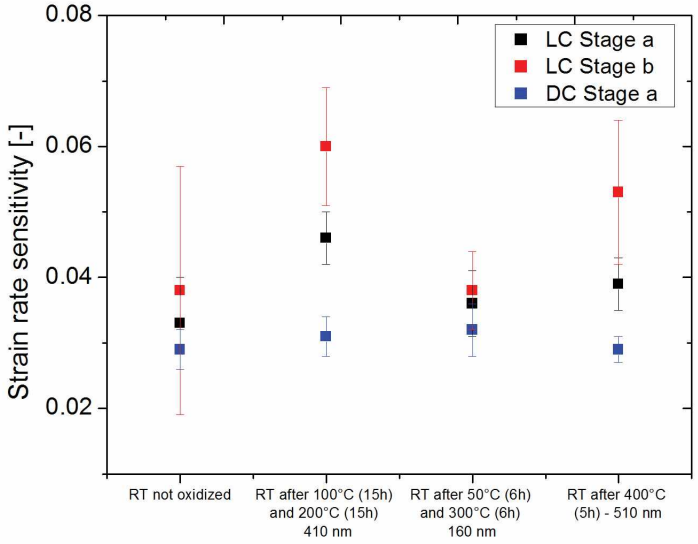

Figure 4.17: Strain rate sensitivity for a non-oxidized and different oxidized samples at RT. The tick labels on the x-axis symbolize the length of the heating segment and the estimated thickness of the oxide layer.

The activation volume versus temperature is plotted in Figure 4.18. The activation volume was normalized using the volume of a cubic Burgers vector for Cu (Dislocation: 1/2·{110}, b = 0.255 nm [68]). An upper and lower boundary calculation of the activation volume using equation (20) was performed. The upper boundary is indicated by $H \sim 3 \cdot \sigma_f$ (behavior of low density foams), and the lower boundary by $H \sim \sigma_f$, as explained in chapters 2.2.3 and 2.3.3. This assumption was taken into account to account the densification of the foam during oxidizing and the correlation for ceramics between yield strength and hardness of $H \sim 1.5 \cdot \sigma_f$. The minimal activation volume versus temperature is plotted in Figure 4.18 (a) and the maximal in Figure 4.18 (b). Hereby, a similar trend for Stage *a* and Stage *b* was observed. The activation volume strongly decreases from approximately 250-850 b^3 at RT to 20-150 b^3 at 50°C, 100°C, 200°C and 300°C, respectively. Thus, *A* remains rather constant at elevated temperatures. The activation volume for the oxidized sample is about 10-15 times lower (10-100 b^3) than that of the non-oxidized material.

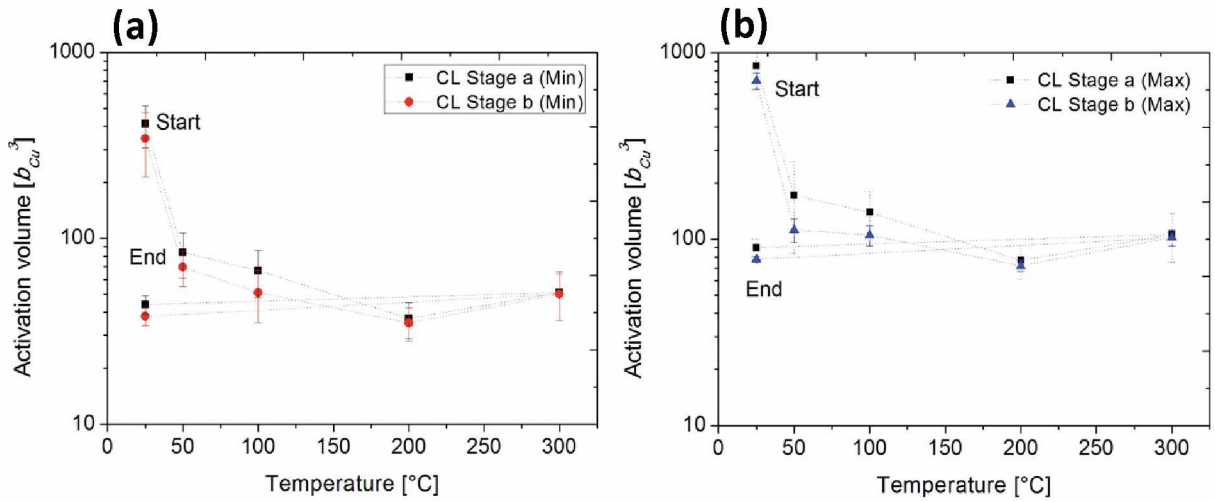

Figure 4.18: (a) Normalized *A* over temperature for CL measurements with the assumption: $H \sim \sigma_f$. (b) Normalized *A* over temperature for CL measurements with the assumption: $H \sim 3 \cdot \sigma_f$.

The activation volume was also obtained from the dwell segment (only Stage *a*) of DC measurements and is plotted in Figure 4.19 (a). Again, the lower and the upper boundary of the relative activation volumes are displayed, and generally the same trend and activation volumes as for CL-tests (Stage *a*) were observed as shown for comparison in Figure 4.19 (b) for the upper boundary.

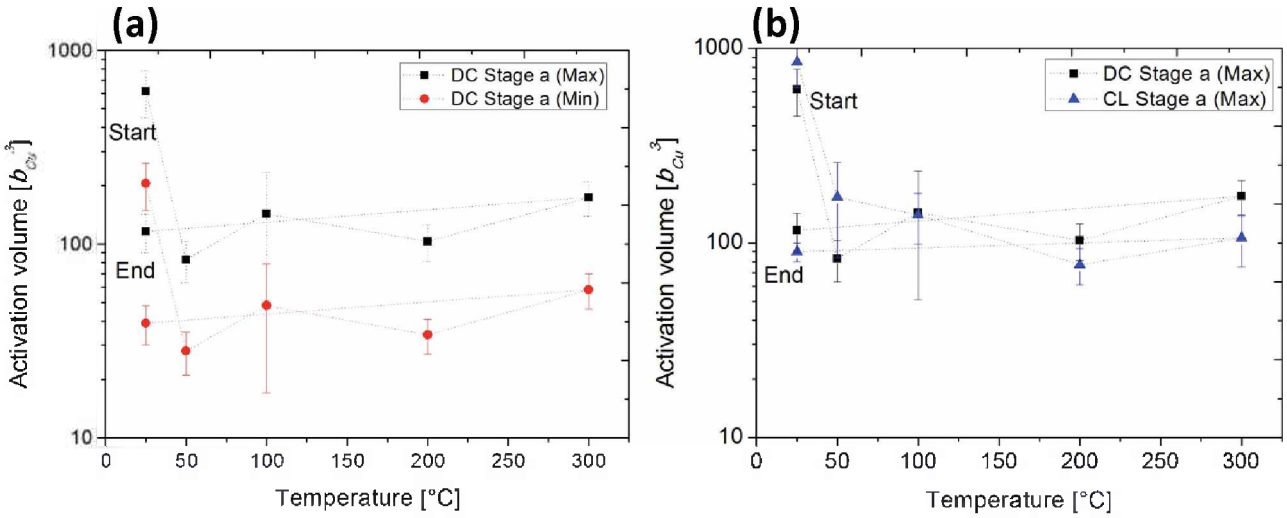

Figure 4.19: (a) Relative *A* obtained from DC measurements. The minimal and maximal normalized *A* are plotted. (b) *A* versus temperature plot comparing DC and CL Stage *a* results.

Finally, the obtained activation volumes for different oxidized samples at RT after high temperature testing are shown in Figure 4.20. No significant differences were observed for different oxidation temperatures and times as shown in the labels on the x-axis. A certain tendency of a lower activation volume for the 400°C after-heating experiments is given, but overall the activation volume of the oxidized samples is between 20 b^3 and 150 b^3, and remains relatively constant for all different heating conditions.

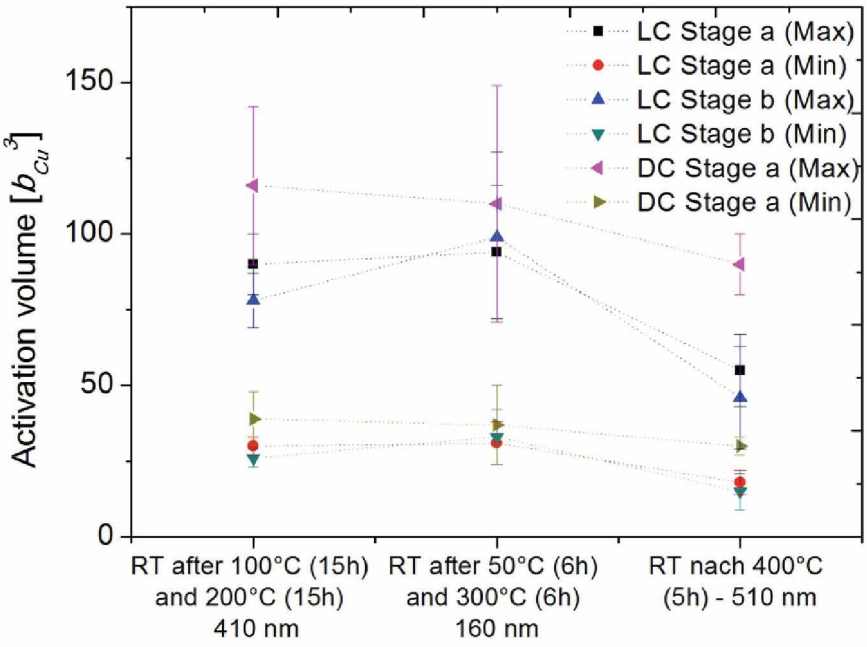

Figure 4.20: Relative activation volume for different oxidized dealloyed specimen at 25°C. The tick labels on the x-axis symbolize the length of the heating segment and the estimated thickness of the oxide layer.

For summary, Table 6 shows all activation volume and strain rate sensitivity values for different temperatures and stages. Furthermore, the RT measurements of different oxidized samples are shown.

Table 6: Average *m* and *A* values for different experimental conditions.

Temperature/ Testing conditions	*m* LC (Stage a)	*m* LC (Stage b)	*m* DC (Stage a)	*A* CL (Stage a) [b^3]	*A* CL (Stage b) [b^3]	*A* DC (Stage a) [b^3]
25°C	0.033	0.038	0.029	283-848	236-708	205-616
50°C	0.035	0.056	0.046	57-172	48-112	28-83
100°C	0.097	0.148	0.046	46-139	35-105	48-143
200°C	0.094	0.121	0.064	26-77	24-72	34-103
300°C	0.162	0.237	0.116	35-106	34-102	58-174
Oxidized 100°C – 15 h 200°C – 15 h	0.046	0.060	0.031	30-90	26-78	39-116
Oxidized 300°C – 6 h	0.036	0.038	0.032	31-94	33-99	37-110
Oxidized 400°C – 5 h	0.039	0.053	0.029	18-55	15-46	30-90

4.3.3 SEM and FIB investigations

Indents, which were placed in very heterogeneous areas, were discarded for 25°C experiments by analyzing SEM images, as shown in Figure 4.21. Areas with irregularities nearby (circled in Figure 4.21) could be clearly correlated to low apparent modulus of the nearby indent. The SEM approach was not possible for high temperature experiments due to the oxidization of the sample surface making the indents disappear over time. Therefore, based on the insights from the RT investigation for RT and high temperature experiments a threshold of 10 GPa for the Young's modulus, which is very sensitive to inhomogeneities, was defined as a criterion in order to discard adulterated values.

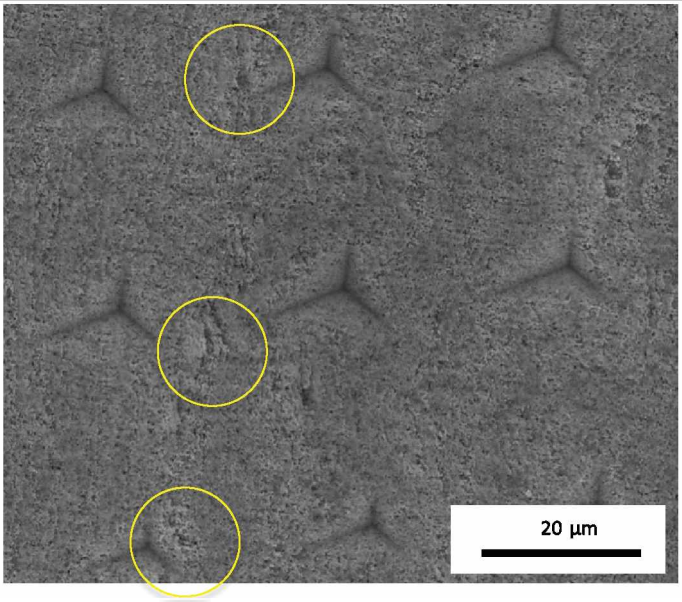

Figure 4.21: Overview of CL indents at 25°C. Circled areas show measurement-influencing areas.

The dominant deformation mechanism during nanoindentation in the NPC was expected as ductile, plastic densification. In order to prove this assumption, the residual imprints were studied using SEM to analyze the deformation of the NPC. Figure 4.22 shows SEM micrographs of 2000 nm depth-controlled imprints on the polished surface using a Berkovich tip after RT experiments. A confined deformation can be observed in the contact area, which is dominated by ductile densification of the foam. The pore structure is undisturbed adjacent to the indents. This demonstrates the absence of pronounced long-range stress fields and confirms the assumption H ~ σ_f, as described in chapter 2.2.3 and 2.3.2. During the indentation process at RT no ligament cracking was observed, which was proofed by detailed inspection of Figure 4.22 (c).

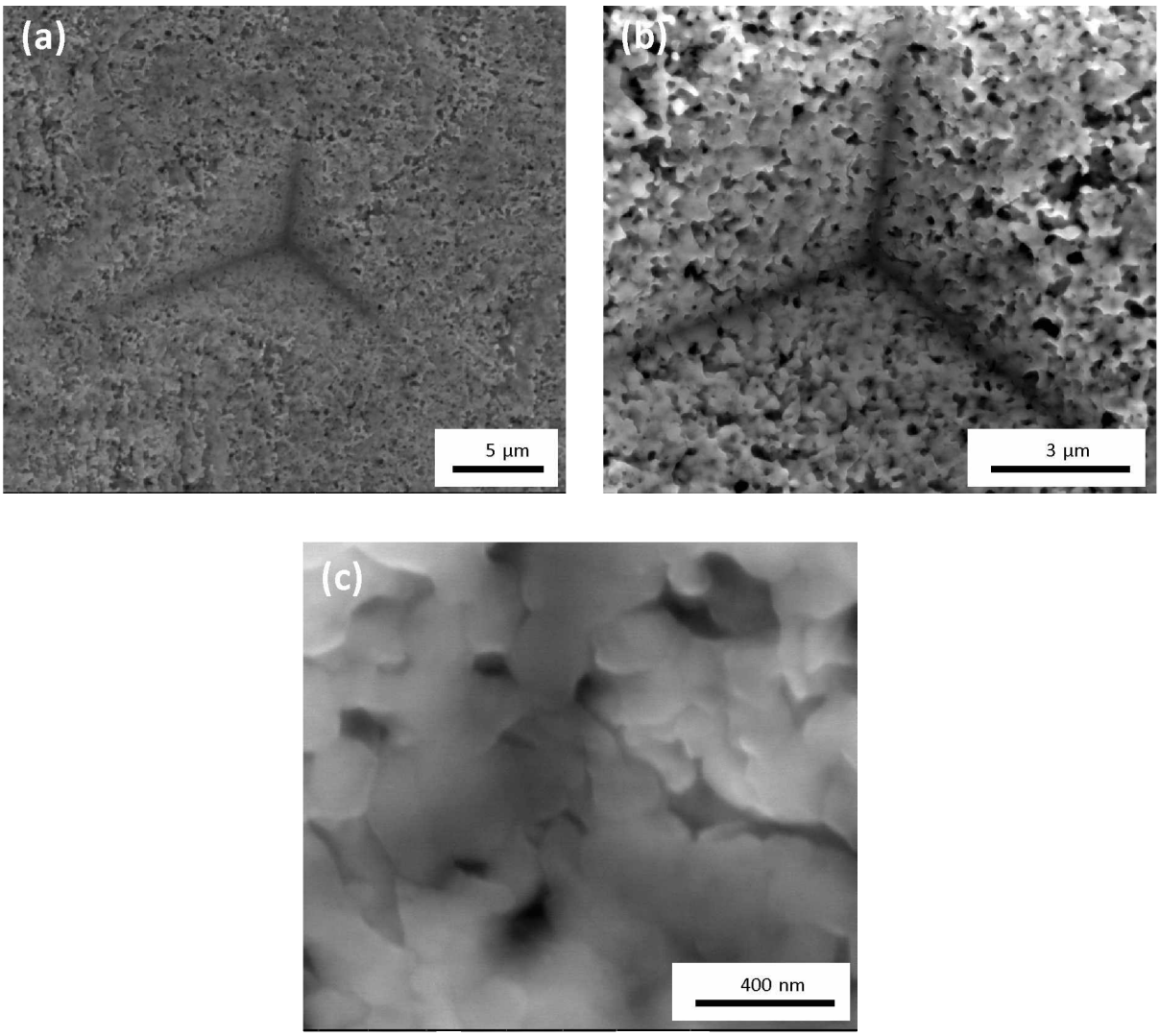

Figure 4.22: SEM micrographs of (a) an overview of an indent (b) more detailed image of the indent and (c) the deformed ligaments in the center of the indent.

Additionally, SEM images of the cross-section of an indent are shown in Figure 4.23. Figure 4.23 (a) shows the approach for making a local cross-section of an indent. Prior to the FIB milling process, Platinum was locally deposited via sputtering diagonal on the top of the indent in order to protect the surface and prevent curtaining of the cross-section surface. The SEM images Figure 4.23 (b) and (c) reveal that the deformation is contained in the contact area, and no pileup adjacent to the residual impression was observed.

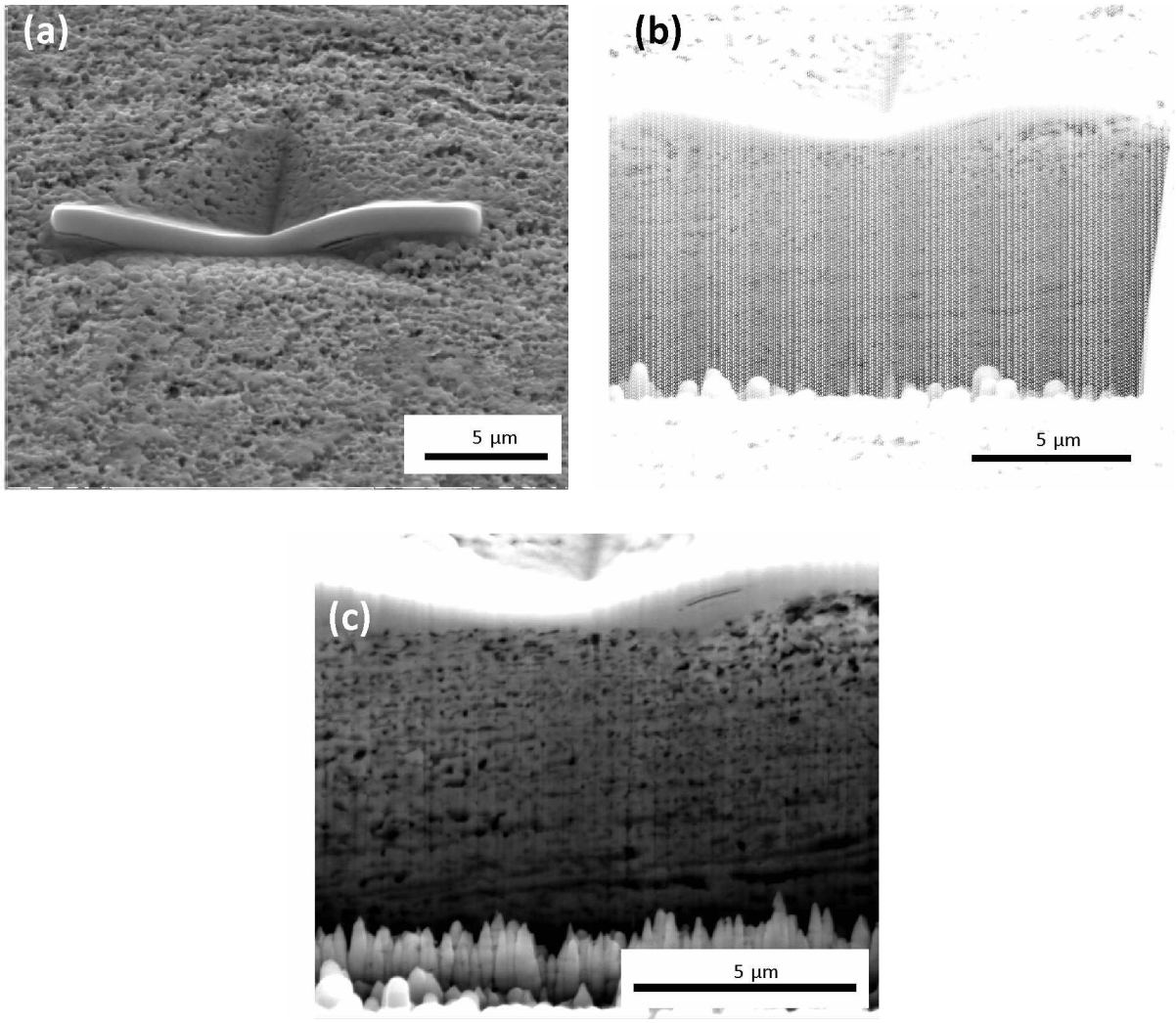

Figure 4.23: (a) Inclined SEM image of an indent sputtered with platinum to prevent curtaining. (b) Micrograph of a local cross-section beneath an indent and (c) more detailed micrograph of the local cross-section.

Investigation of the oxidation of the NPC

In order to understand the rapid increase of hardness and the Young's modulus over temperature, the specimen surface and local cross-sections were investigated by EDX after the high temperature nanoindentation experiments. The result of the EDX surface-scan after the measurements at 100°C and 200°C is shown in Figure 4.24. An increase of the oxygen content was detected close to the surface compared to the inner NPC. This result confirms that oxidation has occurred during heating. Especially the volume close to the surface was affected by the oxidation as shown by local cross-section and EDX line-scans in Figure 4.25, where the top 1.5 µm show increasing oxygen content.

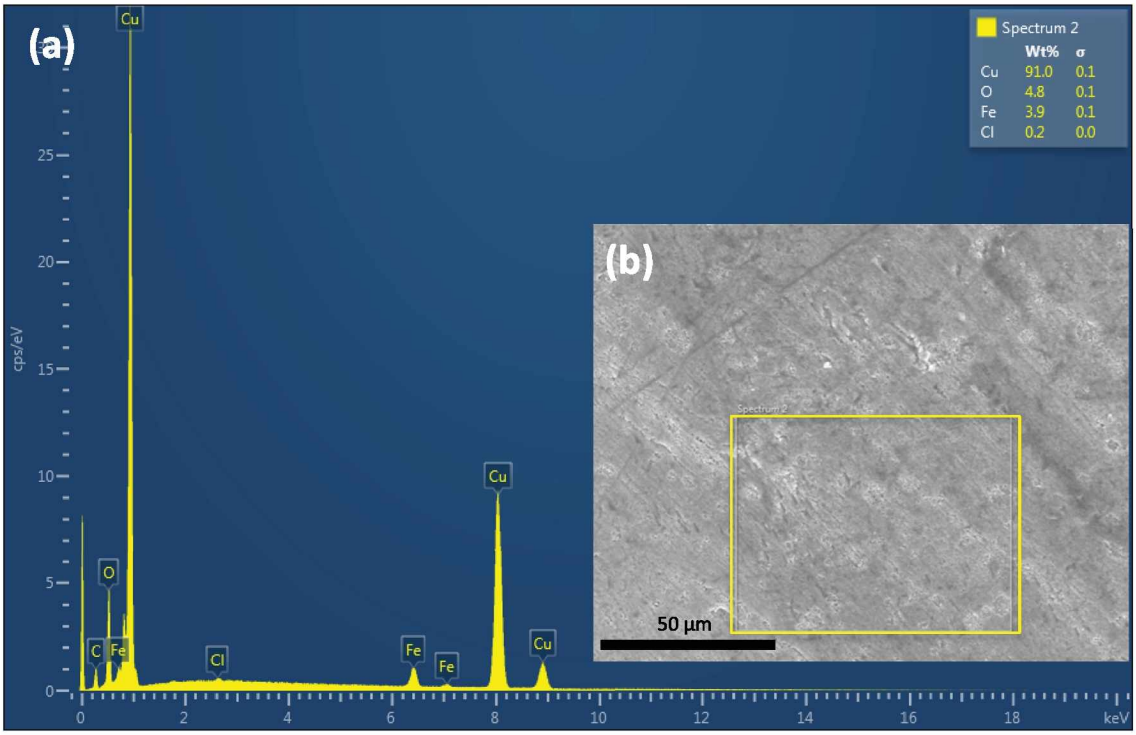

Figure 4.24: (a) EDX-spectra of the surface after high temperature nanoindentation. (b) Overview of the measured area.

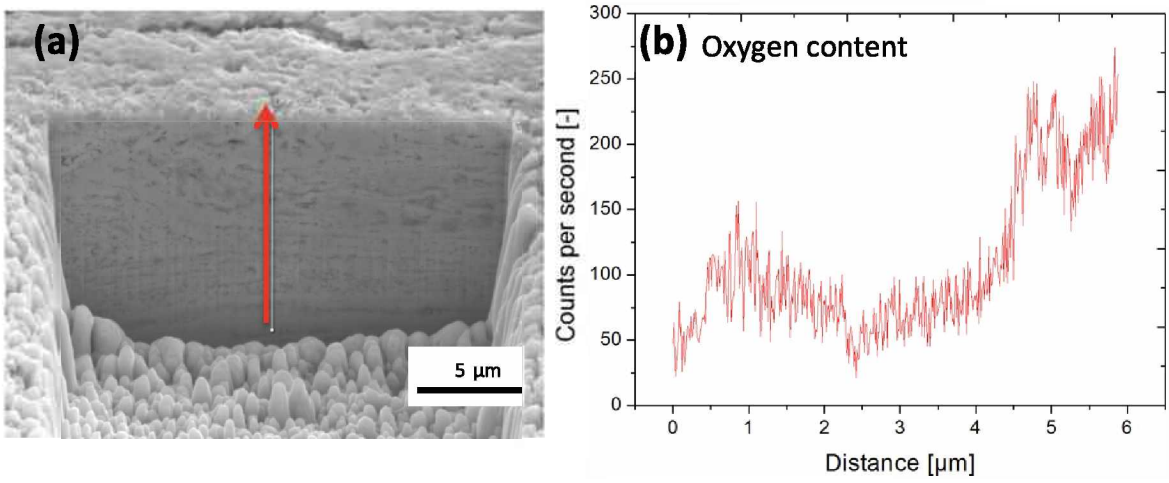

Figure 4.25: (a) Local cross-section of the surface after oxidation. (b) EDX line-scan close to the surface, which is indicated by the red arrow in image (a).

Figure 4.26 (a) and (b) show micrographs of the oxidized sample surface after six hours at 100°C and 200°C, respectively. A densification up to ~95% relative density during the oxidation process was observed due to conversion of copper into copper oxide, which was proofed by analyzing the SEM image (Figure 4.26 (a)) with the explained method in chapter 4.2.1. Furthermore, a strong increase of the surface roughness was detected. An indent after high temperature measurements at 100°C is shown in Figure 4.26 (c). Crack propagation around the indent was not observed. Note that possible small cracks could not be detected due to the oxidation process during high temperature testing. The local cross-section of an indent after high temperature testing revealed a rather dense oxide layer on the top of the NPC, as shown in Figure 4.26 (d). The thickness of this oxide layer is in the order of 1-2 µm, even after low temperature oxidation of the NPC at 100°C for six hours and 200°C for six hours.

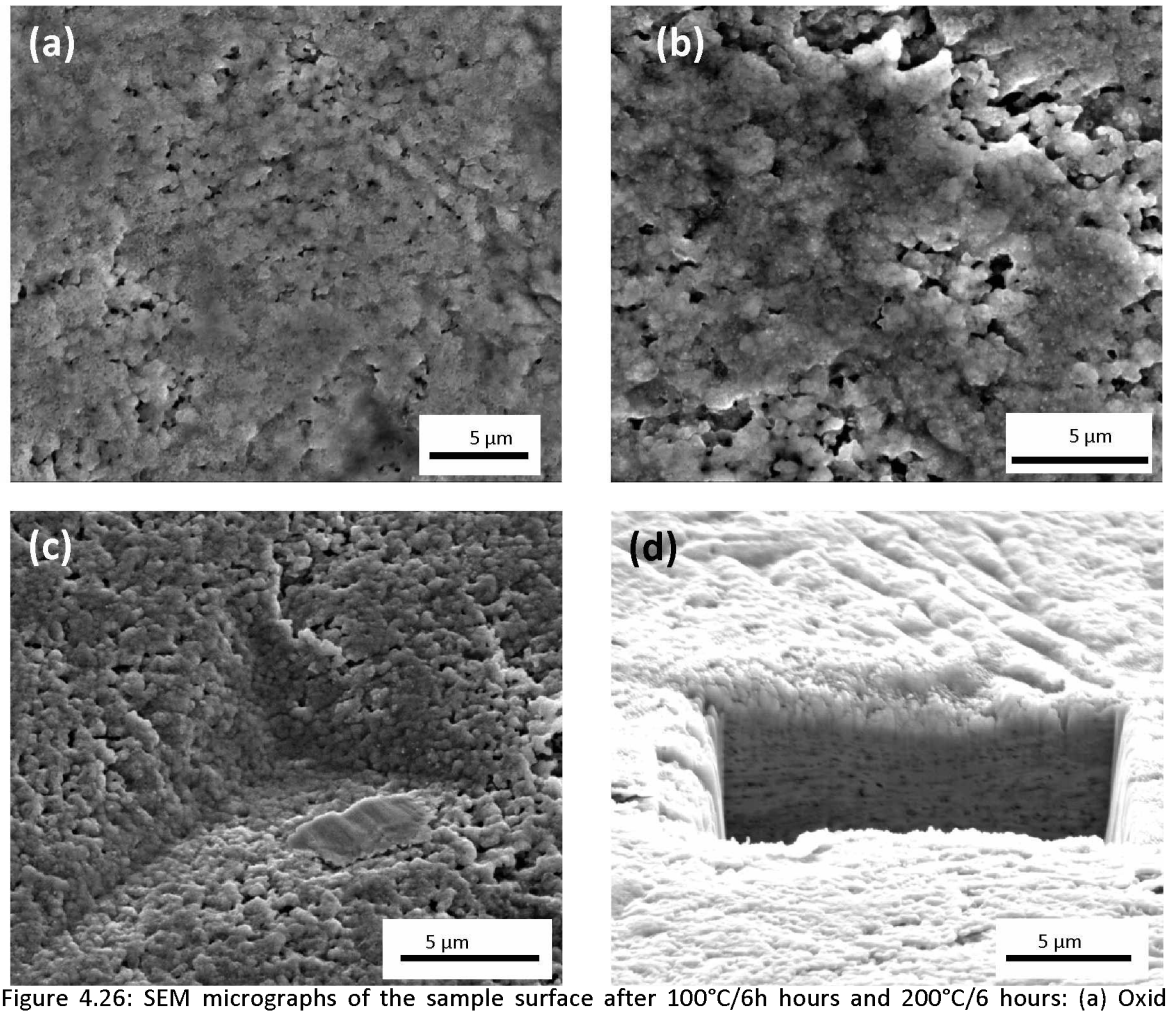

Figure 4.26: SEM micrographs of the sample surface after 100°C/6h hours and 200°C/6 hours: (a) Oxidized sample surface. (b) Detailed micrograph of the oxidized surface. (c) Overview of an indent after 100°C/6h hours and 200°C/6 hours. (d) Local cross-section of an indent showing a rather dense oxide layer.

The XRD-measurements revealed a detectable oxidation at a temperature of 150°C, as shown in Figure 4.27 (a) and (b). The differentiating between CuO and Cu_2O is quite difficult due to similar positions of the peaks, as shown in Figure 4.27 (b). The XRD-spectrums of a non-oxidized sample and an oxidized sample at 300°C for six hours are overlaid in Figure 4.28. Mainly the formation of Cu_2O was observed, but also low intensity peaks of CuO were detected. Moreover, a diminishing of the Cu (111) peak and a slight move to lower diffraction angles were observed. The Fe (110) peak belongs to small amounts of not dissolved crystalline Fe, which is encapsulated by Cu and not reachable for the HCl.

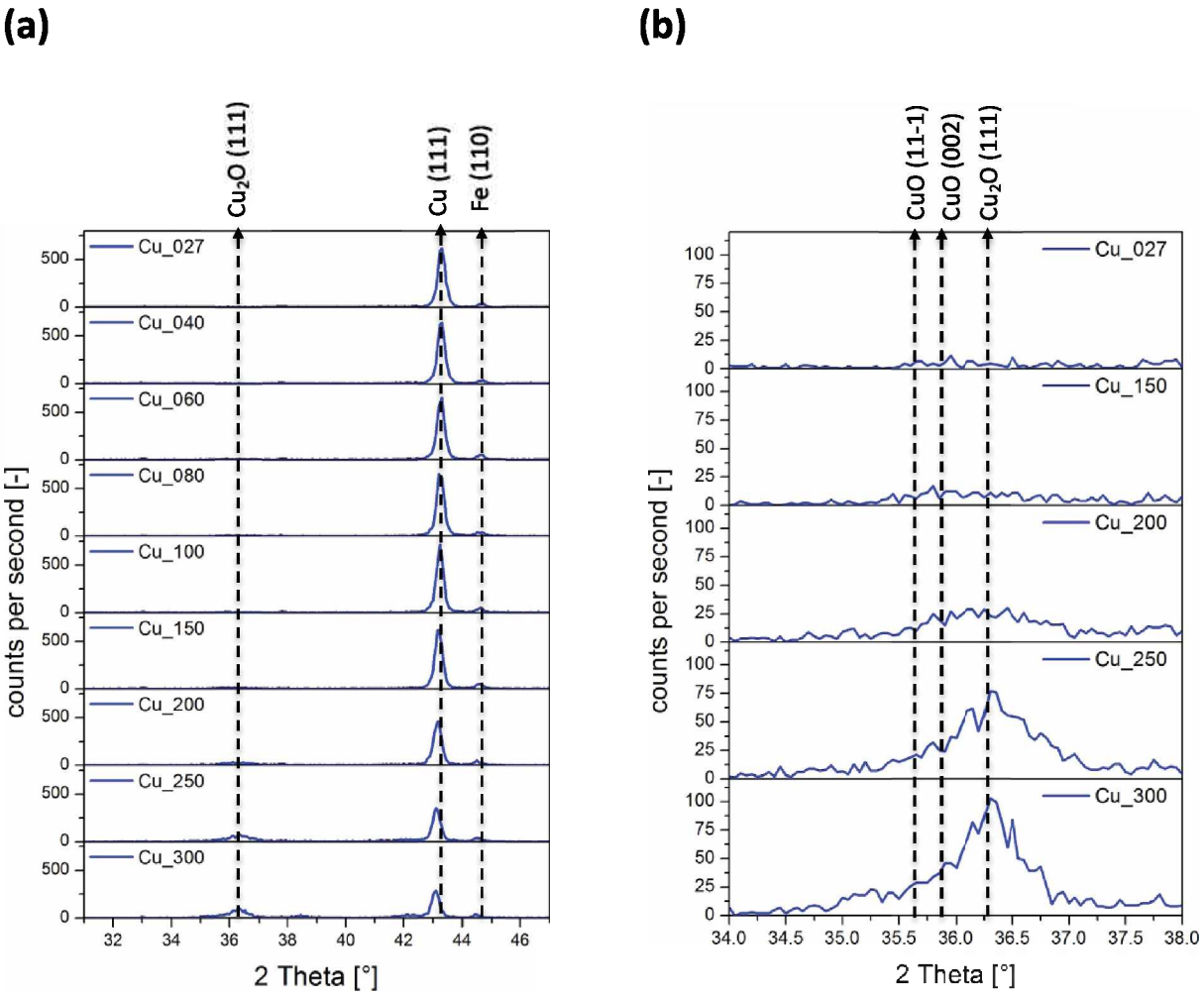

Figure 4.27: (a) XRD-spectrums for different temperatures of the oxidizing sample. (b) Detailed view of the growing Cu_2O peak for relevant temperatures.

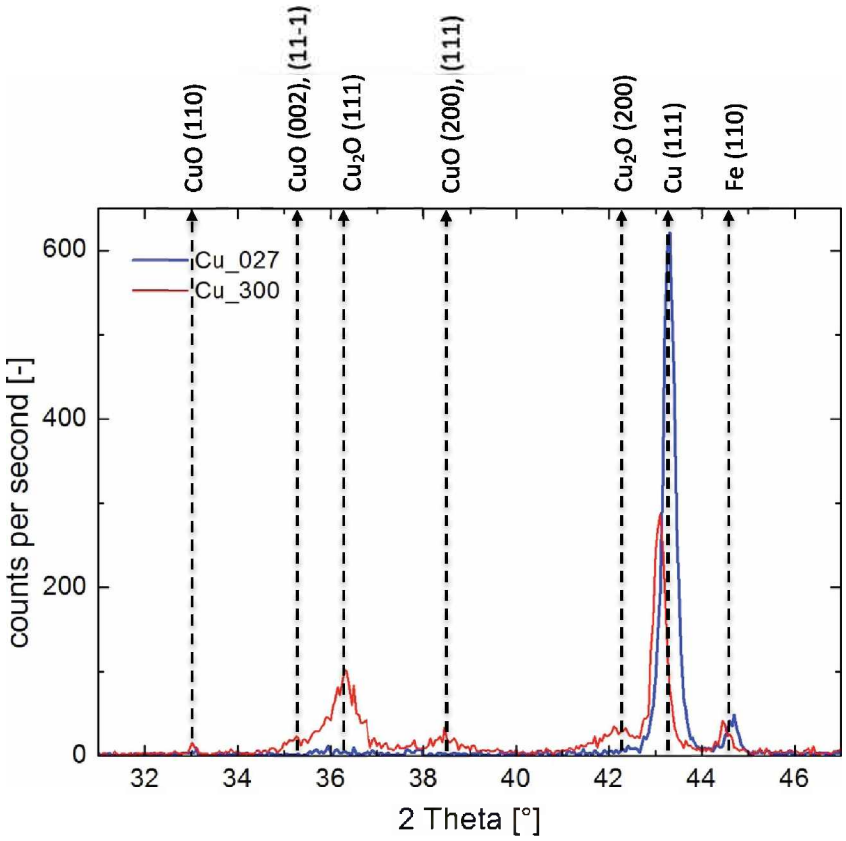

Figure 4.28: Red line: XRD-spectrum after the oxidization at 300°C for 6 hours. Blue line: XRD-spectrum of a non-oxidized sample.

5 Discussion

5.1 Sample fabrication

In the present work, a mixture of UFG supersaturated FCC Cu and BCC Fe is obtained after the two-step HPT process, where the formation of supersaturated solid solutions occurs as a result of the severe plastic deformation. The microstructure of the finally obtained NPC showed slight inhomogeneities after the manufacturing process as shown in Figure 4.4, Figure 4.7 and Figure 4.24 (c), although the novel two-step HPT route (proposed by Bachmaier et al. [4]) was used up to the saturation regime for the production of the primary material. One possible solution for this inconvenience would be an increase of the used HPT steps in order to reduce the grain size homogenously in all directions. For further decrease of the grain size by HPT, lower temperatures would be required during deformation as shown in Bachmaier's work [4], but this would possibly limit the high temperature stability. In general, this novel method is a good and effective way to obtain nanocomposites.

The heat treatment after the HPT deformation is essential for a further dealloying process. The annealing at a temperature of 500°C for 1 hour is used in order to stay in balance between achieving the desired decomposition and retaining the UFG microstructure. Finally, several percent of the supersaturated Fe in the Cu phase are still present after selective dissolution, as shown by the EDX surface-scan in Figure 4.8. One possibility to reduce the remaining Fe would be changing the time and temperature of the heat treatment. This, however, requires many processing steps and was not carried out in this thesis.

The selective dissolution process is an easy method to obtain nanoporous structures with different ligament shapes and sizes, as presented in this work. A minimal change of the process temperature or concentration of the acid would lead to different nanoporous structures [20,21]. For the CuFe-system just a low concentration of HCl is required to reach the wanted nanoporous material. The increase of the temperature to 55°C accelerates the process, but also influences the ligament shape. Exceedingly higher temperatures and long etching times would also lead to an unwanted dissolution of the Cu phase. To sum up, the difficulty is to find

the balance of the right etching time and temperature for the desired ligament morphology. However, for the CuFe system selective dissolution is a simple and efficient method to obtain nanoporous structures.

5.2 Nanoindentation

5.2.1 Young's modulus and hardness

The hardness values of CuO and Cu_2O are between 2050–2490 MPa and 2010–2030 MPa [59], respectively, while the yield strength value of UFG Cu (grainsize around 200 nm) is around 450 MPa [42,69]. This corresponds to a hardness for UFG Cu of 1350 MPa ($H = 3\sigma_f$). Thus, the difference in hardness between copper and copper-oxide is significant. The increase of Young's modulus cannot only be explained by the values of CuO and Cu_2O, which are 80 GPa and 30 GPa [60,62], respectively, because during the oxidation of Cu to copper oxide (mainly Cu_2O), the relative density of the foam increases due to increase in volume. This is because of the uptake of oxygen from of the atmosphere. The volume of the foam would increase by 40–45% if the copper completely converts to copper oxide. Thus, the relative density would be ~95% up to nearly 100%. The increase of relative density close to the surface can be seen in Figure 4.26 (a) and (b) after annealing at 100°C for 6 hours and 200°C for 6 hours, respectively. Identification of the porosity has become almost impossible in this state. Furthermore, the roughness of the surface has increased dramatically, resulting in a relatively high standard deviation of hardness and Young's modulus values. This is related to an inhomogeneous oxidation process of the surface, as shown in Figure 4.26. The local cross-section of an indent in Figure 4.26 (d) shows that the first one or two micrometers of the surface are completely oxidized and seemingly dense. The zone below the oxidized layer is not much affected by the oxidation. Therefore, changes in the measured foam hardness values allow estimating the ratio of copper-oxide and copper-foam. A model was developed in the present work to estimate hardness and Young's modulus, which is explained later.

Comparison to Gibson and Ashby equations

The flow stress of the foam can be compared to the values predicted by scaling laws, which are explained in chapter 2.2.2. The flow stress of the NPC was assessed from the hardness values obtained by the indentation experiments (for low density foams: $H = \sigma_f^*$). A more detailed discussion of the validity of this assumption can be found in chapter 2.2.3. According to this relationship, the flow stress of the NPC investigated in the present study is 220 MPa at 25°C. The yield strength for bulk copper with an average grain size of 200 nm is 450 MPa [42,69]. Note that the flow stress is obtained from the hardness of nanoindentation tests, and the yield stress of the scaling law equations. Nevertheless, the flow stress and the yield stress

can be compared for a good estimation, since for these high strength NPC materials the work hardening is not very pronounced. The yield strength for the porous material was estimated by using the scaling equation (4) and was compared to the measured flow stress ($H = \sigma_f^*$). The experimentally determined value of the yield stress and the flow stress is nearly five times larger than the value predicted by scaling laws, 220 MPa instead of 52 MPa. This deviation gives rise to the question whether the scaling laws deduced from macroscopic foams can still be applied to nanoporous materials. Further possible explanations for this difference are:

- There is still supersaturated Fe in the Cu ligaments
- The Gibson and Ashby equation is rather valid for homogenous foam structures and lower relative densities
- The theory of the near zero Poisson's ratio is not completely valid for the NPC
- The used yield strength for bulk Cu with 200 nm grain size is just an estimation

But if we assume that equation (4) describes the mechanical properties of the NPC, the experimentally determined value of 220 MPa for the yield strength of the NPC would require that the yield strength of the foam ligaments be in the order of 1.9 GPa. This interpretation suggests that the yield strength of the ligaments in the NPC would approach the theoretical strength of Cu (> 6 GPa [70]). Similar high values were also achieved for NC Au foams by Biener et al. [28].

The Young's modulus of the NPC is 17 GPa at 25°C. Assuming that the NPC sample exhibits a relative density of 53 % and using equation (5) for Cu, E = 100 – 130 GPa, the scaling law would predict a Young's modulus of 28-36 GPa. The difference of 10-20 GPa can be explained by the layered-structure of the NPC from the HPT shear deformation process, which is shown in Figure 4.7. The ligaments in the direction of indentation do not exist in the same density like the ligaments perpendicular to them, what is related to the inhomogeneity of the deformation process. The outcome of this is a lower Young's modulus in loading direction.

5.2.2 Oxidation of the NPC

During the high temperature measurements oxidation occurred despite the Ar atmosphere with a relatively low O_2 content (1 % – 3 %). In this kind of atmosphere, the oxidation was supposed to be widely prevented due to the higher activation energies for the formation of copper oxides. The values for the activation energies of bulk copper for an Ar atmosphere with 1 % O_2 are shown in Table 2. Note that the activation energies are valid for bulk copper and can be different for the oxidation of the NPC. The approximation of the oxide layer thickness with equation (24) and the activation energies for the Ar + 1 % O_2 atmosphere revealed an oxide thickness below < 50 nm even at high temperatures and long oxidation times. But

the thicknesses of the oxide layers were obviously thicker, as shown by local cross-sections. This indicates a strong dependence of the oxidation rate on slightly higher oxygen contents (> 1 %) for the NPC.

In order to understand the change of hardness and Young's modulus, a model is proposed to predict the hardness for different oxidized samples at 25°C. By inspecting Figure 4.26 (a) and Figure 4.26 (c) closer, a grown layer of different copper oxides was observed. During the oxidization of the NPC, an increase in volume of ~45% occurred. Therefore, the assumption of a dense oxide layer, which is growing from the top of the NPC, can be used for developing a model as shown in Figure 5.1.

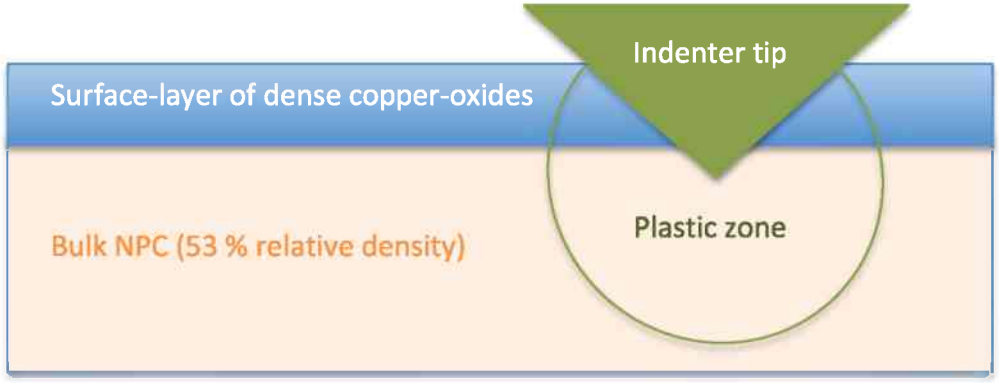

Figure 5.1: Schematic model of the oxidation behavior of the NPC and the plastic zone beyond the indenter tip.

This composite model will allow a prediction of the hardness and stiffness characteristics of the oxidized NPC. The following expression basically describes the ratio of oxide to foam in the area of the plastic zone and allows estimating the hardness:

$$H_C = H^* \cdot v^* + H_O \cdot v_O. \tag{27}$$

Where H_C is the hardness of the composite, H^* the hardness of the foam, v^* the fraction of the foam, and H_O and v_O are the corresponding values for the oxide. For the approximation of the modulus of the composite the following equation of the composite theory is used [71]:

$$E_C = \frac{E^* \cdot E_O}{E_O v^* + E^* v_O}. \tag{28}$$

Here E_C is the Young's modulus of the composite, $E^*$of the NPC and E_O of the oxide, v^* and v_O are the particular fractions of foam and oxide. This equation is derived from the composite theory for the Young's modulus according to fiber-reinforced composites, whereby the load direction is perpendicular to the fiber direction.

This assumption makes an estimation of the hardness values possible, but for estimating the Young's modulus a detailed knowledge about the oxides after different oxidation time and temperature is necessary. The mechanical properties for CuO and Cu_2O are known and shown in Table 1, but distinct hardness and Young's modulus values for the not well-investigated Cu_3O_2, which is a defect structure of Cu_2O, are not accessible. There have been some studies regarding to the oxidation temperature and time, and the resulting ratios of different copper-oxides [54,55,58,72]. Figure 4.14 shows that not only the thickness of the grown oxide is crucial, also the type of oxide after different oxidation temperatures plays a major role. The low Young's modulus of 25 GPa after 400°C (Table 7) indicates that mainly Cu_2O was formed during the oxidation [55], which has a Young's modulus of 30 GPa. The modules after 100°C/200°C and 300°C are between 30-40 GPa, which can be associated with higher ratios of CuO/Cu_3O_2 compared to Cu_2O [73], assuming that Cu_3O_2 has a modulus between CuO and Cu_2O . According to the hardness in Figure 4.14, the higher hardness slightly differs from 1200-1700 MPa due to different thicknesses of the oxide layers after annealing at certain temperatures. The individual influence of the different types of oxide on the hardness is relatively small due to similar hardness values of the oxides.

Figure 5.2 shows the model for obtaining hardness and Young's modulus values depending on the measured amount of oxide in percent inside the plastic zone. The prediction for the hardness values shows realistic values compared to the experimental values because of the relatively identical oxide hardness. A precise estimation of the Young's modulus is not possible due to the fact that the ratio of different oxides is unknown. According to the ex-situ and in-situ XRD-measurements up to 300°C, Cu_2O and CuO were formed as shown in Figure 4.28. Comparing the XRD-spectrums of Figure 4.27 and Figure 4.28, a significant higher amount of CuO was detected after long dwelling times at high temperatures. Such a change in the ratio of the oxides was also found by Lenglet et al [73]. A possible explanation of the high Young's modulus values (Table 7) is a relatively high amount of CuO compared to Cu_2O. The developed model requires a minimum ratio of 1:1 of CuO/Cu_2O or higher, and a high grade of oxidation (> 60 %) to explain the Young's modulus of 32.8 GPa after 100°C/200°C and 300°C as shown in Figure 5.2. The model predicts an oxidation of the NPC around 60-80 % for the hardness and the Young's modulus.

Table 7: Mechanical properties of different oxidized samples at 25°C.

Temperature/Oxidation time	Hardness [MPa]	Young's modulus [GPa]
Oxidized 100°C/200°C - 15h/15h	1170	37.2
Oxidized 300°C – 6h	1280	32.8
Oxidized 400°C – 5 h	1610	26.2

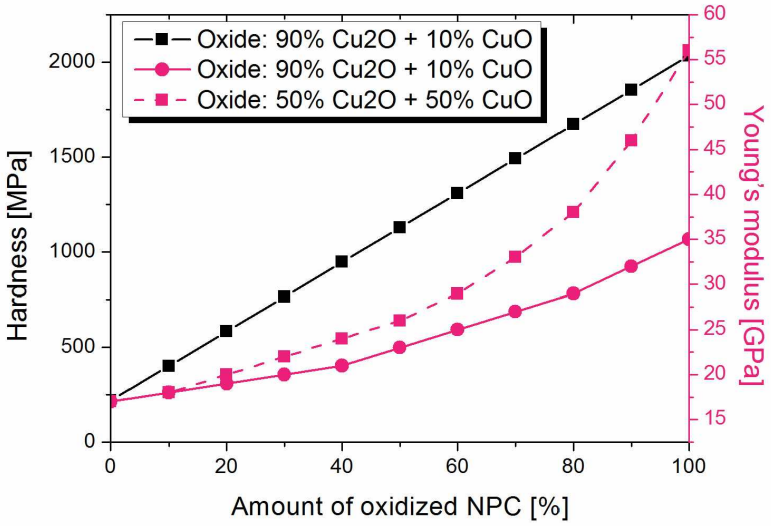

Figure 5.2: Graph of hardness and Young's modulus for different amounts of oxidized NPC in the plastic zone.

The RT hardness values for NPC of the present work and of a recent publication of Cheng et al. [57] are shown in Figure 5.3 (a). The increase of the hardness with relative density seems to be extraordinary high. One possible explanation would be the strong effect of the supersaturated Fe in the Cu ligaments. Another possible explanation is the local densification of the foam due to higher indentation depths (2000 nm) in the present than in the mentioned publication (1000 nm). Figure 5.4 (b) shows the hardness over relative density for oxidized NPC. The high hardness value for a relative density of 53 % is related to the longer heating process.

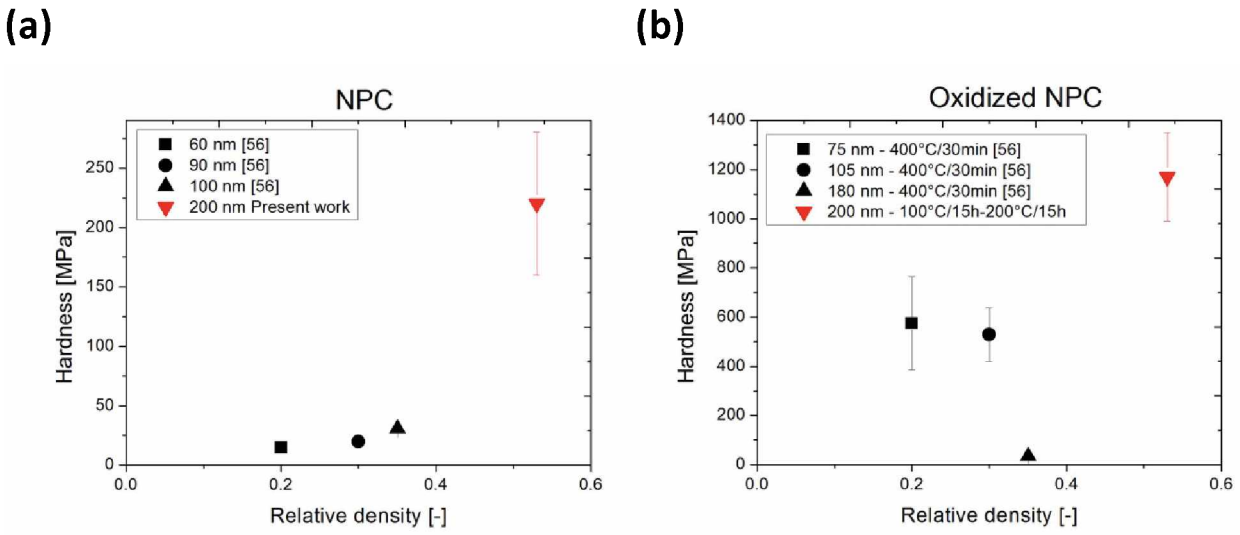

Figure 5.3: (a) Hardness over relative density for NPC with different ligament sizes. (b) Hardness over relative density for different oxidized NPC with different ligament sizes.

5.2.3 Strain rate sensitivity

The examination of the strain rate sensitivity *m* and the activation volume *A* is necessary in order to understand the deformation behavior of the material. The occurred oxidation makes the interpretation of governing deformation mechanisms more difficult. First of all, an explanation of the measurements at 25°C is necessary. All obtained *m* values from DC and CL measurements for Stage *a* and Stage *b* are around 0.03-0.04 in the non-oxidized state, as shown in Figure 4.16.

It is important to mention that besides the stress relaxation tests, Verena Maier has performed strain rate jump tests on the NPC in Erlangen at RT in order to double check the obtained results. The strain rate jumps were performed at an indentation depth of 1000 nm and 1500 nm from 0.05 s^{-1} to 0.001 s^{-1}. These tests revealed a similar strain rate sensitivity of 0.026-0.029 for the NPC.

Overall, at RT *m* is similar to the observed *m* for bulk UFG-Cu with a grain size around 150-200 nm (0.03 as summarized in Meyer et al. and Chen et al. [42,74]). The high value of *m* is related to the increased amount of grain boundaries, which are able to influence the dislocation dynamics of the material. Therefore, the behavior of the NPC and bulk UFG-Cu concerning the strain rate sensitivity are similar. After oxidation of the NPC, the *m* is still in the same order ($\sim 0.03 - 0.04$) for Stage *a* tests, as shown in Figure 4.17. Thus, the rate-controlling phase of the foam has to be the copper and not the copper oxides. This is because of a quasi-elastic behavior of the rather dense oxide on the top of the foam and a plastic behavior of the underlying copper ligaments.

Note that CSR-tests were also performed to determine *m* of the NPC. These tests have shown that this method is too sensitive for nanoporous materials due to the high standard deviation of the hardness/strain rate pairs. Stress relaxation and strain rate jump tests are more appropriate methods for the determination of the strain rate sensitivity of nanoporous materials.

Strain rate sensitivity over temperature

For an interpretation of the strain rate sensitivity it is essential to distinguish between the influence of the Cu and the copper oxide. The main deformation mechanism for copper oxide (Cu_2O) polycrystals were found to be dominated by a very limited dislocation mobility [62,63], thus resulting in a brittle behavior up to 300°C. The melting points T_m of the copper oxides are around 1200°C-1300°C and for Cu it is 1084°C. For UFG metals, thermal activated processes can even occur at temperatures > $0.2 \cdot T_m$. But thermally activated processes are not possible for the copper oxides up to 300°C as found by Vagnard et al. [65]. Hence, during the stress relaxation tests the rate-controlling mechanisms are governed by the deforming copper. The increasing strain rate sensitivity over temperature from 0.03 to 0.1–0.2, which is shown in Figure 4.16, can be explained by thermally activated climb-controlled annihilation of lattice dislocations in the Cu ligaments, which favorably takes place at high angle grain boundaries. The increased amount of high angle grain boundaries is a consequence of the HPT process. The high misorientation and amount of the high angle grain boundaries enhances climbing controlled processes even at low temperatures. At elevated temperature a similar behavior (100°C-300°C) was found for ECAP UFG Al by Priftaj et al. [75] and for ECAP UFG Cu by Bach et al. [76].

5.2.4 Activation volume

The obtained activation volume for the NPC at 25°C does not correlate with the values of bulk UFG Cu with the same structure size. The activation volume for non-oxidized NPC is in the order of 250-850 b^3 (Table 6) by taking the upper and lower boundary for the hardness to yield strength conversion into account. This indicates a dominant deformation mechanism of forest lattice dislocations, which is found rather for CG Cu (~1000 b^3). Lower values of ~100 b^3 were observed for UFG Cu [77] and UFG Al [78]. The obtained activation volume for the oxidized sample is this order of magnitude, namely 50-150 b^3. Hereby, the use of the relative activation volume of Cu is feasible due to the nearly same Burgers vector for the 1/2·{110} dislocation in Cu (b = 0.255 nm [68]) and for the 1/2·{100} dislocation in Cu_2O (b = 0.213 nm [64]). Note that this is just an assumption, because the Burgers vector is dependent on the kind of activated dislocations and this can vary, for example for Cu_2O [64]. Furthermore, the Cu mainly dominates the plastic deformation during indentation, and the influence of the

copper oxides is relatively low. In general, after the oxidation the density of the NPC increases and an oxide layer grows, and the measured activation volume significantly drops from 250-850 b^3 to 20-100 b^3 as shown in Figure 4.19 and Figure 4.20. Probably, this drop can be explained by studying the deformation behavior of Cu_2O. No further studies about the deformation behavior of CuO or Cu_3O_2 were accessible. Polycrystalline Cu_2O does not extensively plastically deform in a temperature range from 25°C up to 300°C at atmospheric pressure [64,65]. Thus, the Cu ligaments govern the plastic deformation during nanoindentation and not the copper oxide. The reason for the subsequent drop of the measured activation volume of the NPC is that the oxide layer on the top of the Cu-ligaments has an influence on the deformation mechanism of the NPC. This growing oxide layer traps dislocations inside the Cu-ligaments and strongly reduces the activation volume of the foam. Dislocations are not able to glide from the Cu phase into the ceramic phase due to differences of the crystal structure and the volume for possible dislocation dynamic is significantly reduced inside the plastic zone, which is shown in Figure 5.4 (b). Contrarily, in the case of the non-oxidized Cu ligaments, which is shown in Figure 5.4 (a), the *A* and so the dislocation dynamic is not influenced by surface oxides and the dislocations can exit to the surface.

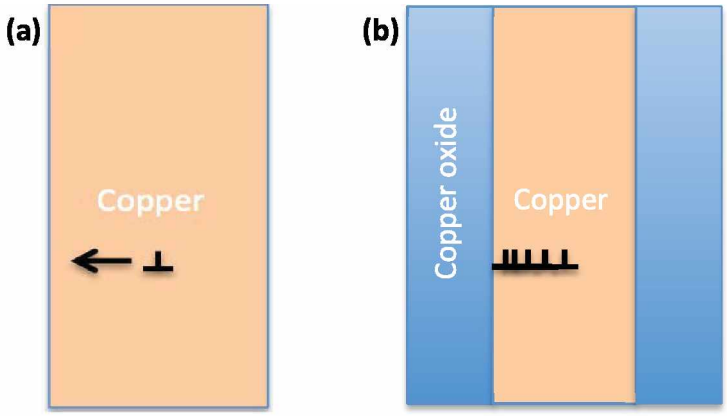

Figure 5.4: (a) Schematic of a non-oxidized ligament. Dislocation can leave the sample over the surface. (b) Schematic of an oxidized ligament. Dislocations are trapped inside the Cu-phase of the ligament.

Activation volume over temperature

The observed temperature dependence of *A* for the NPC partly correlates with the behavior found in bulk UFG Al determined using strain rate jump tests [78]. The decreasing activation volume with increasing temperature hints towards a change of the deformation mechanism related to conversion of the metal to a metal oxide. The CL and DC measurements show a sudden decrease of the *A* immediately after first oxidation has occurred. Thus the grown oxide layer on the Cu ligaments strongly influences the deformation behavior inside the material by preventing the dislocations from leaving the sample. After this first drop the activation volume up to 300°C approximately remains on the same level of 50-150 b^3 (shown in Figure 4.18 and Figure 4.19). Thus, no significant changes in the deformation mechanism are observed

anymore. To further understand the deformation behavior of the pure NPC, it would be essential to obtain data in vacuum at elevated temperatures to avoid any oxidation.

5.2.5 Comparing Stage *a* to Stage *b*

Similar trends for all measurements were obtained from DC and LC measurements concerning the stress relaxation tests. Strain rate sensitivity values obtained from Stage *b* were significantly higher than from Stage *a*, as shown in Figure 4.16 and Figure 4.17. This observation was also made before by Peykov et al.[51] and is related to thermal drift induced errors. Generally, DC measurements are the better method to obtain strain rate sensitivity and activation volume of nanoporous materials over a certain temperature range. The reason is that for obtaining activation volume the tested volume should be comparable. Therefore, the standard deviation in the mechanical and deformation properties for DC tests is significantly lower than that for CL tests due to sampling to the same plastic indentation depths, which correlates directly with the tested volume. Inhomogeneities and different temperatures prevent identical indentation depths for CL controlled measurements, as shown in the right column of Figure 4.11.

5.3 XRD measurements

The performed XRD measurements reveal more information about the oxidation behavior of the NPC. The in-situ measurements with relatively low dwelling times at certain temperatures indicate a starting oxidation at 150°C, as shown in Figure 4.27. Even at lower temperatures oxidation occurs [73] and strongly influences the mechanical properties during high temperature nanoindentation. It is important to mention that this XRD method is not sensitive enough to detect oxide layer thicknesses in the range of several nanometers that form at low temperatures. More sensitive methods are required to study the starting temperature of Cu oxidation. The Cu peak diminishing in Figure 4.27 and Figure 4.28 offers information about the transformation from copper to copper oxide in the measured zone. The slight change of the Cu (111) peak position in Figure 4.28 hints at the expansion of the lattice during heating. The ex-situ measurements revealed similar results for the oxidation of the NPC and bulk Cu, and thus most information about the oxidation behavior of Cu was taken from prior studies [57,73,79]. The Fe (110) peak (Figure 4.27 and 4.28) can be explained by encapsulated crystalline Fe, which is surrounded by the Cu. Therefore, the HCl is not able to dissolve this crystalline Fe, which is isolated by the Cu. This isolation of the Fe is related to the HPT process, heat treatment and selective dissolution manufacturing process.

6 Summary and Outlook

In this thesis, nanoporous copper was created by selective dissolution of Fe from a nanocrystalline Cu-Fe composite produced by a high-pressure torsion process. The mechanical properties and deformation behavior of the nanoporous copper were investigated using nanoindentation in a temperature range between 25°C – 300°C. High temperature nanoindentation was performed to obtain mechanical properties of the material at elevated temperatures and acquire information about the governing deformation mechanisms in the material. During the high temperature nanoindentation, oxidation of the nanoporous copper could not be avoided. To investigate the formed copper oxides, room temperature nanoindentation of the oxidized samples after high temperature tests and XRD measurements were performed in-situ and ex-situ to complement the microstructural characterization.

From the depth-sensing nanoindentation experiments, an increasing hardness and Young's modulus were observed, which is related to the oxidation of the copper foam. A model was developed taking into account the mechanical properties and growing rates of the copper oxides, which allows to explain the measured mechanical properties in dependence of the proceeding oxidation. Furthermore, depth- and load-controlled measurements were performed to obtain the strain rate sensitivity and activation volume. This allows identifying the nature of the dominating thermally activated deformation processes.

In conclusion, nanoindentation experiments at elevated temperature were successfully conducted for a nanoporous Cu. During high temperature tests, an unexpected oxidation of the copper occurred at low temperatures. This oxidation influenced the mechanical properties and the activation volume, but the rate-controlling mechanism was still dominated by the softer Cu phase. An increase of the strain rate sensitivity over temperature was observed. The formation of copper oxides rapidly influenced the activation volume due to a change in the deformation mechanism.

For further experiments it would be interesting to conduct experiments in vacuum at elevated temperatures in order to obtain high temperature information about the non-oxidized nanoporous copper, or to use face centered cubic metals with oxidation resistance, such as Au. After being able to deal with this problem, high temperature nanoindentation on lower density foams and different morphologies can be conducted in order to study the influence of these parameters more detailed.

List of Figures

List of Tables

Bibliography

[1] *Viswanathan V, Laha T, Balani K, Agarwal A, Seal S. Mater Sci Eng R Reports 2006;54:121.*

[2] *Tsuji N, Saito Y, Lee S-H, Minamino Y. Adv Eng Mater 2003;5:338.*

[3] *Valiev RZ, Islamgaliev RK, Alexandrov IV. Bulk Nanostructured Materials from Severe Plastic Deformation, vol. 45. 2000.*

[4] *Bachmaier A. Generation of Bulk Nanocomposites by Severe Plastic Deformation. Montanuniversität Leoben, 2011.*

[5] *Teplov VA. Nanostructered Mater 1995;6:437.*

[6] *Sauvage X, Pippan R. Mater Sci Eng A 2005;410-411:345.*

[7] *Sauvage X, Wetscher F, Pareige P. Acta Mater 2005;53:2127.*

[8] *Raabe D, Choi P-P, Li Y, Kostka A, Sauvage X, Lecouturier F, Hono K, Kirchheim R, Pippan R, Embury D. MRS Bull 2010;35:982.*

[9] *Fultz B, Ahn CC, Spooner S, Hong LB, Eckert J, Johnson WL. Metall Mater Trans A 1996;27:2934.*

[10] *Ma E, Atzmon M, Pinkerton FE. J Appl Phys 1993;74:955.*

[11] *Ma E. Prog Mater Sci 2005;50:413.*

[12] *Baker H. Alloy Phase Diagrams, in: ASM Met. Handb., Vol. 3. ASM Metal Handbook; 1992.*

[13] *Ding Y, Chen M, Erlebacher J. J Am Chem Soc 2004;126:6876.*

[14] *Bonroy K, Friedt J-M, Frederix F, Laureyn W, Langerock S, Campitelli A, Sára M, Borghs G, Goddeeris B, Declerck P. Anal Chem 2004;76:4299.*

[15] *Kramer D, Viswanath RN, Weissmüller J. Nano Lett 2004;4:793.*

[16] *Liu PS, Liang KM. J Mater Sci 2001;36:5059.*

[17] *Fu E, Serrano De Caro M, Wang Y, Nastasi M, Zepeda-Ruiz L, Bringa EM, Baldwin JK, Caro JA. 2012.*

[18] *Zhang Z, Wang Y, Qi Z, Zhang W, Qin J, Frenzel J. J Phys Chem C 2009;113:12629.*

[19] *Haynes WM, Lide DR, Bruno TJ. CRC Handbook of Chemistry and Physics 2012-2013. CRC Press; 2012.*

[20] *Hayes JR, Hodge AM, Biener J, Hamza A V, Sieradzki K. J Mater Res 2006;21:2611.*

[21] *Chen L-Y, Yu J-S, Fujita T, Chen M-W. Adv Funct Mater 2009;19:1221.*

[22] *Ding Y, Chen M. MRS Bull 2009;34:569.*

[23] *Erlebacher J, Seshadri R. MRS Bull 2009;34:561.*

[24] *Kaesche H. Metallic Corrosion: Principles of Physical Chemistry and Current Problems. Houston, Tex.: National Association of Corrosion Engineers; 1985.*

[25] *Yagi S. Potential-pH Diagrams for Oxidation-State Control of Nanoparticles Synthesized via Chemical Reduction, in: Thermodyn. - Phys. Chem. Aqueous Syst. n.d.*

[26] *Gibson LJ, Ashby MF. Cellular Solids: Structure and Properties, Second. Cambridge University Press; 1999.*

[27] *Hodge AM, Biener J, Hayes JR, Bythrow PM, Volkert CA, Hamza AV. Acta Mater 2007;55:1343.*

[28] *Biener J, Hodge AM, Hamza A V, Hsiung LM, Joe H. Satcher J. J Appl Phys 2005;97:24301.*

[29] *Liu R, Antoniou A. Acta Mater 2013:1.*

[30] *Wilsea M, Johnson KL, Ashby MF. Int J Mech Sci 1975;17:457.*

[31] *Olurin OB, Fleck NA, Ashby MF. Scr Mater 2000;43:983.*

[32] *Everitt NM, Davies MI, Smith JF. Philos Mag 2011;91:1221.*

[33] *Oliver WC, Pharr GM. JMaterRes 1992;7:1564.*

[34] *Maier V. Verformungsverhalten von Ultrafeinkörnigen Metallen Untersucht Mittels Neu Entwickelter Nanoindentierungsmethoden. University of Erlangen, 2013.*

[35] *Sneddon IN. Int J Eng Sci 1965;3:47.*

[36] *Atkins AG, Tabor D. J Mech Phys Solids 1965;13:149.*

[37] *Hay JL, Olive WC, Bolshakov A, Pharr GM. MRS Online Proc Libr 1998;522.*

[38] *Johnson KL. Contact Mechanics. Cambridge University Press; 1987.*

[39] *Norton FH. The Creep of Steel at High Temperatures. McGraw-Hill Book Company, Incorporated; 1929.*

[40] *Hart EW. Acta Metall 1967;15:351.*

[41] *Mayo MJ, Nix WD. Acta Metall 1988;36:2183.*

[42] *Meyers MA, Mishra A, Benson DJ. Prog Mater Sci 2006;51:427.*

[43] *Frost HJ, Ashby F. Deformation-Mechanism Maps: The Plasticity and Creep of Metals and Ceramics. Pergamon Press; 1982.*

[44] *Gibbs GB. Phys status solidi 1965;10:507.*

[45] *Coble RL. J Appl Phys 1963;34:1679.*

[46] *Suzuki T, Takeuchi S, Yoshinaga H. High-Temperature Deformation of Metals and Alloys, in: Dislocation Dyn. Plast. SE - 8, vol. 12. Springer Berlin Heidelberg; 1991.*

[47] *Kunimine T, Aragaki T, Fujii T, Onaka S, Kato M. J Mater Sci 2011;46:4302.*

[48] *Wang YM, Hamza AV, Ma E. Acta Mater 2006;54:2715.*

[49] *Mayo MJ, Siegel RW, Narayanasamy A, Nix WD. J Mater Res 1990;5:1073.*

[50] *Mayo MJ, Siegel RW, Liao YX, Nix WD. J Mater Res 1992;7:973.*

[51] *Peykov D, Martin E, Chromik RR, Gauvin R, Trudeau M. J Mater Sci 2012;47:7189.*

[52] *Raman V, Berriche R. J Mater Res 1992;7:627.*

[53] *Lucas BN, Oliver WC. Metall Mater Trans A 1999;30.*

[54] *Cocke DL, Schennach R, Hossain MA, Mencer DE, McWhinney H, Parga JR, Kesmez M, Gomes JAG, Mollah MYA. Vacuum 2005;79:71.*

[55] *Zhu Y, Mimura K, Isshiki M. Mater Trans 2002;43:2173.*

[56] *Cocke DL, Mencer DE, Hossain MA, Schennach R, Kesmez M, Parga JR, Naugle DG. J Appl Electrochem 2004;34:919.*

[57] *Cheng IC, Hodge AM. Adv Eng Mater 2012;14:219.*

[58] *Ramirez M, Henneken L, Virtanen S. Appl Surf Sci 2011;257:6481.*

[59] *Samsonov G V. The Oxide Handbook: IFI/Plenum; 1973.*

[60] *Tan EPS, Zhu Y, Yu T, Dai L, Sow CH, Tan VBC, Lim CT. Appl Phys Lett 2007;90:163112.*

[61] *Anthony JW. Handbook of Mineralogy. Mineral Data Publishing; 1990.*

[62] *Manghnani MH, Brower WS, Parker HS. Phys status solidi 1974;25:69.*

[63] *Fries E. Rev Phys Appl 1978;2:489.*

[64] *Torres G, Radcliffe V. J Mater Sci 1978;13:2164.*

[65] *Vagnard G, Washburn J. J Am Ceram Soc 1967;51:88.*

[66] *Pippan R, Scheriau S, Taylor A, Hafok M, Hohenwarter A, Bachmaier A. Annu Rev Mater Res 2010;40:319.*

[67] *Bachmaier A, Kerber M, Setman D, Pippan R. Acta Mater 2012;60:860.*

[68] *Straumanis ME, Yu LS. Acta Crystallogr Sect A 1969;25:676.*

[69] *Dao M, Lu L, Shen YF, Suresh S. Acta Mater 2006;54:5421.*

[70] *Ogata S, Li J, Yip S. Science 2002;298:807.*

[71] *Rösler J, Harders H, Bäker M. Mechanisches Verhalten Der Werkstoffe. Vieweg + Teubner; 2008.*

[72] *Cho S., Paik K. Scr Mater 1998;38:1149.*

[73] *Lenglet M, Kartouni K, Machefert J, Claude JM, Steinmetz P, Beauprez E, Heinrich J, Celati N, Spectroscopic A De, Traitement D, Surface D, Rouen U De, Saint M, Cedex A, Mi LDC, I UDN, Sciences F. 1995;30:393.*

[74] *Chen J, Lu L, Lu K. Scr Mater 2006;54:1913.*

[75] *Priftaj AV, Böhner A, May J, Höppel HW, Göken M. Mater Sci Forum 2008;586:741.*

[76] *Bach J, Liebig JP, Höppel HW, Blum W. Philos Mag 2013:24.*

[77] *Asaro RJ, Suresh S. Acta Mater 2005;53:3369.*

[78] *Wheeler JM, Maier V, Durst K, Göken M, Michler J. Mater Sci Eng A 2013;585:108.*

[79] *Korzhavyi PA, Johansson B. Literature Review on the Properties of Cuprous Oxide Cu2O and the Process of Copper Oxidation. 2011.*

Fabrication and thermo-mechanical behavior of nanoporous copper

Marius Kreuzeder[1], Manuel-David Abad[2], Mladen-Mateo Primorac[1], Peter Hosemann[2], Verena Maier[1], Marisa Rebelo de Figueiredo[2], Daniel Kiener[1] *

[1]*Department of Materials Physics, University of Leoben, A-8700 Leoben, Austria*
email: daniel.kiener@unileoben.ac.at

[2]*Department of Nuclear Engineering, University of California, Berkeley, CA 94720, USA*

Abstract

Nanoporous materials have a high potential for future applications due to excellent properties such as high strength-to-weight ratio, high surface-to-volume ratio or radiation tolerance. To use these foams efficiently in the future, it is necessary to acquire information about the foam manufacturing, their thermo-mechanical properties, and the plastic deformation mechanisms. The objective of this work was to manufacture nanoporous copper, to determine the thermo-mechanical properties, and to elucidate the deformation behavior at elevated temperatures. The experimental approach for manufacturing the foam structures used high-pressure torsion, subsequent heat treatments, and selective dissolution. Scanning electron microscopy was used for identifying the shape and size of the foam structures and their thermal stability. In-situ nanoindentation was conducted to determine mechanical properties and deformation mechanisms at elevated temperatures.

High-temperature nanoindentation was successfully conducted on nanoporous copper, showing a room temperature hardness of 220 MPa. During high temperature experiments, unexpected oxidation of the copper occurred even at low temperatures and the hardness rapidly increased to ~ 1 GPa. A model was developed, taking into account the mechanical properties of the copper oxides, which allows explaining the measured mechanical properties in dependence on the proceeding oxidation. The strain rate sensitivity of the copper foam strongly correlates with the strain rate sensitivity of ultrafine grained bulk copper. Although oxidation occurred near the surface, the rate-controlling process was still the deformation of the softer copper. An increase in the strain rate sensitivity with increasing temperature was observed, comparably to that of ultrafine grained copper, which can be linked to thermally activated processes at grain boundaries. Important insights into the effects of oxidation on the deformation behavior were obtained by assessing the activation volume. Oxidation of the copper foam, thereby hindering dislocations to exit to the surface, resulted

in a pronounced reduction of the apparent activation volume from $\sim 800\ b^3$ to $\sim 50\ b^3$, typical for ultrafine grained materials. These basic mechanistic insights shall contribute to a better understanding of the deformation processes of nanoporous materials at a microscopic level.

1 Introduction

Nanoporous materials are enormously interesting for future applications due to many excellent properties including: high surface-to-volume ratio, high strength-to-weight ratio, electrical and thermal conductivity, or radiation tolerance. These excellent properties can be used for combining structural purpose and a certain functional use in the same material at the same time. Decreasing the length-scale of ligaments down to nanometers leads to an enormous increase of the yield strength of the ligaments, approaching the theoretical strength of the material [1,2]. Therefore, weight can be reduced due to the fact that nanoporous materials show mechanical properties close to their corresponding properties of the particular bulk material. Furthermore, special material properties, such as a high surface-to-volume ratio, can be utilized for special purposes. With such promising material properties, this kind of material has high potential for future applications. One impressing fact about nanoporous materials is that the ligament size and morphology can be controlled by the manufacturing process, dedicated heat treatments, or chemical treatments. Adjusting these parameters in the right way will allow tailoring foams for certain purposes. An easy method to obtain nanoporous structures from a Cu-Fe composite is selective dissolution, which already has been used in prior works for the fabrication of metal foams such as Ag, Au, Cu, Pd or Pt [3]. The Cu-Fe system shows perfect precursor requirements for the manufacturing of a nanoporous foam by severe plastic deformation (e.g. High Pressure Torsion), due to the complete immiscibility of Cu and Fe [4].

However, to use these foams more efficiently in the future, it is necessary to acquire information about the foam manufacturing, their thermo-mechanical properties, and the plastic deformation mechanisms even if the application has a functional purpose. Nanoindentation is a well-suited method to obtain many mechanical properties for micro- and nanoporous structures with high lateral- and depth resolution [1,2]. Important data about the material can be obtained to determine the dominant deformation processes and mechanical behavior even at elevated temperatures. The rate dependent deformation mechanisms and the underlying movement of dislocations can be locally obtained by strain rate jump-tests, relaxation tests, or creep experiments [5–8]. These novel nanoindentation techniques have been developed in order to obtain local deformation mechanisms in a material. There are

several characteristic properties of a material that can be used for an understanding and description of the ongoing time and strain rate dependent mechanisms inside the material. The strain rate sensitivity *m* and the activation volume *A* are two of those characteristic properties. In prior works, nanoindentation has only been used for the determination of *m* and *A* for UFG (ultrafine grained) and CG (coarse grained) bulk metals [5,9–16], but never for nanoporous metal foams. In this this work, *m* and *A*, beside the mechanical properties, were determined by stress relaxation tests in order to get a better knowledge about the dominating deformation mechanisms of nanoporous materials at elevated temperatures.

2 Experimental procedures

2.1 Foam processing

The first step of the manufacturing chain was to get a disk shaped bulk sample out of a Cu-Fe powder mixture. The basic raw materials for the HPT (High pressure torsion) process were Copper powder (99.9% purity, - 170 + 400 mesh, 37-88 µm) and iron powder (99.9% purity, - 100 + 200 mesh, 74-149 µm). Both powders were premixed in a ratio of 50 at. % Cu and 50 at. % Fe ($Cu_{50}Fe_{50}$) and deformed by using a novel two-step HPT process, which was proposed by Bachmaier et al. [17], to achieve a homogenous and fine grained microstructure.

In order to prepare the disks, with a diameter of 8 mm and thickness 1 mm, for selective dissolution, and to reduce the amount of forced mechanical mixing between Cu and Fe, a heat treatment was conducted at 500°C with a dwelling time of 1h in a vacuum furnace (SERIES XRETORT, Xerion Advanced Heating Ofentechnik GmbH, Germany). The pressure never exceeded $3 \cdot 10^{-4}$ mbar during the heat treatment. The heating rate of the furnace was 10 °C per minute and the cooling down to RT required eight hours.

The bulk nanoporous copper (NPC) was prepared using a free corrosion process by selective dissolution of the iron. For this process, the before ground and polished slices of $Cu_{50}Fe_{50}$ were emerged to 5 wt.% hydrochloric acid (HCl) for 35 hours at a temperature of 55°C and opened to air. After 35 hours the samples were removed from the solution and cleaned in acetone and ethanol to remove the residual HCl-solution.

2.2 Foam characterization and testing

During this work all microstructural investigations were made in axial and/or tangential direction at a radius of 3 mm step related to the high-grade of deformation at this radius. After the dealloying process the morphologies and structures of the NPC were investigated to confirm a successful dissolution process. The microstructural investigations were performed in axial direction by scanning electron microscope (SEM; LEO type 1525, Carl Zeiss GmbH, Germany) equipped with an energy dispersive X-ray spectroscope (EDX) or a dual beam FIB-SEM (Qanta 3D FEG, FEI, USA). EDX spectra were collected for the NPC over a certain axial region to roughly proof the remaining Fe concentration. A more accurate method to get information about the porosity is to obtain the relative density from micrographs. SEM pictures were processed using the computer software AnalySIS (AnalySIS Pro 5.0, Olympus Soft Imaging Solutions GmbH, Germany) to use the images for a professional phase separation. Later, local cross-sections were prepared with a FIB using Gallium ions for investigating the structure and morphology beneath the surface of the foam.

The mechanical properties were tested using a nanoindenter (Micro Materials NanoTest Platform 3, Micromaterials, UK) with a high temperature option. The machine was placed into an environmental chamber purged with high purity argon to reduce the oxygen level below 2% aiming to minimize oxidation of the sample. The measurements, data recording and data evaluation were carried out using the software “NanoTest Platform Three“, Origin, and Microsoft Excel. For RT measurements the samples were fixed with super glue on a common sample holder. For the high temperature measurements the specimens were mounted onto the heated sample stage with a special high temperature cement Omegabond 600 (Omega Engineering Inc., Stamford, USA). The heating system of the indenter consists of a resistance heater at the sample stage and the indenter tip. Two thermocouples were mounted onto the sample surfaces of a reference specimen close to the measured sample and directly above the resistance heater of the heating stage to control the temperature accurately. A second heating element and thermocouple were used to control the temperature of the indenter in order to minimize thermal fluctuations during indentation. Additionally, a water-cooled heating shield was used to reduce the thermal drift. Indentations were performed at RT (22 °C), 50 °C, 100 °C, 200 °C, and 300 °C in argon atmosphere (oxygen content < 2 %). For the high temperature measurements a cubic Boron Nitride (cBN) Berkovich indenter was used up to 300 °C in argon atmosphere. After the measurements at elevated temperatures all the used samples were measured again with a diamond Berkovich indenter at RT to get information about changes of the microstructure. Indentations were performed on the planar, polished surfaces of the samples. The tip calibrations were performed on

fused silica before and after each high temperature indentation experiment cycle. For minimizing mechanically vibrations the floating table was brought into an equilibrium position before each experiment. All measurements were conducted at a radius of 3 mm from the center of the sample and the distance between the indents was at least 50 µm.

In order to get reference values for the hardness and Young's modulus of the NPC, depth sensing nanoindentations were performed to 2000 nm indentation depth with a constant strain rate of 0.1 s^{-1}. The dwell segment for the depth-controlled (DC) measurements was 30 s and the unloading rate was 10 mN/s. Constant load (CL) relaxation tests were performed to determine the strain rate sensitivity *m* of the material. For the determination of *m* it is essential to test each time a similar volume. Thus, for the experiments loads of 8 mN were used for the RT measurements at the beginning, and 30 mN for the high temperature tests and for the tests after high temperature nanoindentation up to 400 °C due to an increase of hardness related to the oxidation during the heating. For all constant load measurements a dwell time of 200 s, a loading time of 10 s and unloading time of 5 s were used. A minimum of 10 indents per temperature and condition were performed tangential. The 60 s thermal drift correction was performed post-indentation at 10 % of the maximum peak load. The last 60 % of the recorded drift data was used for the thermal drift correction. The thermal drift of all measurements was below 0.3 nm/s. The evaluation of hardness *H* and the reduced modulus E_r during this work was performed from the load-displacement curves by the Oliver-Pharr-method [18]. The near-zero Poisson ratio *v* assumption ($v = 0$) for low density foams was used for obtaining the Young's modulus *E* from the reduced modulus and for obtaining the flow stress from the hardness of the NPC ($H = \sigma_f^*$) [19].

Measurements with dwell times of 30 s and 200 s were performed for obtaining information about the rate controlling deformation mechanism of the material. The dwell period allows an exact calculation of the *m* and *A* value. The depth-time curve of the dwell period can be separated into two distinct regions, called Stage *a* and Stage *b* as proposed by Peykov et al. [6]. The following paragraph explains the evaluation of *m* and *A*.

The relative depth versus time curves of each indentation were fitted with the following empirical function [6]:

$$h_r(t) = A \cdot |h - x_c|^P, \tag{1}$$

where h_r is the relative indentation depth, *h* the actual indentation depth, and *A*, x_c, and *P* are fitting parameters. For Stage *b* all the data (200 s) were fitted, while for Stage *a* just the first 20 s were used to obtain an accurate fit. The reason for this approach was that the den-

sity of recorded values in the first regime is less than in Stage *b*. Therefore, the best and most accurate results of the fits were achieved by two distinct fits. The *m* values for each regime were calculated and compared to each other. The least-square method was used to fit the depth-time curves. The absolute depth h_a must be used for the further calculation of the displacement rate.

$$h_a(t) = h_r(t) + h_0 \tag{2}$$

Hereby h_0 is the depth of the beginning of the dwell period.

The displacement rates $\dot{h}_a$ were achieved from the derivative of this fitted curve and then the strain rates $\dot{\varepsilon} = \frac{\dot{h}_a}{h_a}$ were calculated. The current hardness under load values were obtained from the average load during the hold segment and the projected area (obtained from the original data). The hardness and strain rate were plotted in a double logarithmic plot to achieve the *m* value with two linear fits for each regime by using following relation [20,21]:

$$m = \frac{\partial \ln \sigma}{\partial \ln \dot{\varepsilon}} \sim \frac{\partial \ln H}{\partial \ln \dot{\varepsilon}} \tag{3}$$

Hereby the *m* value for Stage *a* was assessed from the recorded data of the first 20 s and the linear fit of Stage *b* included data between 30 s and 200 s. The data of the transient region was discarded between 20 s and 30 s.

Finally, the activation volume *A* was obtained for each regime by using the following equation [22]:

$$A = \sqrt{3}kT \frac{\partial \ln \dot{\varepsilon}}{\partial \sigma} = c^* \sqrt{3}kT \frac{\partial \ln \dot{\varepsilon}}{\partial H} \tag{4}$$

Here $k = 1.3806488 \times 10^{-23}\ m^2\ kg\ s^{-2}\ K^{-1}$ is the boltzmann constant and c^* is the constraint factor, which describes the relation between hardness and flow stress at 8 % representative strain for a Berkovich indenter [23].

3 Results

3.1 Foam manufacturing

The NPC is obtained by selective dissolution. During the immersion, hydrogen bubbles were generated as expected by the Pourbaix diagrams hinting at a successful dissolution [24]. The resulting structure after this process in axial direction is shown in Figure 1. The lig-

ament size of the structure is about 200 nm. Both ligament width and pore size are not perfectly homogenous throughout the whole specimen, related to manufacturing process. The relative density of this foam structure is 53 % ± 1.5 %, which was proven by EDX and by analyzing SEM-images.

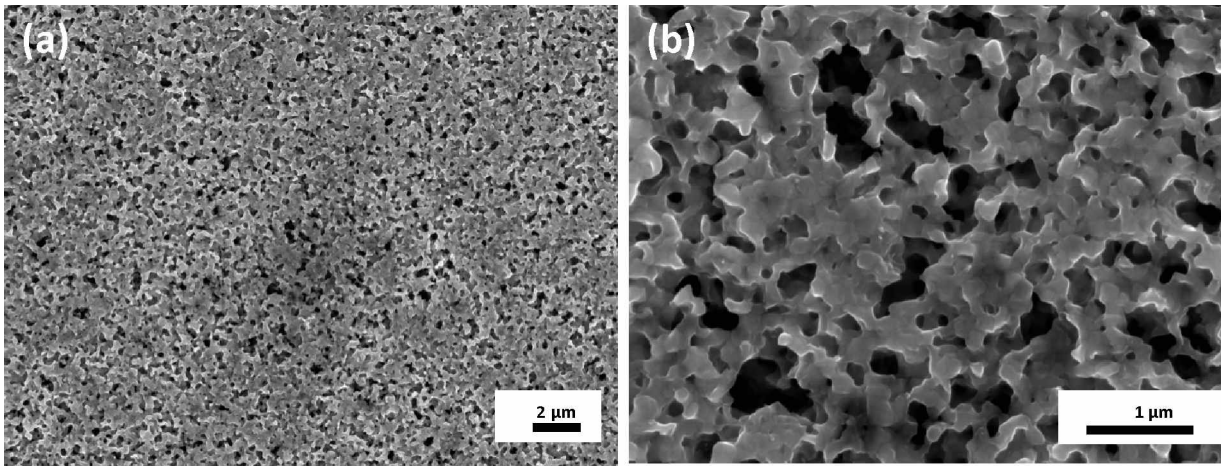

Figure 1: The SEM images show the obtained foam structure in axial direction after the selective dissolution with a low magnification in (a) and a high magnification in (b).

3.2 Young's modulus and hardness

To access the change of hardness and Young's modulus over temperature, DC measurements were performed with a constant strain rate. The pink line in Figure 2 visualizes the correlation between Young's modulus, which was obtained from the reduced modulus, and temperature. The obtained values for 25 °C in the non-oxidized state are symbolized by "Start". First, an increase of the Young's modulus from 17 ± 3.5 GPa to 26.8 ± 3 GPa was observed up to 100 °C, which was followed by a decrease in modulus down to 22.2 ± 2.2 GPa at 200 °C and 16.7 ± 2.1 GPa at 300 °C. The black line in Figure 2 shows the change of hardness over temperature. A strong increase of the hardness from 220 ± 60 MPa up to ~ 950 ± 300 MPa was observed at 50 °C, which stayed constantly at 100 °C and 200 °C. At 300 °C, a hardness drop from 940 ± 140 MPa down to 300 ± 60 MPa was observed. The values of the RT hardness after the high temperature experiments at 25 °C are shown in both graphs close to the symbol "End". The sample after high temperature indentation shows an enormous increase of around 500 % in hardness and 200 % in Young's modulus compared to the original 25°C experiments.

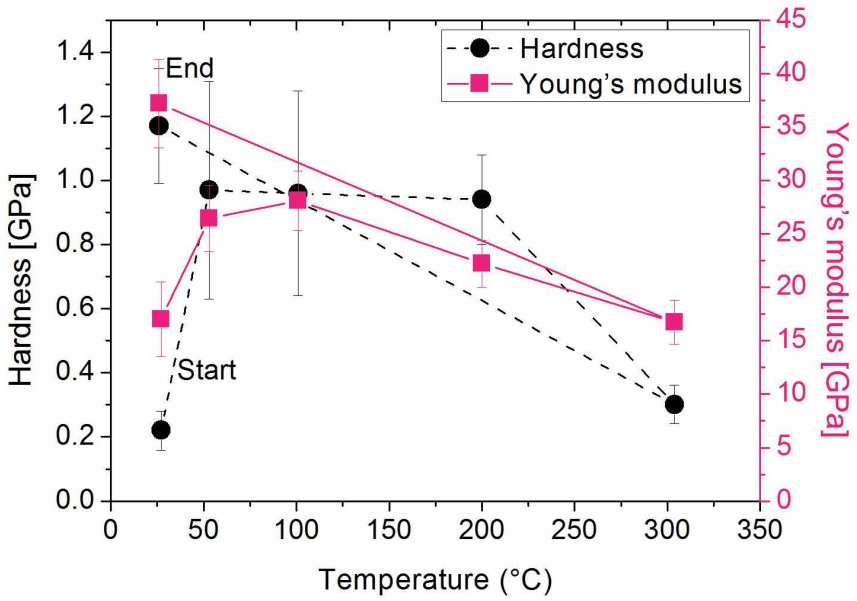

Figure 2: Young's modulus versus temperature for NPC up to 300°C (pink squares). "End" symbolizes the RT modulus after high temperature experiments. Hardness over temperature for NPC up to 300°C (black circles). "End" symbolizes the oxidized sample at RT.

3.3 Strain rate sensitivity

Figure 3 (a) shows the *m* value versus temperature for CL and DC measurements. In general, an increase of the strain rate sensitivity over temperature from 0.03 – 0.04 to 0.1 – 0.2 was observed for all different experimental conditions. For Stage *a* and Stage *b* of the CL experiments the same trend of the *m* value was observed. The results of the investigation of the RT experiments after high temperature indentation are shown in Figure 3 (b). No significant changes of the *m* value between the measurements before and after the oxidation were observed for the DC measurements, which show a very constant value of 0.03 for all different conditions. The Stage *a* *m* values of the LC measurements are around 0.04 and show higher scattering than the DC measurements. The Stage *b* results of LC measurements are between 0.04 - 0.06 and show significantly higher standard deviations.

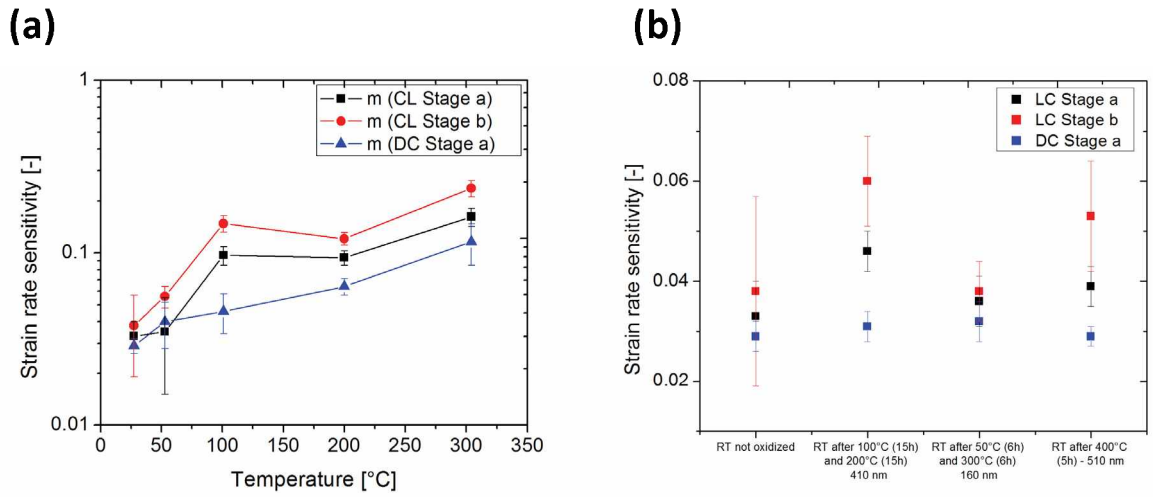

Figure 3: (a) Strain rate sensitivity over temperature for CL and DC measurements. (b) Strain rate sensitivity for a non-oxidized and different oxidized samples at RT. The tick labels on the x-axis symbolize the length of the heating segment and the estimated thickness of the oxide layer.

3.4 Activation volume

The activation volume versus temperature is plotted in Figure 4. The activation volume was normalized using the volume of a cubic Burgers vector for Cu (Dislocation: 1/2·{110}, b = 0.255 nm [25]). An upper and lower boundary calculation of the activation volume using equation (4) was performed. The upper boundary is indicated by $H \sim 3 \cdot \sigma_f$ (behavior of low density foams), and the lower boundary by $H \sim \sigma_f$. This assumption was taken into account to regard the densification of the foam during oxidizing and the correlation for ceramics between yield strength and hardness of $H \sim 1.5 \cdot \sigma_f$. The minimal (red line) and maximal (black line) activation volume versus temperature for DC measurements is plotted in Figure 4. The activation volume strongly decreases from approximately 250 - 850 b^3 at RT to 20 - 150 b^3 at 50 °C, 100 °C, 200 °C and 300 °C, respectively. Thus, *A* remains rather constant at elevated temperatures. The activation volume for the oxidized sample is about 10 - 15 times lower (10 - 100 b^3) than that of the non-oxidized material. Generally, the same trend and activation volumes as for CL-tests (Stage *a*) were observed as shown for comparison in Figure 4 (blue line) for the upper boundary. Here is to mention that CL Stage *b* values are not shown in this Figure, but Stage *a* and Stage *b* *A* values show a nearly identical trend.

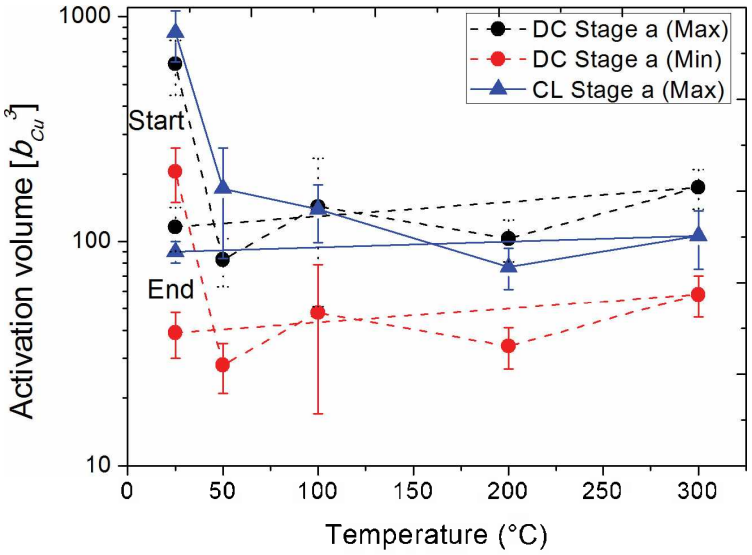

Figure 4: Relative *A* obtained from DC and CL measurements. The minimal and maximal normalized *A* for DC measurements are plotted. *For* comparison maximal CL Stage *a* results are shown.

4 Discussion

4.1 Young's modulus and hardness

The hardness values of CuO and Cu_2O are between 2050 – 2490 MPa and 2010 – 2030 MPa [26], respectively, while the yield strength value of UFG Cu (grainsize around 200 nm) is ~ 450 MPa [27,28]. This corresponds to a hardness for UFG Cu of 1350 MPa ($H = 3\sigma_f$). Thus, the difference in hardness between copper and copper-oxide is significant. The increase of Young's modulus cannot only be explained by the values of CuO and Cu_2O, which are 80 GPa and 30 GPa [29,30], respectively, because during the oxidation of Cu to copper oxide (mainly Cu_2O), the relative density of the foam increases due to increase in volume. This is because of the uptake of oxygen from of the atmosphere. The volume of the foam would increase by 40 – 45 % if the copper completely converts to copper oxide. Thus, the relative density would be ~ 95 % up to nearly 100 %. Figure 5 (b) shows a micrograph of a local cross-section of a residual impression after high temperature experiments for six hours at 100 °C for and 200 °C, respectively. The increase of relative density up to 95 % close to the surface can be clearly seen in Figure 5 (b). Furthermore, the roughness of the surface has increased dramatically, resulting in a relatively high standard deviation of hardness and Young's modulus values, as shown in Figure 2. This is related to an inhomogeneous oxidation process of the surface, as shown in Figure 5 (b). The local-cross section also shows that the first one or two micrometers of the surface are completely oxidized and seemingly dense, even after low temperature oxidation of the NPC at 100 °C for six hours and 200 °C for six hours. The zone below the oxidized layer is not much affected by the oxidation.

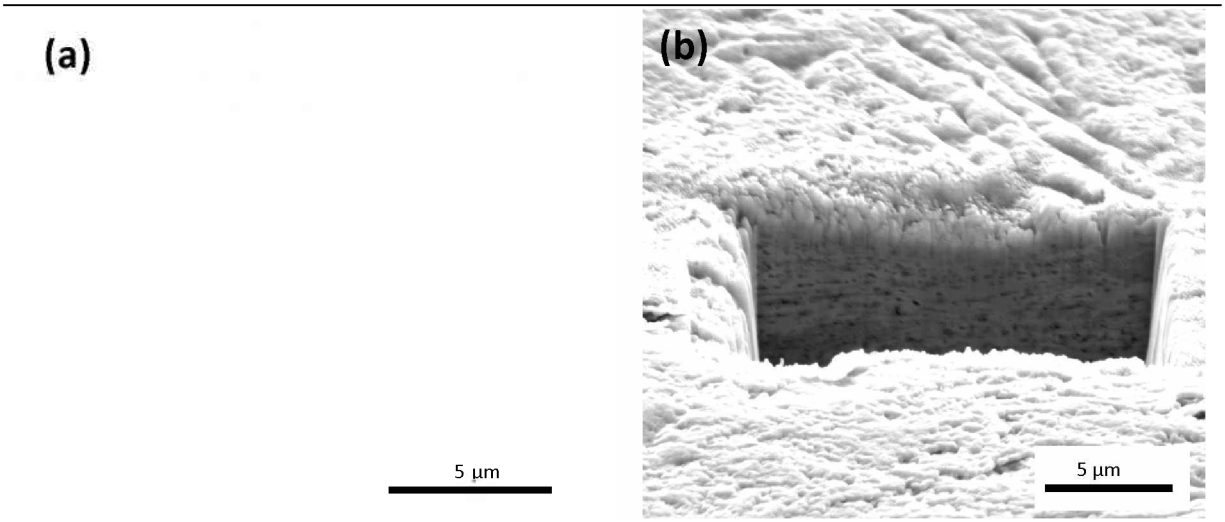

Figure 5: (a) SEM image of a local cross-section beneath a residual impression in the non-oxidized state. (b) Corresponding local cross-section showing a rather dense oxide layer after 100 °C / 6h hours and 200 °C / 6 hours.

The flow stress of the foam can be compared to the values predicted by scaling laws. The flow stress of the NPC was assessed from the hardness values obtained by the indentation experiments (for low density foams: $H = \sigma_f^*$ [19]). According to this relationship, the flow stress of the NPC investigated in the present study is 220 MPa at 25 °C. The yield strength for bulk copper with an average grain size of 200 nm is 450 MPa [27,28]. Note that the flow stress is obtained from the hardness of nanoindentation tests, and the yield stress σ_{pl}^* of the foam from the scaling law equation [19]:

$$\sigma_{pl}^* = C_1 \cdot \sigma_{ys} \cdot (\rho^*/\rho_s)^n \quad (5)$$

Where σ_{ys}, ρ_s, and ρ^* are the yield strength of the solid, the density of the solid, and the density of the foam, respectively. ($C_1 = 0.3$ and n = 1.5 [19]). Nevertheless, the flow stress and the yield stress can be compared for a good estimation, since for these high strength NPC materials the work hardening is not very pronounced. The yield strength for the porous material was estimated by using the scaling equation of Ashby and Gibson, and was compared to the measured flow stress ($H = \sigma_f^*$) [19]. The experimentally determined value of the yield stress and the flow stress is nearly five times larger than that value predicted by equation (5), 220 MPa instead of 52 MPa. This deviation gives rise to the question whether the scaling laws deduced from macroscopic foams can still be applied to nanoporous materials. Further possible explanations for this difference are:

- There is still supersaturated Fe in the Cu ligaments
- The Gibson and Ashby equation is rather valid for homogenous foam structures and lower relative densities [19]
- The theory of the near zero Poisson's ratio is not completely valid for the NPC [19]

- The used yield strength for bulk Cu with 200 nm grain size is just an estimation

But in order to make an estimation, we assume that the Ashby and Gibson equation (5) describes the mechanical properties of the NPC well [19]. Then the experimentally determined value of 220 MPa for the yield strength of the NPC would require that the yield strength of the foam ligaments be in the order of 1.9 GPa. This interpretation suggests that the yield strength of the ligaments in the NPC would approach the theoretical strength of Cu (> 6 GPa [31]). Similar high values were also achieved for NC Au foams by Biener et al. [2].

The Young's modulus of the NPC is 17 GPa at 25 °C. Assuming that the NPC sample exhibits a relative density of 53 % and using the following equation of Ashby and Gibson [19]:

$$E^* = C_2 \cdot E_s \cdot (\rho^*/\rho_s)^n, \tag{6}$$

the scaling law would predict a Young's modulus of 28 – 36 GPa. Whereby in equation (6), E_s (for Cu E = 100 –130 GPa), ρ_s, and ρ^* are the Young's modulus, the density of the solid material, and the density of the foam, respectively ($C_1 = 1$ and n = 2 [19]). The difference of 10 – 20 GPa can be explained by the layered-structure of the NPC from the HPT shear deformation process, which is shown in Figure 5 (a) and (b). The ligaments in the direction of indentation do not exist in the same density like the ligaments perpendicular to them, which is related to the inhomogeneity of the deformation process. The outcome of this is a lower Young's modulus in loading direction.

In order to understand the change of hardness and Young's modulus, a model is proposed to predict the hardness for different oxidized samples at 25 °C. During the oxidization of the NPC, an increase in volume of ~ 45% occurred. Therefore, the assumption of a dense oxide layer, which is growing from the top of the NPC, can be used for developing a model as shown in Figure 6 (a). This composite model will allow a prediction of the hardness and stiffness characteristics of the oxidized NPC. The following expression basically describes the ratio of oxide to foam in the area of the plastic zone and allows estimating the hardness:

$$H_C = H^* \cdot v^* + H_O \cdot v_O. \tag{7}$$

Where H_C is the hardness of the composite, H^* the hardness of the foam, v^* the fraction of the foam, and H_O and v_O are the corresponding values for the oxide. For the approximation of the modulus of the composite the following equation of the composite theory is used [32]:

$$E_C = \frac{E^* \cdot E_O}{E_O v^* + E^* v_O}. \quad (8)$$

Here E_C is the Young's modulus of the composite, $E^*$of the NPC and E_O of the oxide, v^* and v_O are the particular fractions of foam and oxide. This equation is derived from the composite theory for the Young's modulus according to fiber-reinforced composites, whereby the load direction is perpendicular to the fiber direction.

This assumption makes an estimation of the hardness values possible, but for estimating the Young's modulus a detailed knowledge about the oxides after different oxidation time and temperature is necessary. Therefore, some studies can be found regarding the oxidation temperature and time, and the resulting ratios of different copper-oxides [33–36]. Not only the thickness of the grown oxide is crucial, also the type of oxide after different oxidation temperatures plays a major role.

Figure 6 (b) shows the results of the model for obtaining hardness and Young's modulus values depending on the measured amount of oxide in percent inside the plastic zone. The prediction for the hardness is quite accurate due to the nearly identical oxide hardness. A precise estimation of the Young's modulus is not possible due to the fact that the ratio of different oxides is unknown. Such a change in the ratio of the oxides was also found by Lenglet et al [37].

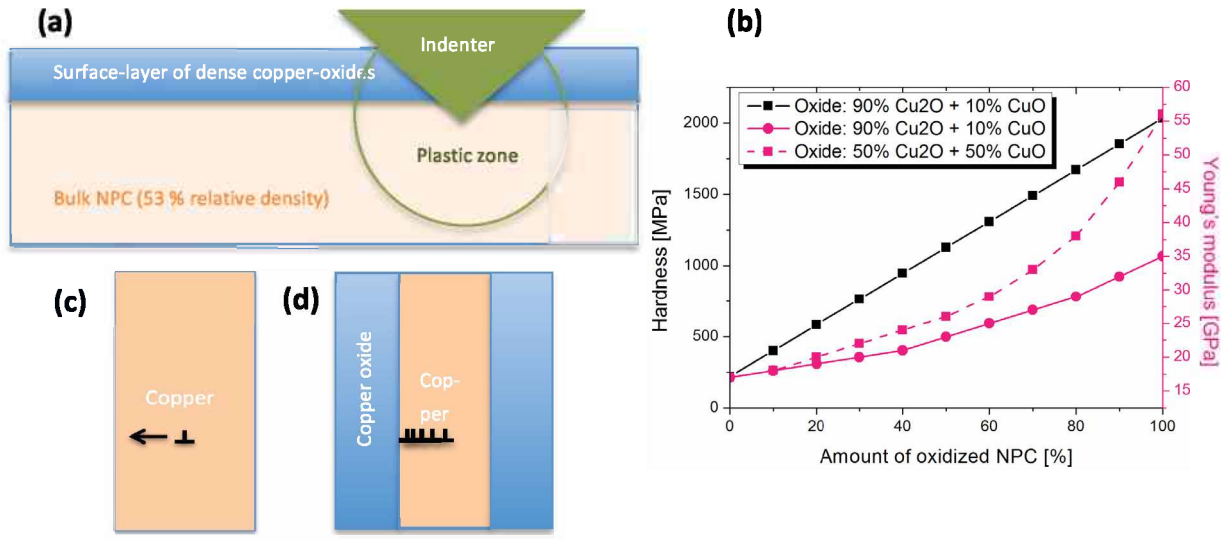

Figure 6: (a) Schematic model of the oxidation behavior of the NPC and the plastic zone beyond the indenter tip. (b) Hardness and Young's modulus for different amounts of oxidized NPC in the plastic zone. (c) Schematic of a non-oxidized ligament. Dislocations can exit to the sample surface. (d) Schematic of an oxidized ligament. Dislocations are trapped inside the Cu-phase of the ligament.

4.2 Strain rate sensitivity

The examination of the strain rate sensitivity *m* and the activation volume *A* is necessary in order to understand the deformation behavior of the material. The occurred oxidation makes the interpretation of governing deformation mechanisms more difficult. All obtained *m* values from DC and CL measurements for Stage *a* and Stage *b* are around 0.03 – 0.04 in the non-oxidized state, as shown in Figure 3. At RT *m* is similar to the observed *m* for bulk UFG Cu with a grain size around 150 - 200 nm (0.03 as summarized in Meyers et al. and Chen et al. [16,28]). The high value of *m* is related to the increased amount of grain boundaries, which are able to influence the dislocation mobility of the material. Therefore, the behavior of the NPC and bulk UFG Cu concerning the strain rate sensitivity are similar. After oxidation of the NPC, *m* is still in the same order ($\sim 0.03 - 0.04$) for Stage *a* tests, as shown in Figure 3 (b). Thus, during stress relaxation tests the rate-controlling phase of the foam has to be the copper and not the copper oxides. This is because of a quasi-elastic behavior of the rather dense oxide on the top of the foam and a plastic behavior of the underlying copper ligaments. The copper oxide (Cu_2O) polycrystals were found to be dominated by a very limited dislocation mobility [30,38], thus resulting in a brittle behavior up to 300°C.

The increasing strain rate sensitivity over temperature from 0.03 to 0.1 – 0.2, which is shown in Figure 3, can be explained by thermally activated climb-controlled annihilation of lattice dislocations in the Cu ligaments, which favorably takes place at high angle grain boundaries [39,40]. The increased amount of high angle grain boundaries is a consequence of the HPT process. The high misorientation and amount of the high angle grain boundaries enhances climbing controlled processes even at low temperatures. At elevated temperature a similar behavior (100°C-300°C) was found for ECAP UFG Al by Vevecka-Priftaj et al. [40] and for ECAP UFG Cu by Bach et al. [41].

4.3 Activation volume

The obtained activation volume for the NPC at 25°C does not correlate with the values of bulk UFG Cu with the same structure size. The activation volume for non-oxidized NPC is in the order of 250 – 850 b^3 by taking the upper and lower boundary for the hardness to yield strength conversion into account. This indicates a dominant deformation mechanism of forest lattice dislocations, which is found rather for CG Cu ($\sim 1000\ b^3$). Lower values of $\sim 100\ b^3$ were observed for UFG Cu [13] and UFG Al [9]. The obtained activation volume for the oxidized sample is this order of magnitude, namely 50 – 150 b^3. Hereby, the use of the relative activation volume of Cu is feasible due to the nearly same Burgers vector for the 1/2·{110} dislocation in Cu (b = 0.255 nm [25]) and for the 1/2·{100} dislocation in Cu_2O (b = 0.213 nm

[42]). In general, after the oxidation the density of the NPC increases and an oxide layer grows, and the measured activation volume significantly drops from $250-850\,b^3$ to $20-100\,b^3$ as shown in Figure 4. Polycrystalline copper oxides does not extensively plastically deform in a temperature range from 25 °C up to 300 °C at atmospheric pressure [42,43]. Thus, the Cu ligaments govern the plastic deformation during nanoindentation and not the copper oxide. The reason for the subsequent drop of the measured activation volume of the NPC is that the oxide layer on the top of the Cu-ligaments has an influence on the deformation mechanism of the NPC. This growing oxide layer traps dislocations inside the Cu-ligaments and strongly reduces the activation volume of the foam, as shown in Figure 6 (d). Dislocations are not able to glide from the Cu phase into the ceramic phase due to differences of the crystal structure and the volume for possible dislocation dynamic is significantly reduced inside the plastic zone. Contrarily, in the case of the non-oxidized Cu ligaments, which is shown in Figure 6 (c), the *A* and so the dislocation mobility is not influenced by surface oxides and the dislocations can exit to the surface. Both, the CL and DC measurements show a sudden decrease of *A* immediately after first oxidation has occurred (Figure 4). After this first drop the activation volume up to 300 °C approximately remains on the same level of $50-150\,b^3$, as shown in Figure 4. Thus, no significant changes in the deformation mechanism are observed anymore.

4.4 Comparing Stage *a* and Stage *b*

Similar trends for all measurements were obtained from DC and LC measurements concerning the stress relaxation tests. Strain rate sensitivity values obtained from Stage *b* were significantly higher than from Stage *a*, as shown in Figure 3 (a) and (b). This observation was also made before by Peykov et al. [6], and is related to thermal drift induced errors and higher strain rates in Stage *a* ($\dot{\varepsilon} \sim 10^{-2}-10^{-3}$) than in Stage *b* ($\dot{\varepsilon} \sim 10^{-3}-10^{-4}$) during the dwell segment. Generally, DC measurements are the better method to obtain strain rate sensitivity and activation volume of nanoporous materials over a certain temperature range. The reason is that for obtaining activation volume the tested volume should be comparable. Therefore, the standard deviation in the mechanical and deformation properties for DC tests is significantly lower than that for CL tests due to sampling to the same plastic indentation depths, which correlates directly with the tested volume. Inhomogeneities and different temperatures prevent identical indentation depths for CL controlled measurements.

5 Summary

In conclusion, nanoindentation experiments at elevated temperature were successfully conducted on nanoporous Cu. During high temperature testing, an unexpected oxidation of the copper occurred at low temperatures. An increasing hardness and Young's modulus were observed, which is related to the oxidation of the copper foam. A model was developed taking into account the mechanical properties and growing rates of the copper oxides, which allows the explanation of the measured mechanical properties in dependence on the proceeding oxidation. The oxidation did not significantly change the strain rate sensitivity of the NPC, which was in the order of magnitude as for UFG bulk copper. Furthermore, an increase of the strain rate sensitivity over temperature was observed and correlated to thermally activated grain boundary processes. The activation volume was strongly influenced by the oxidation due to a change in deformation mechanism.

6 Acknowledgement

The financial support by the Austrian "Marshall-Plan Scholarships" and the University of Leoben is gratefully acknowledged.

References

[1] *Hodge AM, Biener J, Hayes JR, Bythrow PM, Volkert CA, Hamza AV. Acta Mater 2007;55:1343.*

[2] *Biener J, Hodge AM, Hamza A V, Hsiung LM, Joe H. Satcher J. J Appl Phys 2005;97:24301.*

[3] *Zhang Z, Wang Y, Qi Z, Zhang W, Qin J, Frenzel J. J Phys Chem C 2009;113:12629.*

[4] *Baker H. Alloy Phase Diagrams, in: ASM Met. Handb., Vol. 3. ASM Metal Handbook; 1992.*

[5] *Alkorta J, Martínez-Esnaola JM, Gil Sevillano J. Acta Mater 2008;56:884.*

[6] *Peykov D, Martin E, Chromik RR, Gauvin R, Trudeau M. J Mater Sci 2012;47:7189.*

[7] *Maier V, Merle B, Göken M, Durst K. J Mater Res 2013;28:1177.*

[8] *Maier V, Durst K, Mueller J, Backes B, Höppel HW, Göken M. J Mater Res 2011;26:1421.*

[9] *Wheeler JM, Maier V, Durst K, Göken M, Michler J. Mater Sci Eng A 2013;585:108.*

[10] *Wei Q, Cheng S, Ramesh K., Ma E. Mater Sci Eng A 2004:71.*

[11] *Wang YM, Hamza AV, Ma E. Acta Mater 2006;54:2715.*

[12] *Huang P, Wang F, Xu M, Xu KW, Lu TJ. Acta Mater 2010;58:5196.*

[13] *Asaro RJ, Suresh S. Acta Mater 2005;53:3369.*

[14] *Cavaliere P. Phys B Condens Matter 2008;403:569.*

[15] *Champion Y, Nowak S. Mater Sci Forum 2008;584-586:399.*

[16] *Chen J, Lu L, Lu K. Scr Mater 2006;54:1913.*

[17] *Bachmaier A, Hohenwarter A, Pippan R. Scr Mater 2009;61:1016.*

[18] *Oliver WC, Pharr GM. JMaterRes 1992;7:1564.*

[19] *Gibson LJ, Ashby MF. Cellular Solids: Structure and Properties, Second. Cambridge University Press; 1999.*

[20] *Hart EW. Acta Metall 1967;15:351.*

[21] *Mayo MJ, Nix WD. Acta Metall 1988;36:2183.*

[22] *Gibbs GB. Phys status solidi 1965;10:507.*

[23] *Johnson KL. Contact Mechanics. Cambridge University Press; 1987.*

[24] *Kaesche H. Metallic Corrosion: Principles of Physical Chemistry and Current Problems. Houston, Tex.: National Association of Corrosion Engineers; 1985.*

[25] *Straumanis ME, Yu LS. Acta Crystallogr Sect A 1969;25:676.*

[26] *Samsonov G V. The Oxide Handbook: IFI/Plenum; 1973.*

[27] *Dao M, Lu L, Shen YF, Suresh S. Acta Mater 2006;54:5421.*

[28] *Meyers MA, Mishra A, Benson DJ. Prog Mater Sci 2006;51:427.*

[29] *Tan EPS, Zhu Y, Yu T, Dai L, Sow CH, Tan VBC, Lim CT. Appl Phys Lett 2007;90:163112.*

[30] *Manghnani MH, Brower WS, Parker HS. Phys status solidi 1974;25:69.*

[31] *Ogata S, Li J, Yip S. Science 2002;298:807.*

[32] *Rösler J, Harders H, Bäker M. Mechanisches Verhalten Der Werkstoffe. Vieweg + Teubner; 2008.*

[33] *Zhu Y, Mimura K, Isshiki M. Mater Trans 2002;43:2173.*

[34] *Cocke DL, Schennach R, Hossain MA, Mencer DE, McWhinney H, Parga JR, Kesmez M, Gomes JAG, Mollah MYA. Vacuum 2005;79:71.*

[35] *Cho S., Paik K. Scr Mater 1998;38:1149.*

[36] *Ramirez M, Henneken L, Virtanen S. Appl Surf Sci 2011;257:6481.*

[37] *Lenglet M, Kartouni K, Machefert J, Claude JM, Steinmetz P, Beauprez E, Heinrich J, Celati N, Spectroscopic A De, Traitement D, Surface D, Rouen U De, Saint M, Cedex A, Mi LDC, I UDN, Sciences F. 1995;30:393.*

[38] *Fries E. Rev Phys Appl 1978;2:489.*

[39] *May J, Höppel HW, Göken M. Scr Mater 2005;53:189.*

[40] *Priftaj AV, Böhner A, May J, Höppel HW, Göken M. Mater Sci Forum 2008;586:741.*

[41] *Bach J, Liebig JP, Höppel HW, Blum W. Philos Mag 2013:24.*

[42] *Torres G, Radcliffe V. J Mater Sci 1978;13:2164.*

[43] *Vagnard G, Washburn J. J Am Ceram Soc 1967;51:88.*